Properties of the $CuGaSe_2$ and $CuInSe_2$ (001) Surface

vorgelegt von
Diplom-Ingenieurin
Thalia Deniozou
aus Genf

der Fakultat II - Mathematik und Naturwissenschaften
der Technischen Universtitat Berlin
zur Erlangung des akademischen Grades

Doktor der Naturwissenschaften
- Dr. rer. nat. -

genehmigte Dissertation

Promotionsausschuss:

Vorsitzender:	Prof. Dr. A. Knorr
Berichter:	Prof. Dr. C. Thomsen
Berichter:	Dr. N. Esser

Tag der wissenschaftlichen Aussprache: 2. November 2005

Berlin 2005
D 83

Abstract

The main task of this work was to investigate the (001) $CuGaSe_2$ and $CuInSe_2$ surface in dependence of preparation and stoichiometry. The knowledge of the atomic structure as well as other surface properties is important in respect to optimization of novel thin film solar cells. For the characterization of the layers mainly Auger electron spectroscopy, low-energy electron diffraction and photoelectron spectroscopy were implemented. The development of an appropriate procedure with Ar^+ sputtering and annealing combined with decapping enabled the preparation of clean and well-ordered surfaces. Different surface structures were observed in dependence of the layer preparation and composition. A (4×1) reconstruction was observed for the first time on $CuGaSe_2$ layers grown with a moderate Cu-excess after preparation by sputtering and annealing. Similarly a (4×2) reconstruction was detected on $CuInSe_2$ surfaces of Cu-poor layers. A reconstruction could be also observed on Cu-poorer layers, however the facets/steps could not be completely removed. Cu-richer layers were facet-free, however the observed reconstruction was also weaker. Thus it was shown that in contrary to recent expectations, according to which only the (112) surface is stable, also the (001) can be stable under particular conditions. The appearance of facets or steps is correlated with the presence of $CuIn_3Se_5$ or $CuGa_3Se_5$ phases. This information is furthermore important for the understanding of grain boundaries in polycrystalline $CuGaSe_2$ and $CuInSe_2$. Binding energy shifts were observed for the first time on all Se3d, In4d, Ga3d, Cu3d core levels of the reconstructed surfaces. By comparison with results from the literature from the similar ZnSe (100) surface a modell for the (4×2) reconstruction was proposed. The

surface components in the Se3d, In4d and Cu3d emission were attributed to Se dimers or In and Cu adatoms respectively. The ($\times$1) periodicity of the (4×1) reconstruction of $CuGaSe_2$ is interpreted as a Ca/Cu disorder in the adatom chains.

List of publications

Surface Structure of $CuGaSe_2$.
Th. Deniozou, N. Esser, S. Siebentritt, P. Vogt, and R. Hunger
Thin Solid Films **480-481** (2004) 382.

The $CuGaSe_2$ (001) surface: A (4×1) reconstruction.
Th. Deniozou, S. Siebentritt, and N. Esser
Surface Science **579** (2005) 100.

A (4×2) reconstruction of $CuInSe_2$ (001) studied by LEED and SXPS.
Th. Deniozou, N. Esser, Th. Schulmeyer, and R. Hunger
Appl. Phys. Lett., in print.

Surface structure and electronics of the $CuInSe_2$ and $CuGaSe_2$ (001) surface
Th. Deniozou, N. Esser, K. Sakurai, S. Niki, S. Siebentritt, P. Vogt, Th. Schulmeyer, and R. Hunger
submitted in *Phys. Rev. B.*

Contents

1 Introduction

To date Si is the most established material in semiconductor technology for photovoltaics. Cell efficiencies reach up to 25% [1] while module performances up to 14%. However, it is not expected that Si solar cells will meet the requirements for mass penetration of photovoltaics in the market. Despite the reached efficiencies, Si crystals are expensive and slow to grow. As Si with its indirect band gap is the most weakly absorbing semiconductor, a high material volume is nescessary and consequently also a high quality material. Thus the material costs are quite high with concern to mass production.

Thin films represent a recent alternative option for solar cells with respect to production costs. They are so thin that a substrate is nescessary to provide mechanical support. Low costs result from the reduced material volume, relative low-cost substrates such as glass, metal foils or plastics, lower deposition temperatures. Furthermore thin films can tolerate higher impurities without affecting the efficiency and are easily integrated into a monolithic interconnected module. However, thin films can not replace Si in the market yet, as different hindrances have still to be overcome. The efficiencies reached are still to low in comparison to the Si analogues. The main reason lies in the much less-developed knowledge and technology base compared to Si. While the Si technology could simply adopt the already mature technology from Si electronics industry, Cu-chalcopyrite materials implemented in thin films have no real application outside of photovoltaics. A deeper and more extensive understanding of materials and devices has still to be developed, as well as the appropriate equipment and processing to manufacture them.

The highest efficiencies until now have been reached by polycrystalline $Cu(In, Ga)Se_2$ devices with 19% for cells [2] and 10% for modules. Besides $Cu(In, Ga)Se_2$ devices,

stacked cells of semiconductors with different bandgaps, like CuInS/Se_2 and $CuGaSe_2$, is an other option with apparently promising prospects. As multijunction cells possess a much higher efficiency limit in comparison to single cells, they are expected to progress in efficiency for a longer time. $CuInSe_2$ cells show already efficiencies up to 15% [3] which are limited by their low band gap, whereas $CuGaSe_2$ cell efficiencies are still quite low by 10% [4]. However, the emerged progress is largely empirical, whereas the fundamental understanding of these materials and devices is still quite limited [5].

Some of the main challenges for Cu-chalcopyrites based technology are to better understand the chemical and electronic nature of defects which limit the open circuit voltage V_{OC} and reduce the number of recombination centers [6]. Therefore a comprehensive model for the growth of Cu-chalcopyrites has to be developed with respect to the processing parameters determining defect formation as well as junction formation [7]. A further basic issue lies in the fundamental understanding of the nature of grain boundaries and free surfaces. The surface chemistry during heterojunction formation plays a decisive role for final performance [108]. The deposition of the buffer layer and the formation of heterojunction heavily affects not only surface defects but also defects in the bulk. The recombination under open-circuit conditions takes place only some 50-100 nm away from the surface, thus the mastering of the near surface chemistry is an extremely challenging task in future. Furthermore the role of the CdS layer should be studied so as to later introduce an alternative material containing no Cd and providing a wider band gap. Progress in these issues would enable a significant increase of efficiency.

Thus the investigation of Cu-chalcopyrite surfaces by identifying surface structures and electronic surface properties in dependence from stoichiometry is important towards the understanding of solar cell properties and their optimization. However, knowledge in this area is still quite limited, mainly due to the problems encountered when trying to prepare clean, ordered Cu-chalcopyrite surfaces.

Therefore a main subject of this work is the study of the preparation as well as the properties of (001) chalcopyrite surfaces and especially of the (001) $CuGaSe_2$ and $CuInSe_2$ surfaces. The preparation of the $CuGaSe_2$ surface with Ar^+ ion sputtering and

annealing is studied as a factor of Ar^+ ion energy, time and temperature. In the case of the $CuInSe_2$ surfaces the method of decapping is also applied in order to obtain clean surfaces. Next, the sputtering procedure optimized on the $CuGaSe_2$ surface is employed on the $CuInSe_2$ surface so as to improve the surface structure.

The clean surfaces are investigated with respect to composition and structure by means of AES (Auger Electron Spectroscopy) and LEED (Low Energy Electron Diffraction). Apart from the degree of cleanliness of the surfaces, the surface stoichiometry is studied in correlation with the observed symmetry and periodicity on these surfaces. Further information about their morphology is derived by AFM (Atomic Force Microscopy).

SXPS (soft X-Ray Photoemission Spectroscopy) is implemented to determine the chemical state of the atoms involved in the reconstructions observed for the first time on (001) chalcopyrite surfaces. By considering the similar results obtained on both the $CuGaSe_2$ and $CuInSe_2$ surface, a general structure model is proposed. Besides the surface structure, morphology and composition is related to the bulk composition with which the layers have been grown.

A further subject of this work is the investigation of the $ZnSe/CuGaSe_2$ interface. ZnSe has been deposited on the clean $CuGaSe_2$ prepared by sputtering. The surface properties during deposition are monitored with AES and LEED, whereas the impact of the deposition process on the bulk properties of $CuGaSe_2$ is investigated with Raman and luminescence spectroscopy.

Additionaly, the optimized preparation process is applied to the chalcopyrite $ZnGeP_2$ and the deposition of Mn on the $ZnGeP_2$ surface is studied with LEED and AES as well.

2 Solar cells

Solar cell applications are based upon the photovoltaic effect. Photons with an energy above the band gap of the absorber material generate electron-hole pairs which are separated by the in-built electric field. This field is created either by a p-n-junction within the absorber material and between the semiconductor and an other material. As far as commercial applications are concerned, chalcopyrites $Cu(In, Ga)(S, Se)_2$ are good candidates in comparison to III-V materials or Si for the absorber material due to their low production costs. The first experimental device that indicated the potential for $CuInSe_2$ was a heterojunction between a p-type single crystal of $CuInSe_2$ as absorber and a thin film of n-type CdS [9, 10]. Nowadays chalcopyrite cells reach above 19% efficiency [2]. The modules of $Cu(In, Ga)(S, Se)_2$ solar cells are in pilot production at several sites worldwide, and large modules have reached efficiencies above 13% [11] and output power of 80W [12]. The mass production is to start in Europe in 2006 [13]. As far as the buffer layer is concerned, meanwhile besides CdS also the less toxic alternative ZnSe/ZnS [14] has been introduced. In order to allow high transmission of photons, at the front electrode of the cell a metal is used as window layer, like the transparent high conducting oxide ZnO. The charge carriers are collected by electrodes which can generate a current in the outer circuit. The back contact consists of a low-cost glass substrate coated with Mo. The corresponding cross-section of a solar-cell is shown in Fig. 2.1. Different deposition techniques are used for each layer with different advantages and disadvantages.

The tailoring of the bandgap by the choice of the right material plays an important role for maximizing the efficiency. While with a bandgap larger than the energy of the

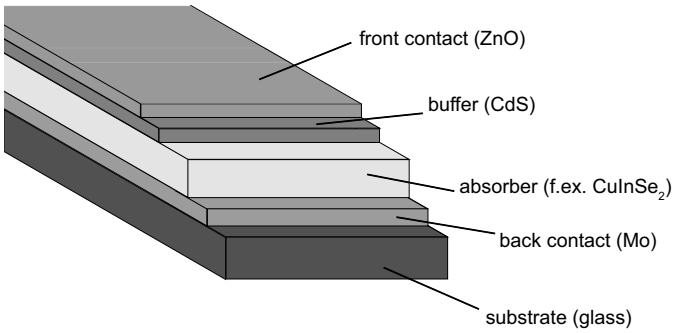

Figure 2.1: cross section of solar cell

photons, no generation of electron-hole pairs is possible, the excess of photon energy over the energy band gap E_G is lost in the form of heat energy (Fig. 2.1). New device concepts are developed aiming in the increase of the efficiency [15]. By the combination of cells from different materials absorbing different spectral ranges of light, it is possible to reduce this energy loss (multispectral/tandem solar cell). Appropriate materials for the realization of this thin film technology is the combination of $CuInSe_2$ (or $Cu(In, Ga)Se_2$) with $CuGaSe_2$ as top cell. The theoretical efficiency of these devices is estimated by 38%, however, further loss mechanisms reduce these predicted values. $CuInSe_2$ and $CuInS_2$ absorbers show efficiencies higher than 15% [3], whereas the efficiency of $CuGaSe_2$ is still much lower by 10% [4]. Another innovation in this direction was accomplished by a further increase of the bandgap by the partial replacement of In with Ga [16] which increases the bandgap of the absorber from 1.04 eV to 1.1-1.2 eV. In this range the highest absorption is obtained (Fig. 2.2). In between the efficiencies of $Cu(In, Ga)Se_2$ cells lie by 19% [2, 17]

An important factor limiting the efficiency is the limited mobility and diffusion length of the generated carriers due to recombination effects [18]. In $Cu(In, Ga)Se_2$, $CuInSe_2$ and $CuGaSe_2$ solar cells the dominant recombination path is in the space charge region of the absorber. However, in $CuGaSe_2$ cells there is a much higher contribution of tunneling resulting in a higher recombination loss. Only $CuInS_2$ shows different recombination mechanisms [19]. In the dark recombination takes place mainly via bulk states with a

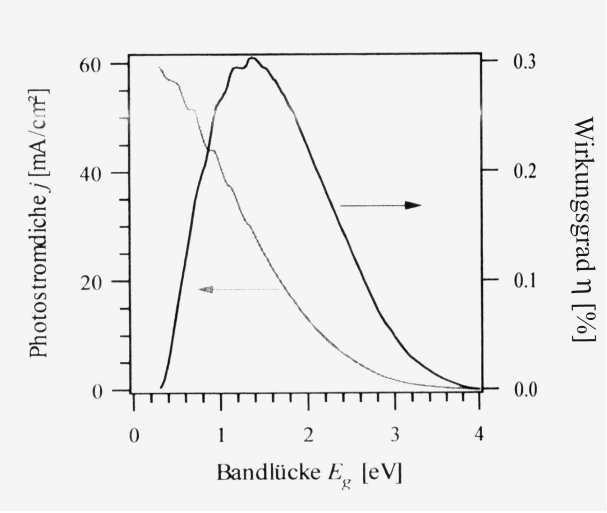

Figure 2.2: maximal possible current density and maximal possible efficiency as a function of the semiconductor bandgap for ideal conditions [20]

strong tunneling contribution. Under illumination recombination is thermally activated and occurs via interface states.

The theoretical efficiency is further decreased by band gap fluctuations and electrostatic potential fluctuations [18]. Band gap fluctuations are due to composition variations. However, the main role play electrostatic potential fluctuations due to the inhomogeneous distribution of charges deriving from structural defects, doping atoms and impurities met in polycrystalline solar cells. Therefore continuous efforts are made to decrease the electric inhomogeneity.

Many investigations are concerned with the formation of the built-in potential and particularly the interface formation, as an appropriate band line-up at the interface decreases interface recombination [21]. The differences between the chalcopyrites are least clear and a definite model has still to emerge [22].

Thus, further studies of the interface recombination and the related atomic defects, as well as the band offset are required. The comprehension of the interface structure can considerably contribute in this task, as it determines the efficiency to a significant extent. Besides, the determination of the "ideal" surface structure of epitaxial layers can serve as a model for the understanding of grain boundaries in polycrystalline films. Also the growth control of epitaxial layers and consequently their quality can then be improved.

3 Bulk properties of Chalcopyrites

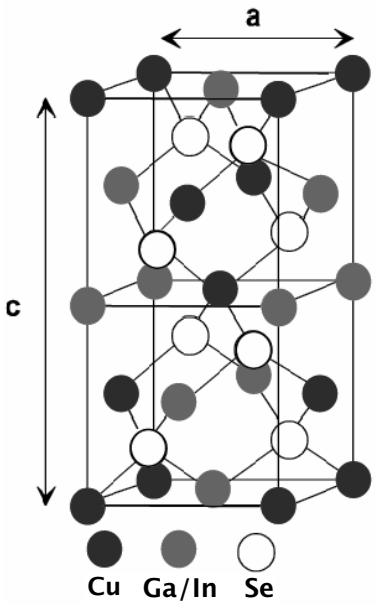

Figure 3.1: Chalcopyrite crystal structure

Before dealing with the surface properties of chalcopyrites an overview of the related bulk properties will be given. Chalcopyrites ABC_2 are the isoelectric analogon to zinc-blende materials. Thus their bonding is of mixed covalent and ionic character, as well. However, the presence of two cations, A and B, instead of one cation like in zinc-blende materials distinguishes the properties of chalcopyrites from the properties of zinc-blende materials. The chalcopyrite structure can be seen as a superlattice of the zinc-blende structure. Each anion C is coordinated by two A and two B cations, whereas each cation is coordinated by four anions. Thus, the unit cell of chalcopyrites has the double size in the c-direction in comparison to the zinc-blende materials (Fig. 3.1) and two different

cation sublattices are present. As a further consequence the unit cell is tetragonally distorted by a distortion parameter which is the ratio between the lattice parameters $\eta = \frac{c}{2a}$ and differs from one. The anions are displaced from their ideal tetrahedral site by an amount u. Whereas the valence bands of most zincblende crystals are composed of s- and p-like orbitals, the noble metal d-levels of chalcopyrites hybridize with the otherwise s- and p-like orbitals, resulting in the modification of their energy band structure [**?**]. Thus, the band gap of chalcopyrites is much smaller and shifts to lower energies in comparison to the binary analogs. This effect is known as "band gap anomaly". Actually this strong red shift of the bandgap makes chalcopyrites such strong absorbers of sunlight.

3.1 Electronic properties

Particularly by means of calculations with the potential-variation mixed-basis approach the origin of the band gap anomaly by comparison to the binary analogs was localized [23, 24] in two effects: The p-d-hybridization effect results from the repulsive p-d-interactions in the valence band associated with the Cu-d orbitals. On the other hand, the anion displacement u in the chalcopyrite crystal influences the band gap by the so called structural factor. In the example of $CuInSe_2$ each anion has two different cations as nearest neighbors, the Cu cation with one valence electron and the In cation with three valence electrons. Consequently the charge density on the Cu-Se bond is lower than on the In-Se bond. In order to compensate this electrostatical inbalance, the Se atom is slightly displaced towards the Cu atom. As a result the Cu-Se bond is shorter than the In-Se bond and the bond charges are modified. As the valence band is dominated by Cu-Se contributions, the change in the bond charges has an impact on the total band gap.

These observations can be better illustrated by considering the electronic structure calculated with the potential-variation mixed-basis approach by Jaffe et al. [25], as well as the electronic charge density of chalcopyrites calculated with Slater-type exchange by Jaffe et al. [23]. The electronic band structure is shown in Fig. 3.2 for the case of $CuInSe_2$. The upper valence band is dominated by bonding Cu d and Se p states.

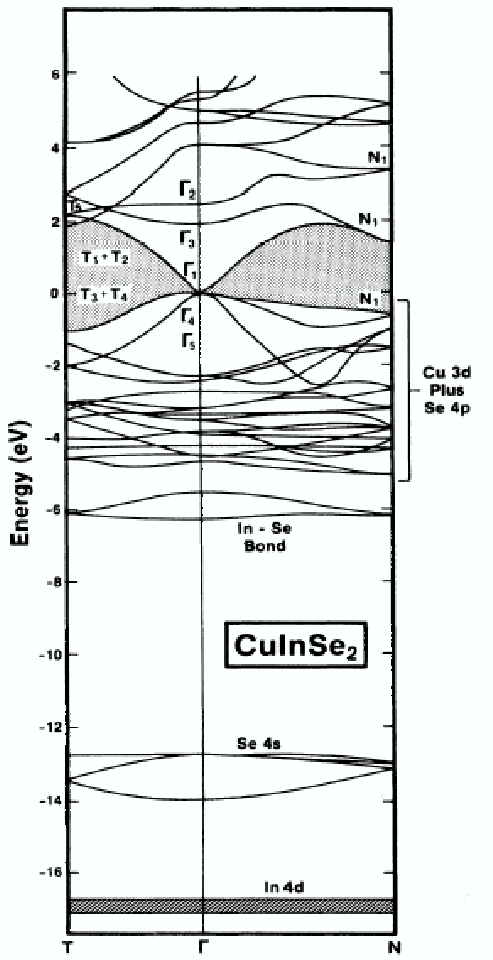

Figure 3.2: Band structure of $CuInSe_2$ as calculated with the potential-variation mixed-basis (PVMB) approach and illustrated by [25].

Towards lower energies the In-Se band is seen which has a weaker bond. Below -8eV the Se4s band appears. In Fig. 3.3 the charge densities of the major valence subbands of Fig. 3.2 are depicted. In the upper valence band (Fig. 3.3a) the covalent character of the Cu-Se bonding is illustrated, as well as the non-bonding character of the In-Se contact. Fig. 3.3b corresponds to the In-Se and Cu 3d bands. Cu has a nearly spherical charge, while the In-Se bond shows a partially covalent bond charge which is however ionically polarized towards the Se site. In the Se 4s band there is an extendend s-like distribution around the Se-site. Thus the Cu-Se contact is covalently bonded with a significant ionic

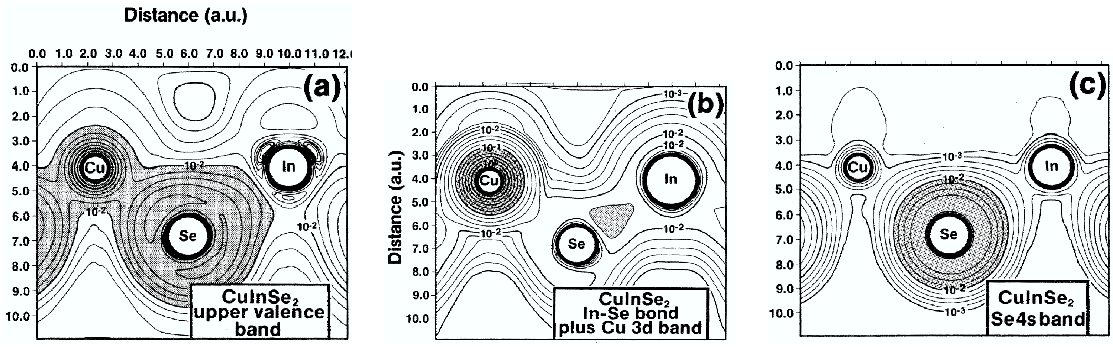

Figure 3.3: Charge densities for the three major valence subbands of $CuInSe_2$ with a) upper valence band, b) In-Se and Cu-d subbands, c) Se s subband as calculated and illustrated by [23] with Slater-type exchange.

component, while the In-Se contact appears as nonbonding. In does not form a strong bond with Cu as well. The role of Cu is important, as it contributes significantly to the charge in the upper valence band and is responsible for the mentioned p-d-hybridization. The band structure and the bondings between the different elements are correlated with the formation of defects and defect structures.

3.2 Defects

A further feature of chalcopyrites resulting from the presence of two different cations is their structural tolerance to large off-stoichiometry in contrast to zinc-blende compounds. Smaller deviations from the ideal stoichiometry (up to 0.1 at%) are compensated by the formation of point defects. While III-V compounds are doped by intention, the intrinsic defects of chalcopyrites are already important for the doping of these materials. $CuInSe_2$ and $CuInS_2$ can be either n-type for Se-poor or p-type for Se-rich stoichiometries, however, $CuGaSe_2$ is reported to be p-type for all compositions [22]. Thus, it is possible to influence the formation of different defects by the composition. Calculations with first-principles self-consistent electronic structure theory also showed the Cu vacancy to be the dominating acceptor [26]. In fact, Cu is known to have a high mobility in Cu chalcopy-

rites [27]. Other possible defects are In vacancies, In_{Cu} and Cu_{In} antisites as well as Cu_i interstitials. However, the defect formation energy is not always constant but varies with the Fermi energy as well as with the chemical potential of the particular atomic species. For example Cu vacancy acceptors V_{Cu}^{-} form more easily in n-type material, while In_{Cu}^{2+} donor states form more easily in p-type material. Besides, the pairing of defects plays an important role as it can actually change the electrical activity. Whereas an isolated V_{Cu} acts as an acceptor and an isolated In_{Cu} as a donor, a pair of both these defects gets electrically inactive. Namely during the interaction of two defects situated close to each other, electrons are transfered from donor to acceptor levels. The charge defects are attracted with Coulomb interaction and atomic relaxation takes place. Pairs with the lowest formation energies were calculated to be the $(2Cu_{In}^{2-} + In_{Cu}^{2+})$ and $(2V_{Cu}^{-} + In_{Cu}^{2+})$. With the formation of these defect pairs also the appearance of secondary phases was explained such as $CuIn_3Se_5$ and $CuIn_5Se_8$. Photoluminescence measurements of $CuInS_2$ and $CuGaSe_2$ were interpreted with donor-acceptor pair (DAP) recombination emission of interstitial Cu atoms as donor defects and cation vacancies as associated acceptor defects [28, 29]. According to later experiments on $CuGaSe_2$ the observed DAP transitions rise from a donor and two shallow acceptors [103, 31, 32]. However their defect chemical origin is not clarified yet. Thus it is not trivial to identify experimentally the atomic species involved in the formation of defects and further research in this area is required.

3.3 Competing ordering structures

In chalcopyrites like in other semiconductors also the coexistence of domains of a few types of ordered structures in the same sample is possible. Near the chalcopyrite structure which is the stablest in room temperature, also other structures are possible like the Cu-Au and the CuPt-ordering. The names derive from metal alloys which show the corresponding ordering structures [33]. The most relevant is the Cu-Au ordering which consists of alternating (100) planes occupied solely with Cu or In/Ga atoms respectively (Fig. 3.4). According to ab initio calculations the formation enthalpy difference between the chalcopyrite and the CuAu phase is very small (2 meV/atom) for $CuInS_2$, while it is

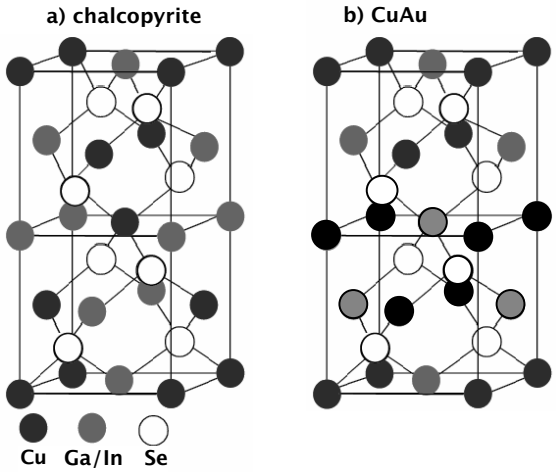

Figure 3.4: Cu-Au ordering in comparison to chalcopyrite structure: The Cu-Au ordering consists of alternating (100) planes occupied solely with Cu or In/Ga atoms respectively

large (9 meV/atom) for $CuGaSe_2$ [34, 35, 36]. Likewise, the CuAu ordering was found experimentally in coexistence with the chalcopyrite phase in $CuInS_2$ [37] and $CuInSe_2$ [38], while in $CuGaSe_2$ only the chalcopyrite phase appears [39, 36, 40].

The defect structures observed in the bulk of chlacopyrites could be also associated with structures observed on the corresponding surfaces. Tendencies in the formation of defects in the bulk are correlated with thermodynamics of surfaces and the observed reconstructions. Thus, the knowledge of the bulk properties can contribute in the interpretation of surface effects. Vice versa, the formation of surface structures may be responsible for the generation of bulk structures during crystal growth or epitaxy. Thus, knowledge and control of surface structures may be important to optimize and to direct crystal structures for chalcopyrite bulk and layer materials.

4 Chalcopyrite surfaces

4.1 Surface reconstructions of semiconductors

The absence of neighbouring atoms on a crystal surface results in the modification of the interatomic forces at the surface. The equilibrium conditions for the surface atoms change so that they can be displaced with respect to their position in the bulk in order to minimize the surface energy [41].

Particularly the atoms of tetrahedrally bonded semiconductors (Si, Ge, binary, chalcopyrites) form sp^3 hybrid orbitals in the bulk. The overlap of the wavefunctions of the neighbouring atoms results in two possible energy levels: the lower energy level corresponds to the so called bonding orbital (valence band), while the higher to the antibonding orbital (conduction band). The electrons participating in the hybridization are distributed on the valence band. Due to the Pauli principle each binding orbital can be occupied only by two electrons. [42]. This bonding has a strongly directional character so that free dangling bond orbitals remain on the surface, each occupied with one electron. In order to decrease the surface free energy, the electronic charge at the surface is redistributed. Due to the lack of neighbouring atoms on the surface, there is no overlap of the sp^3 orbitals so that electronic states are possible also inside the energy gap. The surface atoms undergo a rearrangement [43]. If the surface atoms are only slightly displaced, the periodicity of the surface remains the same as in the bulk, resulting in a surface relaxation. By a displacement of the surface atoms more complex than a pure shift normal to the surface, the free dangling bonds can be saturated by forming new bonds within the surface, leading to a surface reconstruction which modifies the periodicity of the surface.

From a more simplified point of view the occurence of relaxation or reconstruction depends on the stoichiometry of cations and anions and the resulting charge on the corresponding surface. Consequently covalently bonded semiconductors form either polar surfaces with an unequal number of cations and anions on the surface or nonpolar surfaces with an equal number of cations and anions.

The determination of reconstructions can be a complicated task. The combination of several experimental techniques and theoretical calculations is usually nescessary in order to propose possible structures for a particular surface. For the III-V and II-VI semiconductors a variety of different reconstructions is already known, depending on the preparation of the surfaces. However, the knowledge of the thermodynamical stability of chalcopyrite surfaces is still very limited. As the ionicity value of chalcopyrites is similar to the ionicity value of zinc-blende materials, the ionic bonding character of chalcopyrites roughly resembles the one of zinc-blende materials. Thus, the comparison to the well-known zinc-blende surfaces can be helpful in the study of chalcopyrite surfaces.

4.2 Reconstruction models of the (001) surface

As far as zinc-blende materials are concerned, the (110) is a nonpolar surface. As a consequence the (110) surfaces undergo a relaxation, but no reconstruction. In contrast, the polar (001) and (111) surfaces reconstruct in order to neutralize the polar surface charge resulting from the unequal number of cations and anions on the surface. The sp^3 dangling bonds of GaAs and ZnSe are partially filled on the surface as long as no reconstruction is formed. As far as the bulk is concerned, the dangling-bond energy level of the electropositive element (Ga or Zn) is situated in the conduction band and is empty, while the dangling bond energy level of the electronegative element (As or Se) lies in the valence band and should be filled. This equilibrium condition is also seeked on the surface. Therefore electrons move from the dangling bonds of the electropositive element to the dangling bonds of the electronegative element. The Ga/Zn dangling bond becomes more sp^2-like whereas the As/Se bond gets more p_z character resulting in the different shifts of the corresponding atoms. Especially for the GaAs and ZnSe (001) the

electron counting model has been developed, enabling the prediction of possible surface reconstructions [44]. In order to obtain a semiconducting surface, the number of available electrons at the surface should exactly fill all dangling bond states in the valence band. Thus, according to the electron counting rule the lowest energy structure is obtained with filled dangling bonds on the electronegative element and empty dangling bonds on the electropositive element. A general structure model was developed satisfying this condition consisting of dimers and missing dimers. It is based on assumptions about the nature of GaAs (001) reconstructions obtained from STM images [45, 46]. The dimer reconstruction has consequently a $(2 \times \mathrm{N})$ symmetry. The $(2\times)$ periodicity derives from the dimers, while the $(N\times)$ periodicity from missing dimers (Fig. 4.1). For GaAs with three and five valence electrons respectively a (2×4) structure is the simplest possible one. The odd number of electrons makes also missing dimers necessary in order to fill all dangling bonds. In the case of ZnSe each cation has two valence electrons, while each anion six valence electrons. Therefore each atomic orbital contributes on average 1/2 or 3/2 electrons to each bond. The even number of valence electrons enables a higher symmetry so that already simple dimer structures satisfy the electron counting rule. For the Se-rich (001) ZnSe surface, a (2×1) reconstruction is predicted, which has been in fact experimentally observed. However the electron counting rule only predicts the simplest possible surface structures formed with dimers on these surfaces. Other more complicated structures are not excluded and were also experimentally obtained on the GaAs and ZnSe (001).

4.3 ZnSe (001) reconstructions

First-principle total-energy calculations for the ZnSe (100) surface predicted additional surface structures formed not only by dimers, but also by surface defects like vacancies [47, 48], which were mostly also experimentally confirmed [49, 50]. The possible surface structures were calculated as a function of Zn or Se coverage and Zn or Se chemical potentials [47]. As already mentioned, simple dimer structures are metastable for ZnSe (100) surfaces. Se dimers occupy six electrons in the dimer bond which show the be-

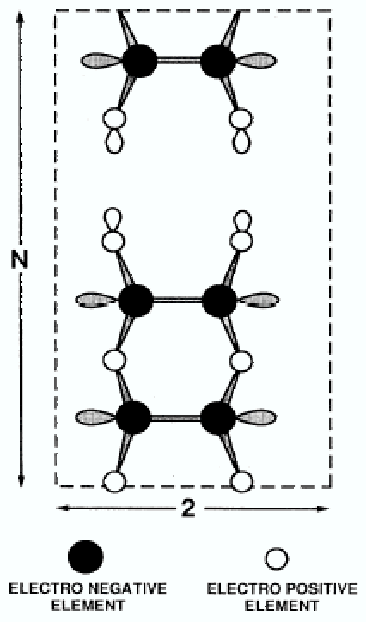

Figure 4.1: $(2 \times \mathrm{N})$ unit cell by [44]: The $(N\times)$ periodicity results from missing dimers. The filled bonds are shaded, while the empty are open.

haviour of π bonds. Vacancy structures are also found to be nonmetallic. Namely the dangling bonds of the anions accept electrons from the dangling bonds of the cations and become fully occupied. This electron exchange is energetically favorable due to the large band gap and ionicity of ZnSe. Zn vacancies are more favourable than Se vacancies, as the Zn-vacancy structure has less dangling bonds than the Se-vacancy structure: After the electron transfer from the dangling bonds of surface Zn atoms into the dangling bonds of the second-layer Se atoms, the Zn atoms relax towards the second layer of Se atoms. The electrons around the surface Zn atoms form an sp-type hybridization which is energetically more favorable in comparison to the σ bond of Zn-Zn dimers. As a result, Zn-vacancy c(2×2) structures are found to be most favourable for the Zn-terminated surface, while Se-dimer (2×1) structures are most favourable for the Se-rich surface. Also more complicated structures consisting of both dimers and vacancies were calculated. The most favourable is a Zn-(4×2) structure as a combination of Se dimers and Zn vacancies (Fig.4.2). Similar results were obtained also experimentally for the

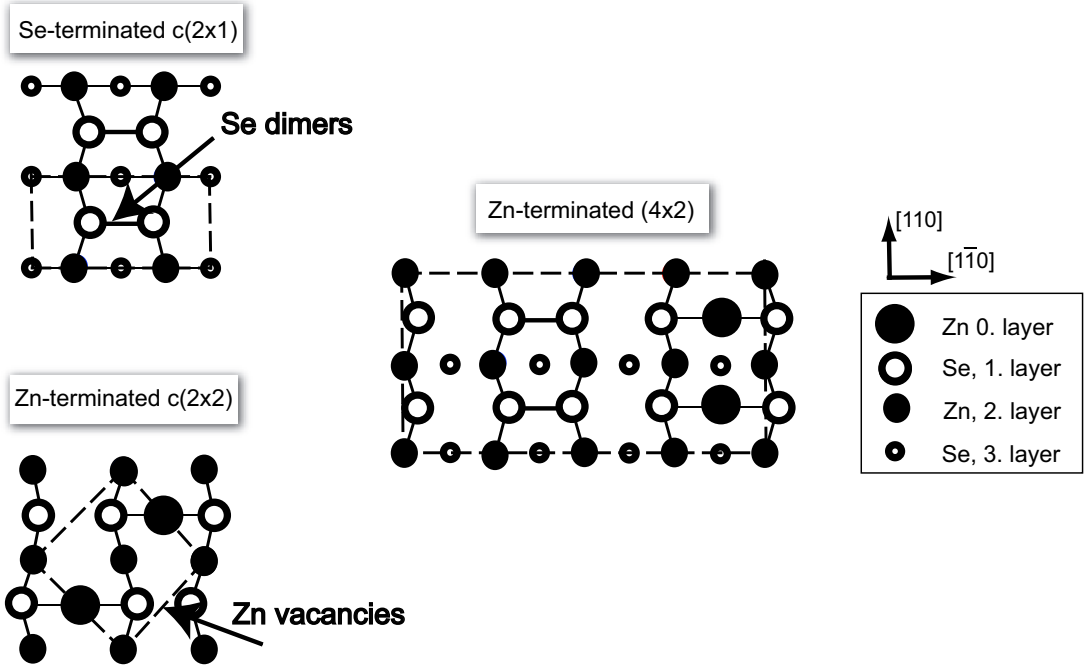

Figure 4.2: model of the Se-terminated (2×1), Zn-terminated c(2×2) structure and Zn-(4×2) structure with $\theta = \frac{1}{4}$ with Zn-vacancies and Se dimers as calculated and illustrated by [47]. The dashed lines show the unit cells for each case.

ZnSe (100) [50]. For the Se-rich surface, a (2×1) reconstruction corresponding to a full monolayer of symmetric Se dimers was obtained, while for the Zn-rich surface a c(2×2) reconstruction corresponding to a half-monolayer of non-dimerized Zn atoms.

4.4 Thermodynamics of chalcopyrite surfaces

Although the (110) surface is the lowest in energy from all zinc-blende surfaces and stable towards the formation of facets, the same conclusion cannot be drawn for chalcopyrites. Namely the presence of two different cation types instead of one favours the formation of charge neutralizing defects [51]. Jaffe et al. predicted by pseudopotential LDA calculations that the polar (112) surface of $CuInSe_2$ is much more stable than the nonpolar (110) surface. According to these calculations the (112) surface is stabilized by Cu vacancies V_{Cu} under Cu-poor conditions or by Cu on In antisites Cu_{In} under In-poor

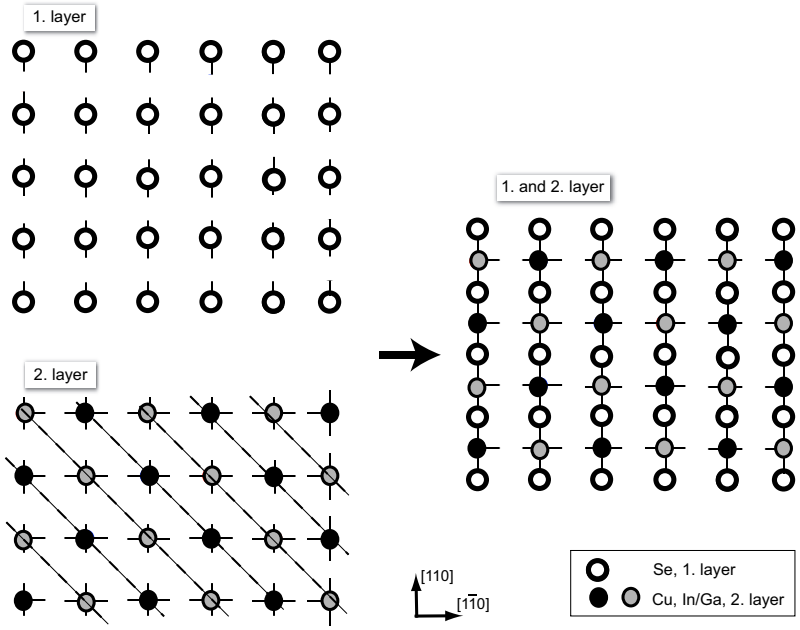

Figure 4.3: Ideal (001) chalcopyrite surface, consisting of alternating layers of Se atoms or Cu and Ga/In rows. On top left the first Se atoms is shown, while on bottom left the second layer of Cu and Ga/In rows. The Cu and Ga/In rows are marked with dashed lines along the [100] direction. On the right the both layers are superimposed.

conditions. The ($\overline{112}$) surface is stabilized by In on Cu antisites In_{Cu}. By this approach it is possible to explain the experimentally observed formation of facets of the polar (112) and ($\overline{112}$) surfaces when trying to grow nonpolar surfaces. Similar results were obtained by Zhang et al. [52] with first-principles total-energy calculations. The (112) and ($\overline{112}$) surfaces were found to be the most stable and a number of structures was proposed on base of TE-calculations. Thus, the (112) surfaces can be self-compensated with intrinsic defects that are p type in the bulk (V_{Cu}, Cu_{In}, V_{Cu}) and the ($\overline{112}$) with intrinsic defects that are n type in the bulk (In_{Cu}, Se antisites). The ideal (001) chalcopyrite surface consists either of Se atoms or of alternating rows of Cu and Ga atoms, as illustrated in Fig. 4.3. Consequently it is polar and it could also reconstruct, however no relevant calculations are reported.

Few experimental results can be found in the literature about chalcopyrite surface re-

constructions, nevertheless the theoretical predictions from the above are experimentally confirmed. The latest investigations were performed by Hunger et al. [53] on $CuInS_2$ layers grown on Si-substrates with MBE. The samples were investigated immediately after growth with LEED. The (112) face was found to be the most stable, showing a (2×1) superstructure with respect to a hexagonal surface unit cell. The (2×1) superstructure was attributed to cation ordering of CuAu-type, characterized by an alternating occupation of the (001) planes by exclusively Cu or In. The $CuInS_2$ (110) face showed complete faceting into (112) and $(\overline{112})$ facets. The (001) face was also investigated, however for Cu-rich growth conditions it seemed to be unreconstructed, while for near stoichiometric growth conditions partial faceting into (112) facets was observed.

4.5 Surface phases

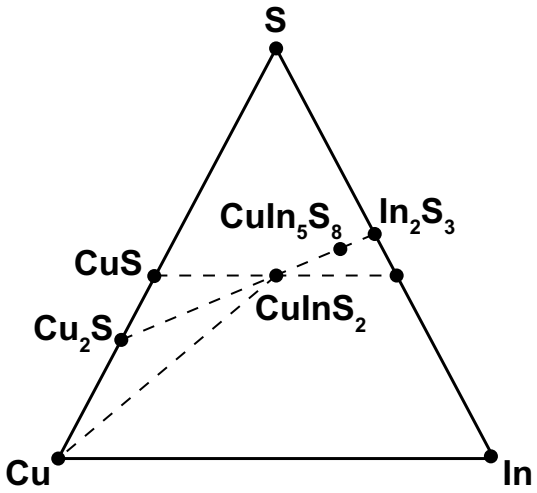

Figure 4.4: Gibb's phase triangle of the ternary Cu-In-S system with the existing binary and ternary phases, according to Binsma et al. [54]

Apart from reconstructions also phases with different crystallographic structures are expected on chalcopyrite surfaces, depending on their bulk and surface stoichiometry. An important parameter related to the surface stoichiometry is the surface cation ratio $y = B_{III}/(B_{III} + Cu)$ with B_{III}=In or Ga. If $y < 0.5$ the surface is Cu-rich, while for

$y > 0.5$ the surface is Cu-poor. For $y > 0.52$ no more point defects are formed in order to compensate the Cu deficiency, as mentioned in section 3.2, but also additional secondary crystal phases can form. Such binary or ternary phases are shown as they can appear in dependence of stoichiometry on the Gibb's phase triangle in Fig. 4.4 according to Binsma et al. [54] for $CuInS_2$. These phases are mostly observed on the surface rather than in the bulk, as they arise from intrinsic or extrinsic bulk defects which diffuse to the surface by forming other stable crystallographic structures. Preferential segregation may for example take place by different ionic sizes of the constituents or as a cause of band bending [55].

For Cu-rich $CuInS_2$, $CuInSe_2$, and $CuGaSe_2$ the formation of a $Cu_{2-x}Se$ phase is always observed on the surfaces of both epitaxial and polycrystalline layers [56, 57, 58, 59, 60, 62, 116]. On the other hand, Cu-poor polycrystalline $CuInSe_2$ and $CuInS_2$ films decompose into $CuIn_3Se_5$ [57, 56] or $CuIn_5S_8$ [58] respectively. The $CuIn_3Se_5$ phase corresponds to a surface cation ratio of $y = In/(In + Cu)_{surf} = 0.75$. For the Cu-poor surface of polycrystalline $CuGaSe_2$ a $CuGa_5Se_8$ phase was reported [57]. However, no $CuIn_3Se_5$ or $CuIn_3S_5$ was observed on epitaxial $CuInSe_2$ [61] and $CuInS_2$ [62] respectively despite their Cu-poor bulk and surface composition. Only after 4 keV of N^+ sputtering and annealing at 650 °C of single crystal $CuInSe_2$, the formation of $CuIn_3Se_5$ was observed [63]. As far as stoichiometric bulk compositions are concerned, for epitaxial [64] $CuInSe_2$, $CuInS_2$ [53] and cleaved [65] $CuInSe_2$ crystals no deviation of the surface composition was observed as well. In contrast, even for stoichiometric bulk compositions of polycrystalline $CuInSe_2$ secondary phase segregation occurs [57]. Thus, polycrystalline chalcopyrites form more easily surface phases as epitaxial or single crystalline chalcopyrites, especially on the Cu-poor side.

5 Surface characterization/experimental methods

In this chapter the experimental methods used to characterize the chalcopyrite surfaces will be introduced. The experiments were held out in standard analysis chambers under Ultra-High-Vacuum (UHV) conditions equipped with different surface sensitive-analyzing and characterizing tools, as well as an Ar^+ ion sputtering gun for the preparation of the surfaces. The first stage of experiments aiming to optimize the surface preparation took place in a laboratory UHV system at the TU Berlin. This system was equipped with LEED, AES, sample heating at a base pressure in the $< 10^{-11}$ mbar range. The samples were mounted on a molybdenum sample holder and transferred into the vacuum system. The temperature of the sample was measured with a Ni-Cr-Ni thermocouple. The second stage of experiments focusing on the characterization of the prepared surfaces was carried out at the BESSY II synchrotron storage ring at the U49/2-PGM2 and UE56/2-PGM2 beamlines. Before and after each preparation step the samples were characterized by synchrotron-excited high resolution photoelectron spectroscopy . The experimental stations, SoLiAS and MUSTANG respectively, were equipped with a Phoibos 150 analyzer and sample stage allowing for simultaneous sample heating, Ar^+ ion bombardment at a base pressure of $< 10^{-9}$ mbar. The AFM measurements took place ex-situ.

5.1 Surface sensitive methods

When an electron or X-ray beam strikes the surface of a solid, it penetrates it to a depth of some μm so that atoms of the solid are ionized. The created electrons have a high probability of being inelastically scattered. Thus, the distance they can travel through the solid is limited by electron-electron collisions so that only electrons from the vicinity of the surface are finally ejected out of the solid. This effect accounts for the high surface sensitivity of XPS and AES, which provide qualitive and quantitive information about the chemical species present in the vicinity of the surface. In the case of LEED the incident electron beam has a particularly low energy. The incident electrons have a high probability of being elastically backscattered so that they can be detected and give information about the periodicity of the surface structure in the vicinity of the surface.

A characteristic value for the surface sensitivity is the electron mean free path λ, defined as the distance the electrons travel in the material before being inelastically scattered. The electrons flux decays exponentially as a function of distance from the point they have been created. The electron mean free path has been measured for different materials [66] and there proves to be a universal curve (Fig. 5.1). For energies >100 eV the primary electrons loose their energy with electronic collective excitation (for example plasma excitation). In this energy range the curve describes well all materials. With increasing energy the curve can be described by the relation

$$\lambda \sim \sqrt{E}$$

For energies < 30 eV rather one-electron excitation takes place and thus the electron mean free path can slightly vary between isolators and metals. In the range of 10 to 500 eV electrons have the shortest inelastic mean free path of about 1 nm [43]. Thus, the information obtained in this energy range derives from the electrons of the upper atomic layers and provides the highest surface sensitivity.

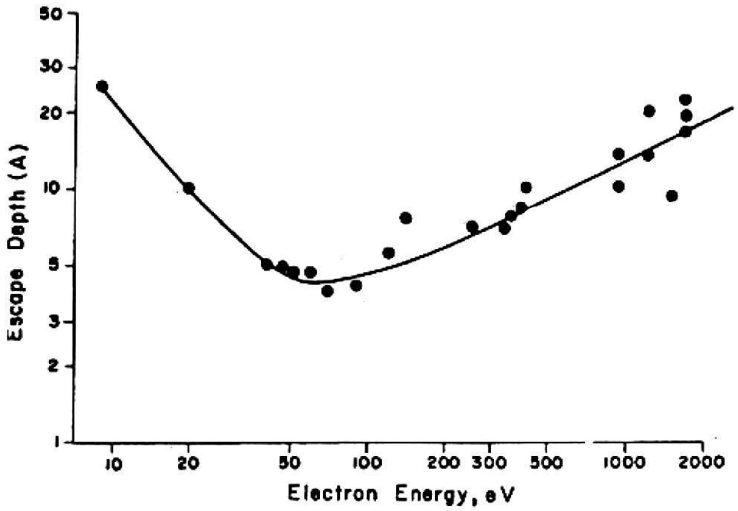

Figure 5.1: Inelastic mean free path of electrons in dependence from energy. The highest surface sensitivity is obtained in the energy range between 10 and 500 eV, in which the inelastic mean free path of the electrons is in the order of only 1 nm.

5.2 Auger Electron Spectroscopy

Auger Electron Spectroscopy is based on the principle of the ionization of core levels. It is applied for the identification of contaminations and particular elements on surfaces, as well as for the determination of the elemental composition. During an Auger process, a core level, e.g. the K level as shown in Fig. 5.2, is ionized by an incident electron with an energy $E_p \gg E_k$. As a result a hole is created in the level K. In order to fill the hole the atom relaxes with a transition from an outer level, e.g. E_{L_1}. The excess kinetic energy originating from this transition ($E_k - E_{L_1}$) is released in two different ways. Either it appears as an X-ray photon at that energy or it is transfered to an other electron on a same or a more shallow level. In the second case the electron is consequently ejected and an Auger emission is induced. The relative probability of an Auger emission to occur is much higher than that of X-ray fluorescence for relative shallow core levels and consequently for elements of a lower atomic number. The Auger transition is denoted

by the electronic levels involved, where $KL_1L_{2,3}$ represents a transition with the energy of the Auger electron

$$E_{KL_1L_{2,3}} = E_K - E_{L_1} - E_{L_{2,3}}. \tag{5.1}$$

E_i are the binding energies of the ith atomic energy levels. As the Auger energy depends only on atomic energy levels its analysis enables the definite identification of chemical elements [67].

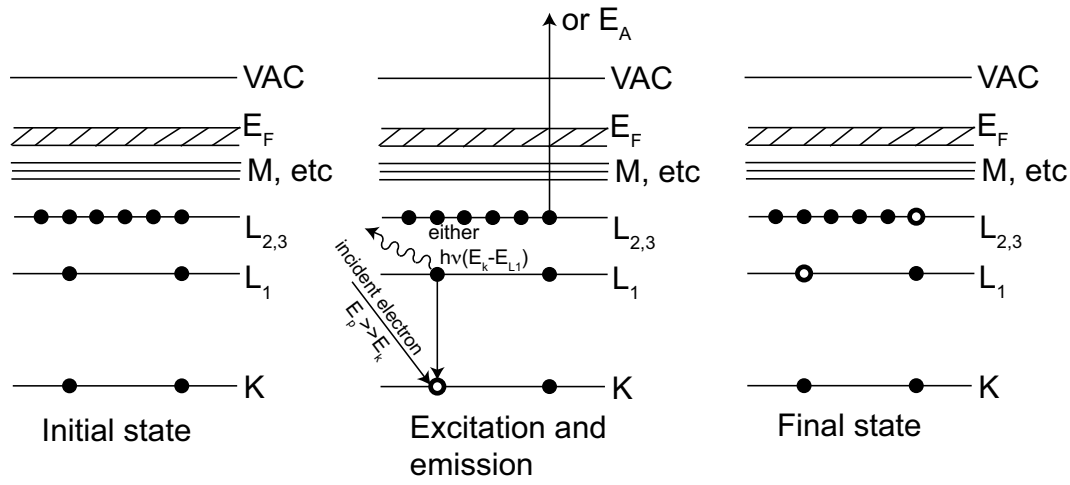

Figure 5.2: During an Auger process (illustration by Briggs et al. [67]) an incident electron with an energy $E_p \gg E_k$ generates a hole in the K core level. The hole is filled with an electron from the L_1 level by emission of a X-ray photon, or by transferring this energy to an electron of a higher shell, for example $L_{2,3}$. Thus, the electron receiving the energy is ejected.

In order to assign the experimentally observed energy peak positions to the corresponding elements, tables with semi-empirically determined Auger energies are available. The spectra in these atlas are however shown in the differential mode EdN(E)/dE. This mode is preferred as Auger peaks on the energy mode are superimposed on a relatively large background deriving from secondary electrons. This background is separated via electronic differentiation.

With AES relative surface quantities can be easily determined, too, as the emission

current of Auger electrons is proportional to the number of excited atoms and consequently also the peak to peak height of the differentiated Auger line. The percentage relative surface concentration of the different elements can be calculated according to the formula

$$C_x = \frac{\frac{I_x}{S_{x,Ag}}}{\sum_a \frac{I_a}{S_{a,Ag}}} \tag{5.2}$$

I_x is the peak-to-peak height of the element X, $S_{x,Ag}$ the relative sensitivity of the element X normalized to Ag [68]. The sum is taken over one peak from each element present on the surface. Relative sensitivities can be also obtained from tables. The accuracy of this formula is limited, as the Auger electron escape depth of the measured material may be differ from that of the standard material.

The evaluation of the Auger intensity ratios can be also applied at the determination of growth mechanisms during the growth of thin layers. When the arrangement of the surface atoms with respect to the substrate atoms does not change with increasing coverage, the Auger intensity of the substrate emission declines exponentially with increasing layer thickness. Particularly, the intensity I of the Auger electrons is:

$$I/I_0 \propto e^{-d/\lambda} \tag{5.3}$$

whereby d is the thickness of the grown layer, λ the inelastic mean free path and I_0 the intensity of the Auger signal of the uncovered surface. The gradient of the relative AES ratio is characteristic for the growth modus.

As far as the instrumentation is concerned, an electron gun is used for the primary excitation with energies of 3-5 keV. The Auger electrons emitted from the sample surface enter the cylindrical mirror analyzer so that only electrons of a particular energy are detected by an electron multiplier.

5.3 LEED

LEED provides information on the symmetry and periodicity of the surface structure of crystals. The set-up is quite simple and comprises a low energy electron beam striking

the sample surface. The wavelength of the electron beam lies in the same order as the grid constant of the investigated crystal. Therefore interference can take place and the backscattered electrons are made visible on a spherical fluorescent screen. The diffraction pattern observed on the screen is a direct representation of the reciprocal lattice of the surface, as it can be demonstrated graphically by the Ewald-sphere construction.

For this purpose the reciprocal space of the two-dimensional ideal crystal surface is drawn with a set of rods perpendicular to the crystal surface (Fig. 5.3) [69]. The wavevector $\vec{k_0}$ of the incident electron beam proceeds along the rods for the simplest and common case of normal incidence. For elastical scattering $k_0 = k$ applies. According to the momentum conservation the reciprocal grid vector $\vec{G}$ is given by $\vec{G} = \vec{k_0} - \vec{k}$. Subsequently the Ewald sphere is drawn with its center at the beginning of the vector $\vec{k_0}$ and with a radius of k_0. Therefore the directions of the scattered beam vectors $\vec{k}$ are determined by the intersections of the Ewald sphere with the rods which consequently give the diffraction spots, too. By increasing the electron energy, the wavelength is

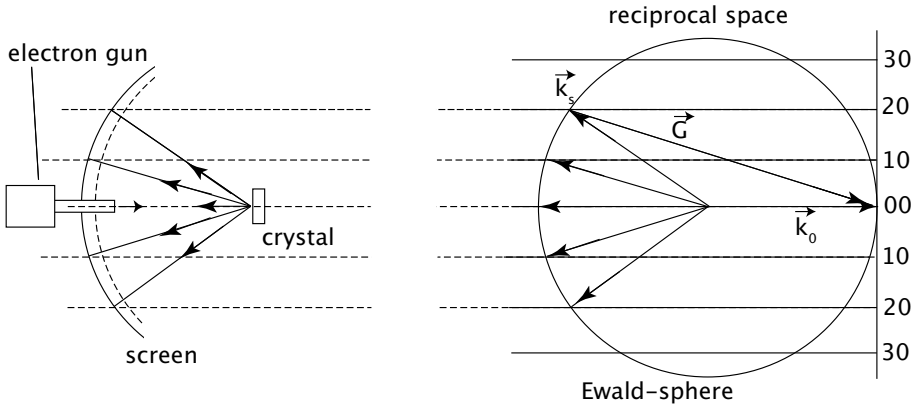

Figure 5.3: Correlation of the LEED diffraction pattern with the Ewald construction in reciprocal space (illustration by Henzler [43]). For incident incidence the LEED pattern observed on the screen corresponds to the projection of the Ewald sphere along the reciprocal rods, thus it corresponds to the cross-section through the rods of reciprocal space.

decreased and the radius of the Ewald sphere increases. The angle between the scattered beams decreases so that the diffraction spots move closer to each other towards the (00)

spot. The (00) spot does not move with increasing electron energy as it derives from the direct reflexion of the electron beam. Therefore it can be easily identified.

Within this approach it is possible to acquire the geometry of the unit cell. From the position of the diffraction spots the periodicity of the crystal is obtained and reconstructions can be identified. Information about the surface morphology like the presence of steps or facets can be obtained from the profile of the diffraction spots by considering the kinematic approach and implementing a Fourier-transformation. Fig. 5.4 illustrates the construction of the diffraction pattern of a stepped surface out of single terraces and sets of steps by comparing the real and reciprocal space for each case. Fig. 5.4d) in real space arises from the convolution of Fig. 5.4b) and c). According to the convolution theorem Fig. 5.4d) in the reciprocal space results from the multiplication of b) and c). As a result the observed diffraction pattern can be obtained from the intersections of the Ewald sphere with the line segments.

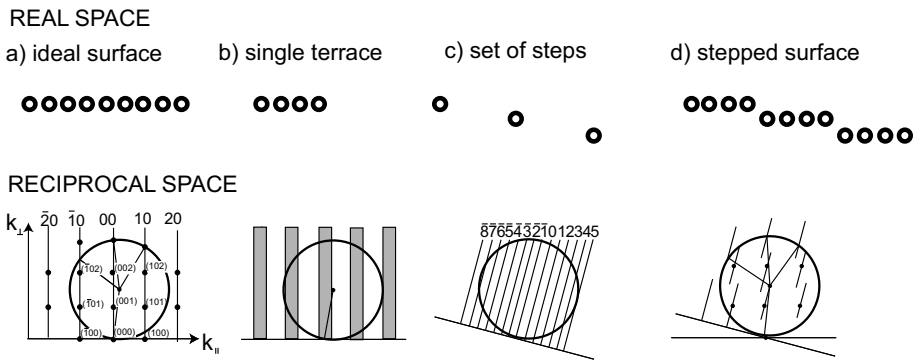

Figure 5.4: Construction of a stepped surface from single terraces and sets of steps (illustration by Henzler [43]).

Facets are defined as domains with a different orientation than the main surface. Like in the example of stepped surfaces it is possible also for facets to predict the corresponding pattern in reciprocal space from the real space. The reciprocal rods corresponding to the facets begin at the same points like the reciprocal rods corresponding to the main surface, as all the facets begin from the main surface as well. However they proceed in different directions, as shown in Fig. 5.5. Accordingly by variation of the electron energy the facet spots move along a particular direction and cross on the screen. From

these directions it is possible to obtain the orientation of the facets in real space. In the same way in the case of a rough surface diffraction spots appear larger in comparison to the sharp spots of a flat, well-ordered surface.

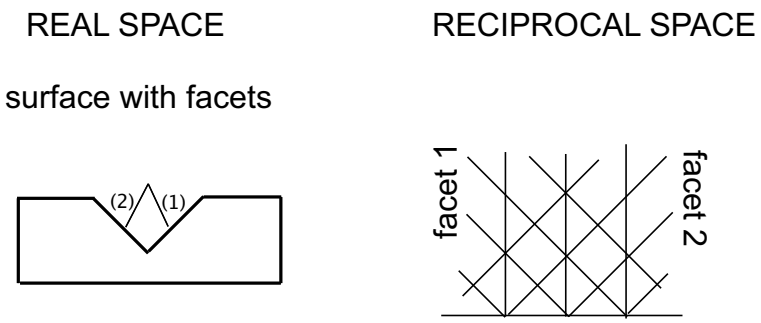

Figure 5.5: Facets in real and reciprocal space (illustration by Henzler [43]). The tilted reciprocal rods correspond to the facets and are perpendicular to the corresponding facet orientation.

5.4 SXPS

SXPS enables apart from the identification of elements the acquisition of the charge distribution of the atoms of this element.

The photoemission process can be adequately described by the three-step model [70]:
1) An electron is optically excited with the energy $h\omega$
2) The electron travels through the solid.
3) The electron escapes through the sample surface into the vacuum with a kinetic energy E_k where it is detected.
The kinetic energy of the ejected electron is given by the equation

$$E_k = h\omega - \phi - |E_b| \tag{5.4}$$

where $|E_b|$ is the binding energy of the corresponding core level and ϕ the work function. In free atoms the binding energy is referred to the vacuum level, in solids however to the Fermi level. The work function is defined as the difference between vacuum level and the Fermi energy of the solid. It can be acquired by calibration towards samples of

well-known work function. The equation is illustrated in Fig. 5.6 where the energy-level diagram is related to the energy distribution of the photoemitted electrons. Electrons deriving from core levels give rise to narrow peaks at kinetic energies below the valence band spectra. The given equation is valid for an elastic photoemission process. However,

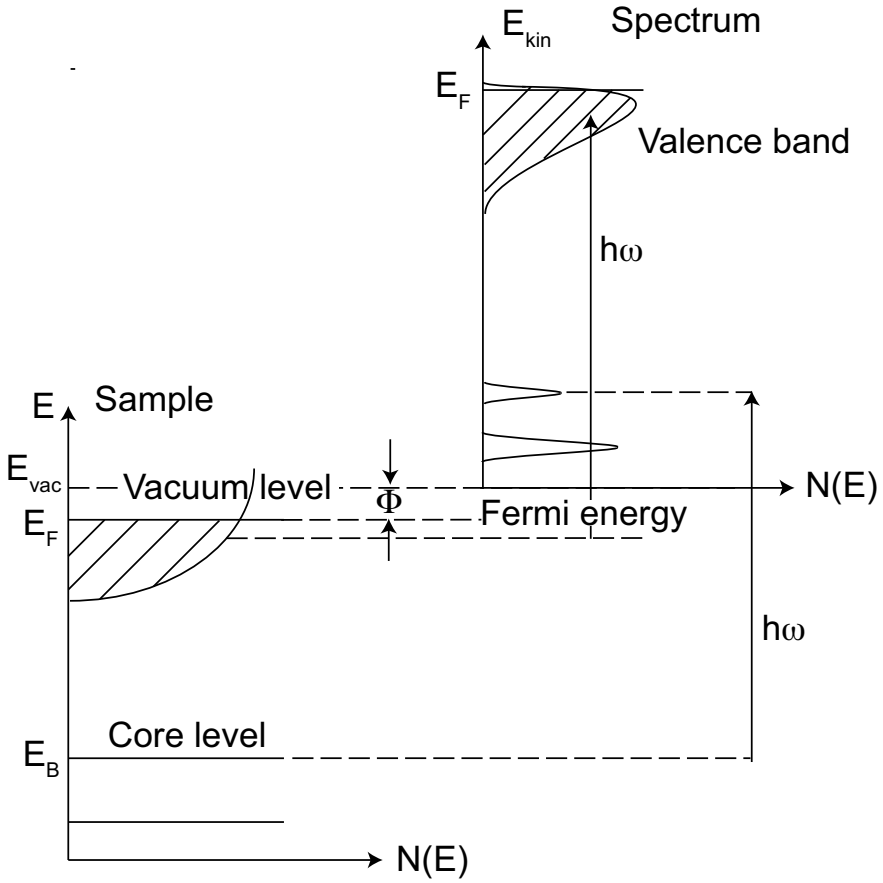

Figure 5.6: Correlation of the energy levels of the acquired spectra with electron energy distribution (illustration by Hüfner [71]). Electrons from core levels correspond to narrow peaks, while electrons from the valence band are associated with the wider band structure. On the real spectra background from backscattered electrons is present, too.

the created photoelectrons can lose energy during inelastic scattering with other electrons before leaving the sample surface. These secondary electrons give rise to background on the measured XPS spectra which increases particularly at lower kinetic energies.

According to the mentioned energy dependence of the inelastic mean free path of Fig.

5.1, the highest surface sensitivity is obtained in the energy range of 10 to 500 eV. As the surface sensitivity also slightly varies along this energy range, it is possible to verify the surface origin of measured components by modifying the energy along this range. With decreasing kinetic energy and increasing surface sensitivity the components decrease in intensity in case they derive from the upper atomic layers. The intensity depends mainly on the photoionization cross section, i.e. the probability of an electron to be excited. The photoionization cross section in turn depends on the main and angular-momentum quantum number. Its values have been directly calculated for different elements, f. ex. by Yeh and Lindau [72].

Theoretically, the generated photocurrent can be described as a result of the excitation of electrons from the initial states i with wavefunction ψ_i to the final states f with wavefunction ψ_f [71]. The photon field is given by the vector potential $\mathbf{A}$. The transition probability is given by the Fermi's Golden Rule $|\Psi\rangle = \sum_i |\phi_i\rangle\langle\phi_i|\Psi\rangle$ as

$$w \propto \frac{2\pi}{h}\langle|\psi_f|r|\psi_i|\rangle^2\delta(E_f - E_i - h\omega). \tag{5.5}$$

The wave functions of the initial and final state which determine the transition matrix element are considered for one electron. On a first approximation it is assumed that the remaining orbitals after excitation are the same in the final state as in the initial state (frozen-orbital approximation). However, for a more accurate calculation it should be considered that after the removal of an electron from its corresponding orbital, the system tends to reorganize the remaining charges so as to minimize its energy.

5.4.1 Final state effects

The creation of a core hole during photoionization can affect the energy distribution of the emitted electrons in different ways. Energetic shifts are measured for the binding energy of the emitted electron, the splitting of peaks is observed or additional satellite peaks can appear.

The energetic shifts are due to relaxation effects. In order to compensate the positive charge of the created hole, negative charge flows towards the generated hole. This negative charge derives partially from electrons of higher shells. As a result, the remaining

electrons are subject to a stronger effective binding energy and their energy levels are slightly reduced. Additional to this so called intra-atomic relaxation effect, also extra-atomic relaxation takes place: The negative charge derives also from eletrons of the other atoms, so that the energy of the hole system decreases.

The observed splitting of peaks is called multiplett splitting and demonstrates the feature of photoemission spectroscopy: The obtained spectra respresent a state with a missing electron instead of the ground state of the measured sample. The emitted electron leaves a hole behind which interacts with the remaining unpaired electrons of the atom. Different spin couplings are possible which influence the energy of the emitted electron as well, resulting in the splitting of the measured spectra. The degree of multiplett splitting as well as the relative intensities of the peaks are associated with the chemical bonding of the corresponding atom and therefore provide respective information.

The reorganization of the electronic structure with the generation of a hole can also induce the formation of additional excited states. Namely during the emission of an electron, a second bound electron can get excited as well by influencing the energy of the first electron and giving rise to additional peaks in the measured spectra, the so called satellite peaks.

5.4.2 Core levels

Core levels are classified according to their principal quantum number number n, the quantum number l of the atomic orbital angular momentum (s, p, d...) and the quantum number s of the atomic spin. The interaction of the orbital angular momentum with the atomic spin is described by the total electronic angular momentum which is the vector sum of the two momenta. If the summation is carried out according to the j-j coupling, the individual spin and angular momenta are added. Consequently for each core level with $l > 0$ two states are possible, the more favourable j=l+s and the less favourable j=l-s for parallel or anti-parallel angular momentum and spin vectors. Thus the core level peaks can have two different values of kinetic energy and appear as doublets. The relative intensity of the doublet peaks is given by the ratio of their respective degeneracies

(2j+1):

$$R = \frac{2(l+s)+1}{2(l-s)+1} = \frac{l+1}{l} \tag{5.6}$$

This intensity ratio has been found to vary experimentally due to changes of the atomic photoionization cross section σ with excitation energy [73] or to diffraction [74] - [76]. The inherent line width of a core level peak depicts the uncertainty in lifetime of the remaining ion state after photoemission. Its Lorentzian form is broadened so that it obtains a Gaussian form due to the experimental resolution of the photon source and the analyzer, as well as from inhomogenities of the sample and local band bending.

5.4.3 Chemical shifts

After a change in the chemical environment of an atom not only the valence charges of this atom are redistributed but also the core levels are affected through the potential change in the area of the atom. Thus a change in the binding energy of the photoemitted electron from the corresponding core level can be measured, the so called chemical shift ΔE_b with

$$\Delta E_b = \Delta E_{chem} + \Delta E_{Mad} + \Delta E_{rel}. \tag{5.7}$$

The first term ΔE_{chem} involves the difference in the electron-electron interaction between the core orbital and the valence charge. The Madelung term ΔE_{Mad} describes the potential of all ionic charges around the particular atom. The last term ΔE_{rel} accounts for the dynamical processes taking place during photoemission which modify the energy position of the measured core level, the already mentioned relaxation effects. As a result the measured binding energy of the emitted electron decreases by this ΔE_{rel} factor, too.

Regarding the high surface sensitivity of SXPS chemically different species of the same atom in the vicinity of a crystals surface can be identified and reconstructions can be determined. During accumulation of positive charge on a surface ion the electrons feel a stronger interaction with the nucleus and their binding energy increases. By accumulation of negative charge on the surface ion the screening effect of the electrons is increased so that the binding energy of the core level electrons decreases.

5.4.4 Valence levels

Valence levels are occupied by electrons of low binding energy (0-20 eV) from bonding orbitals. In this spectrum region the distance between different energy levels decreases so that they appear as a band structure. However, **k**-resolved Photoemission Spectroscopy (PES) is not subject to this work.

5.4.5 Surface Photovoltage Effect

During photoemission spectroscopy in particular with a synchrotron source, the high photon fluxes falling on semiconductors surfaces can affect the measured binding energy positions. Photons with an energy higher than the band gap of the semiconductor can induce electron-hole pairs which produce an "open circuit" voltage. This voltage is opposed to the built-in field created by the band bending from carrier depletion in the surface region [77, 78, 79]. Thus, the available band bending is reduced and the measured binding energies of core and valence levels are analogously shifted. In the example of upward band bending of Fig. 5.7 the generated electron-hole pairs are separated by the built-in field. Thus, the electrons are driven in the bulk whereas the holes are trapped near the surface. They compensate the space charge so that the band bending is reduced and lower binding energies are measured for all levels.

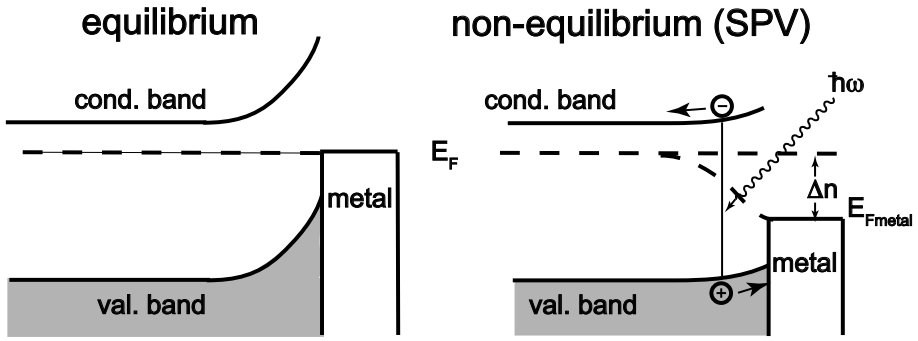

Figure 5.7: Surface Photovoltage Effect for the case of upward band bending. The electron-hole pairs generated by the high photon flux decrease the available band bending, as well as the core level shifts by Δn [78].

5.4.6 Numerical analysis

For the numerical analysis of the obtained SXPS spectra the programm IGOR was used, implementing an algorithm given by J. Humlicek [80] and discussed by F. Schreier [81], B.H. Armstrong [82] and E.E. Whiting [83]. The line shape of the core levels is fitted with a Voigt function, describing the form of the spin-orbit split doublets. The Voigt function is given as a convolution of a Lorentzian and Gaussian function. The background of the inelastically scattered electrons is fitted with a polynomial of third order accounting for the inelastically scattered electrons. During the fitting procedure a core level is fitted with multiple components by trying to obtain a residuum below the noise level of the spectra and a minimum number of components. The fitting parameters are given in table 5.1.

	$CuGaSe_2$		$CuInSe_2$		
core level	Se3d	Ga3d	Se3d	In4d	Cu2p
Spin-orbit splitting	0.85	0.44	0.85	0.85	
Branching ratio	1.64	1.66	1.62-1.50	1.59-1.51	
Gaussian width			0.64	0.47	0.74
Lorentzian width			0.05-0.06	0.11	0.36

Table 5.1: Fitting parameters for the Cu2p, Se3d, Ga3d and In4d core level spectra of $CuGaSe_2$ and $CuInSe_2$

6 Surface Preparation

In order to investigate the atomic surface structure clean, well-defined surfaces are indispensable. For the preparation of compound semiconductor surfaces under UHV conditions in general a variety of effective methods exists. However, many difficulties have been encountered until now in the preparation of chalcopyrite surfaces and especially of the (001) surface. As a result the knowledge about the properties of the (001) surface is very limited.

The cleaving surface for chalcopyrites is the (112) and (011) [84], while the (001) surface is expected to form (112) and ($\overline{112}$) facets, like the (110) surface [53], [86]. The (001) face of $CuInS_2$ layers grown on Si-substrates with MBE was investigated immediately after growth and was reported to be unreconstructed with partial facet building, according to the observed LEED pattern [53]. Capping with a Se layer proved recently to be an effective method of preparing clean (001) chalcopyrite surfaces [85], however, no reconstruction was observed with LEED at this first stage. More investigations of layers grown under different conditions and with different compositions are nescessary and are expected to provide further information about this surface. Therefore the preparation with decapping was implemented for the $CuInSe_2$ layers also in this work as well. Sputtering and annealing is an alternative possibility of preparing chalcopyrite surfaces. The study and optimization of this preparation procedure for both the $CuInSe_2$ and $CuGaSe_2$ was a main subject of this work.

6.1 Decapping

Decapping is widely applied in the recent years for the preparation of semiconductor compounds (e.g. [87] for GaAs, [88] for ZnSe). For this purpose the samples are capped with a removable protection layer directly after growth. Then they can be transported through air without being contaminated. After transfer of the samples to UHV for characterization, the protective layer is removed again by thermal desorption resulting from annealing at an appropriate temperature. In the case of $CuInSe_2$, Se is used as a protecting film, which can be removed by thermal annealing at 300 °C. Details of the capping and decapping process are found in ref. [85].

6.2 Sputtering

Sputtering and annealing is a standard method for the preparation of clean surfaces of crystals and particularly semiconductors (e.g. [89]-[92] for GaAs). During sputtering the surface is bombarded with energetic particles. The kinetic energy of the incident particles has to be higher than the binding energy of the target particles so that the latter are ejected from the surface. Therefore their threshold energy amounts to 20-40 eV for normal incidence. Mostly ions are used which do not react chemically with the atoms of the solid. By an Ar^+ ion beam of 500eV a yield of approximately 1 atom per ion can be reached.

The erosion in sputtering is measured by the sputtering yield which is defined as the average number of atoms removed from the surface per incident particle [93], [94]. The sputtering yield depends on the energy of the incident particles, their mass, their angle of incidence, as well as on the properties of the bombarded surface. However, the interaction of the incident particles with the surface not only removes the upper layers, but also leads to surface modifications which are not always desirable. Such changes can be structural, topographical, electronic or compositional [95].

During structural changes crystalline phases can be converted into amorphous ones and vice versa especially during bombardment with heavy ions. Topographical changes

include such effects like the formation of facets, steps, cones, the reorientation of crystallites etc on the surface. Faceting arises from the anisotropy of surface energy in crystals. Also the presence of defects, impurities or micro-inclusions in surface layers can be correlated with topographical changes. If the defects are sufficiently mobile (e.g. by the appropriate temperature) they tend to diffuse and form islands on the surface. Compositional changes are due to preferential effects. In binary alloys for example the component with the lower binding energy or larger size is removed at a larger rate. As a result the surface layer is enriched in the other component and the surface stoichiometry deviates the bulk stoichiometry. Diffusion plays a role also for this case: At low temperatures diffusion is suppressed and the atoms can be removed stoichiometrically, while at higher temperatures depletion is enhanced.

Besides, the selection of an appropriate annealing temperature can remove lattice damage induced by sputtering. For example implanted atoms of the incident beam are evaporated by annealing. In case bulk impurites are present on the surface several subsequent sputtering and annealing cycles are repeated until they are removed [96]. Hence, the choice of the appropriate parameters for sputtering is important in order to obtain a satisfying surface quality.

6.3 Cu-III-VI Surface Preparation

6.3.1 $CuGaSe_2$ Surface Preparation with sputtering

Considering chalcopyrites only $CuInSe_2$ (112) and (110) surfaces of single crystals [97], [65], [63], [98] and polycrystalline $CuInSe_2$ [99], $CuInS_2$ [100], and $Cu(In_{1-x}Ga_x)Se_2$ [101] prepared by sputtering and annealing are reported. Sputtering/annealing processing has not been applied to $Cu-III-VI_2$ chalcopyrite (001) surfaces. Besides it is mostly reported that variation of the energy to higher energies produces metallic preticipates: According to Corvini et al. [97] sputtering $CuInSe_2$ (112) surfaces with $E > 500eV$ at normal incidence led to Cu-depletion. Massopust et al. [65] report Se-depletion when sputtering with $E > 700eV$ at normal incidence. Metallic In is generated during the

preparation of $Cu(In_{1-x}Ga_x)Se_2$ with 1keV [101] whereas in the case of the $CuGaSe_2$ solar cell cross section, generation of metallic Ga is reported [102].

As it has been possible to prepare III-V surfaces successfully with Ar^+ ion-bombardment, the method was tried out for the $Cu-III-VI_2$ chalcopyrite (001) surface and studied as a function of Ar^+ ion energy, time and temperature. The cleanliness and structure of the samples surface was monitored with LEED and AES before and after each preparation step.

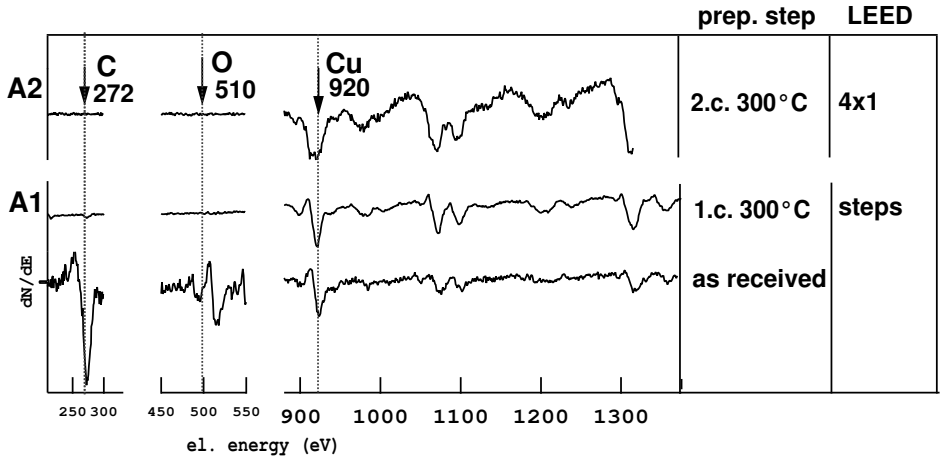

Figure 6.1: AES spectra of two samples from the same wafer A. All AES spectra are normalized to the Cu-peak at 920 eV and displayed on the same intensity scale. Spectra of sample A1 are shown before preparation and after the 1. sputtering cycle, spectra of sample A2 after the 2. cycle. Before preparation the C and O peak at 272 and 510 eV, respectively, have the highest intensity. After preparation the samples are free of contaminants.

The $CuGaSe_2$ samples were grown at the Hahn-Meitner Institute in the group of S. Siebentritt by Metal Organic Chemical Vapor Deposition (MOCVD) on a (001) oriented GaAs substrate under Cu-rich conditons. The parameters used for the growth process were a susceptor temperature of 570 °C, a total flow of 5 l/min, a reactor pressure of 50 mbar, H_2 as gas carrier and the metal organic compound was Cp Cu tBuCN (cyclopentadienyl Cu tertiary butyl isocyanide), TEGa (triethyl gallium), DTBSe (ditertiary butyl

selenide). In the Cu-rich composition regime a phase coexistence of $CuGaSe_2$ and Cu_xSe has been observed. From PL (photoluminescence) measurements it is possible to assess the Cu-excess during growth of different samples quite accurately [103]. Through KCN etching the Cu_xSe-film is removed from the surface so that the samples have an almost stoichiometric ratio of Cu/Ga. For these preliminary experiments samples (A) grown under moderate Cu-excess of Cu/Ga $\approx$ 1.05 were used, according to PL data. For the further surface analytical experiments described in chapter 7 also samples (B) grown with a low Cu-excess of $1 \leq$ Cu/Ga < 1.05 and samples (C) grown with a high Cu-excess were taken.

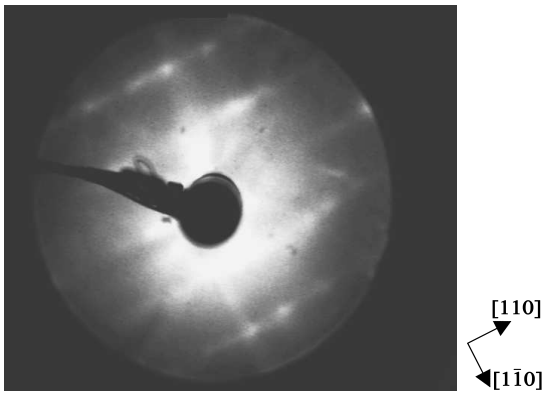

Figure 6.2: LEED pattern of the $CuGaSe_2$ (001)surface, taken at a primary electron energy of 136 eV. The streaks proceed in [110] direction and imply a stepped surface.

According to the results from the literature mentioned on the above, an energy of 600eV of the Ar^+ ions at normal incidence in an Ar^+ background pressure of 2×10^{-6} mbar was chosen in order to avoid metallic Ga/In generation. XPS results given in section 8.3.5 from samples sputtered with different Ar^+ ion energies confirm that this is in fact the optimal Ar^+ ion energy for these experiments. A clean surface free of contaminants could already be obtained after approximately 1h of sputtering and subsequent annealing at 300 °C to restore the surface damage. However, the quality of the surface at this stage was still such that only a very faint (1×1) LEED-pattern could be observed. In a next attempt simultaneous sputtering and annealing at 300 °C was applied which improved the surface quality, as it has been already reported for the preparation of GaAs

surfaces [104, 105]. A change in the LEED pattern could be observed after three hours of sputtering and simultaneous annealing at 300 °C. Further annealing for another 3h slightly improved the LEED pattern. From the AES spectra taken after this preparation cycle it can be easily discerned that the oxygen was completely removed from the surface (Fig.6.1). The residual C-and O-concentration is negligible. The LEED pattern observed at higher primary electron energies shows streaks along the $[1\bar{1}0]$ direction, implying a stepped surface (Fig.6.2).

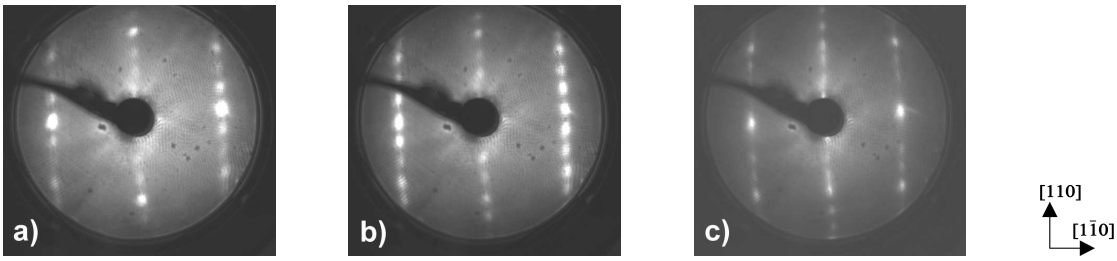

Figure 6.3: LEED patterns of the $CuGaSe_2$ (001)surface of sample (I), taken at a primary electron energy of a) 39, b) 41 and c) 51 eV respectively. The pattern symmetry corresponds to (4×1).

After a second sputtering cycle with the same parameters as the first one a change of the surface structure could be observed. The steps apparently vanished from the surface and a clear LEED-pattern with sharp spots appeared (Fig. 6.3), exhibiting a reconstruction of the surface with a (4×1) symmetry. AES spectra at this stage confirm the absence of C and O contaminations (Fig. 6.1). Raising the annealing temperature up to 450 °C in steps of 50 °C did not induce a respective change in the LEED pattern. AES spectra of Cu, Ga, and Se after each preparation step are shown in Fig.6.4.

Table 6.1: Preparation steps for the optimized preparation by Ar^+ ion sputtering and annealing on the $CuGaSe_2$ (001) surface (sample A) with corresponding LEED pattern.

preparation	LEED pattern
3h sputt./anneal 300 °C	
3h anneal 300 °C	steps
3h sputt./anneal 300 °C	
3h anneal 300 °C	(4×1)

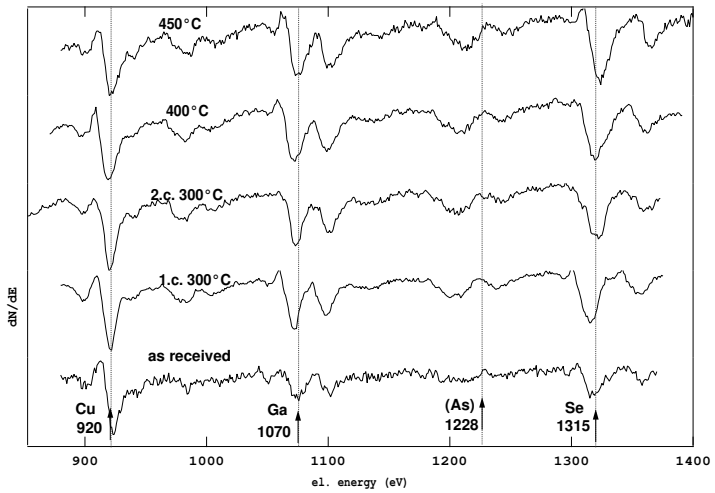

Figure 6.4: AES spectra of $CuGaSe_2$/GaAs(001) (sample A1) for different preparation steps. The spectra are normalized to the Cu-peak. The Cu, Ga and Se peaks at 920, 1070 and 1315 eV respectively are well discerned. There is no evidence of As (1228 eV) on any of the spectra. The peak at approximately 1210 eV is a sideband of the Se-peak.

Further preparation of the sample with the same parameters first deteriorated slightly the surface structure but then reproduced the same results. Also different durations for the subsequent sputtering and annealing cycles were tried out. However, the scheme described on the above proved to be the simplest one in order to optimize the surface structure, consisting of two preparation cycles of 3h simultaneous sputtering and annealing and 3h subsequent annealing at 300 °C each, as also described in table 6.1.

6.3.2 $CuInSe_2$ Surface Preparation with decapping and sputtering

For the preparation of the $CuInSe_2$ surface both preparation methods, decapping and sputtering, were used. The preparation, as well as the properties of the $CuInSe_2$ (001) surface are discussed in chapter 8.

7 The $CuGaSe_2$ (001) surface

The development of a preparation procedure leading to a clean, well-ordered $CuGaSe_2$ (001) surface enables the investigation of its structural and electronic properties. Thus, the stoichiometry, symmetry and periodicity of the $CuGaSe_2$ (001) surface will be discussed with respect to composition, as well as the surface morphology. In order to detect the chemical state of the surface atoms participating in the (4×1) reconstruction, the results obtained by SXPS are analyzed. In addition an insight of the different phases present on the oxidized $CuGaSe_2$ surface is provided.

7.1 Surface stoichiometry

Information about the stoichiometry of the different elements present on the $CuGaSe_2$ surface was derived from the evaluation of the AES spectra of sample A1 from Fig.6.4. For this purpose the percentage relative surface concentration of the different elements was calculated according to [68]. Before preparation the percentage relative surface concentration amounts to approximately 0.3/0.2/0.5 for Cu/Ga/Se respectively. After the first sputtering cycle the ratio changes to 0.2/0.25/0.55, which implies some Cu-depletion. Further annealing to higher temperatures does not change the ratio. Only after heating to 450 °C a further Cu-depletion and Se-enrichment is observed , so that the Cu/Ga/Se ratio changes to 0.15/0.2/0.65, as can be also seen in Fig.7.1. As far as C and O contamination is concerned, the percentage relative concentration of C and O was calculated to be below 0.018 and 0.005, respectively, after preparation, by considering the noise amplitude of the respective AES spectra of samples A1 and A2 in Fig. 6.1.

A slight Cu-depletion by sputtering is in line with other related work. As already

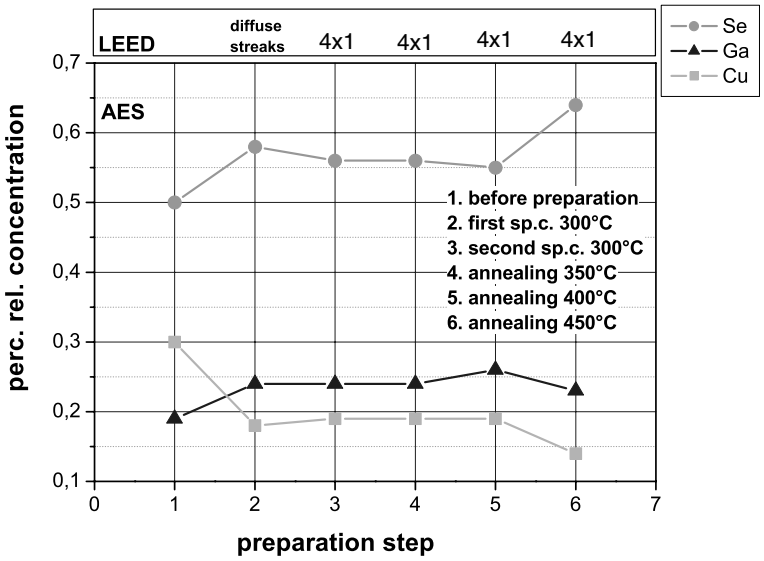

Figure 7.1: Percentage relative surface concentration of Cu, Ga and Se after each preparation step. After the second preparation cycle a slight decrease in the relative Cu-concentration is detected. After the second preparation cycle with sputtering and annealing at 300 °C and after annealing to 400 °C no change in stoichiometry is observed. After annealing at 450 °C some Cu-depletion takes place again.

mentioned, Corvini et al. [97] report Cu-depletion when sputtering the $CuInSe_2$ (112) surface with $E > 500eV$ at normal incidence, which was detected by AES. Liao et al. [61] observe Cu-depletion on $CuInSe_2$ (112) surfaces by x-ray photoelectron spectroscopy in the top 1-2 atomic layers. Also elsewhere [106, 57] Cu-poor surface layers are reported. The untreated surface is Cu-rich due to the remaining Cu_xSe after etching. This remaining Cu_xSe is sputtered away and should lead to Cu-depletion. However, the surface remains Se-rich after the second preparation cycle. Therefore it is supposed that the stoichiometry change measured with Auger is not only related to the removal of Cu_xSe, but additionally associated with the change of the surface structure through sputtering, as it will be further discussed in section 7.4. The origin of AES intensity changes after heating the sample at 450 °C may be related to Cu-diffusion into the bulk. Similar annealing effects have been reported by [107, 108]. Furthermore it should be emphasized that no As is detected on the surface. The corresponding As-peak should appear at

1228 eV, but only the side-bands of the Se-peaks at 1098 and 1205 eV are present.

Summarizing, the prepared $CuGaSe_2$ surface is free of C and O contaminants. Some Cu-depletion is observed during the transition from the oxidized to the prepared surface which is attributed to the removal of Cu_xSe, as well as to the change of the surface structure with sputtering. Annealing up to 400 °C does not modify the surface stoichiometry. Only after annealing at 450 °C, further Cu-depletion is observed probably induced by Cu-diffusion into the bulk. No As could be detected on the surface.

7.2 Surface symmetry and structure

In order to assign the observed LEED-pattern of a (4×1) reconstruction on the $CuGaSe_2$ surface (Fig. 6.3), it is necessary to take into consideration the chalcopyrite structure. The chalcopyrite unit cell has twice the size of the zinc blende cell in c-direction [**?**]. Since c is along the [001] direction, the (001) ideal surface has a quadratic unit mesh. As already discussed in section 4.4, two distinct ideal (001) surfaces exist, consisting either of alternating rows of Cu and Ga atoms or of Se atoms. The observed reconstruction refers to $4\times\frac{a_o}{\sqrt{2}}$ along the $[1\bar{1}0]$ direction and $\frac{a_o}{\sqrt{2}}$ along the [110] direction, with $\frac{a_o}{\sqrt{2}} = 3.95$ Å.

Furthermore the dependence of the surface structure on the exact amount of Cu excess during growth was investigated. The same preparation procedure described in chapter 6 was also applied to $CuGaSe_2$ samples grown with a low Cu-excess (B) and with a high Cu-excess (C). According to the AES spectra, the surfaces of all samples were free of C and O contaminants after sputtering and annealing. Although exactly the same preparation procedure was followed the obtained LEED patterns displayed clear differences. The (4×1) reconstruction observed on sample A was not complete for samples C, as the spots corresponding to the reconstruction had a much weaker intensity. For samples B, the spots corresponding to the reconstruction were well visible, however, they were much longer along the $[1\bar{1}0]$ direction (Fig.7.2). After increasing the energy of the electron beam over 100 eV, streaks with long spots were still visible. Accordingly the surface of these samples had more pronounced steps than sample A which did not recede

completely by sputtering. Besides also the percentage relative surface concentration of Cu calculated from the corresponding AES spectra was lower on the surface of sample B in comparison to sample A.

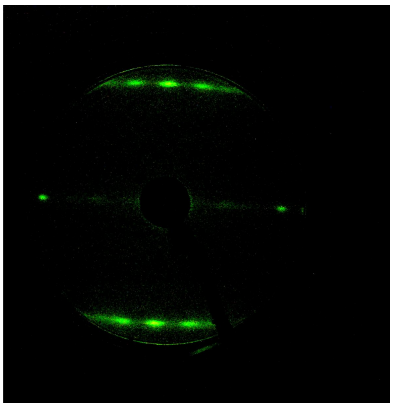

Figure 7.2: Leed-pattern of a sample (B) grown under low Cu-excess showing a (4×1) reconstruction with steps.

Summarizing, the prepared $CuGaSe_2$ samples (A) grown with a moderate Cu-excess exhibit a clear (4×1) reconstruction. Samples (B) grown with a lower Cu-excess show a (4×1) reconstruction with steps which can not removed by sputtering. The relative Cu concentration of the surface of samples B is lower as well in comparison to samples A. In contrast, samples C grown under high Cu-excess show only a weak, uncomplete (4×1) reconstruction but they are flat.

7.3 Surface morphology

AFM measurements were undertaken before preparation (Fig.7.3a), after the first (Fig.7.3b) and after the second preparation cycle (Fig.7.3c) in order to gain information contributing in the interpretation of the obtained LEED patterns. Characteristic for all the AFM pictures are the grooves proceeding along the [110] direction of 10-20 nm depth which arise from the epitaxial growth. Line scans perpendicular to the groove direction are shown on the right side of Fig.7.3. In addition to the large amplitude grooves, smaller irregularities in the order of 1-4 nm can be discerned on the height profiles before and after the first preparation cycle. However, after the second preparation cycle these smaller height differences disappear and rather regular grooves of 10-20 nm depth with a smooth

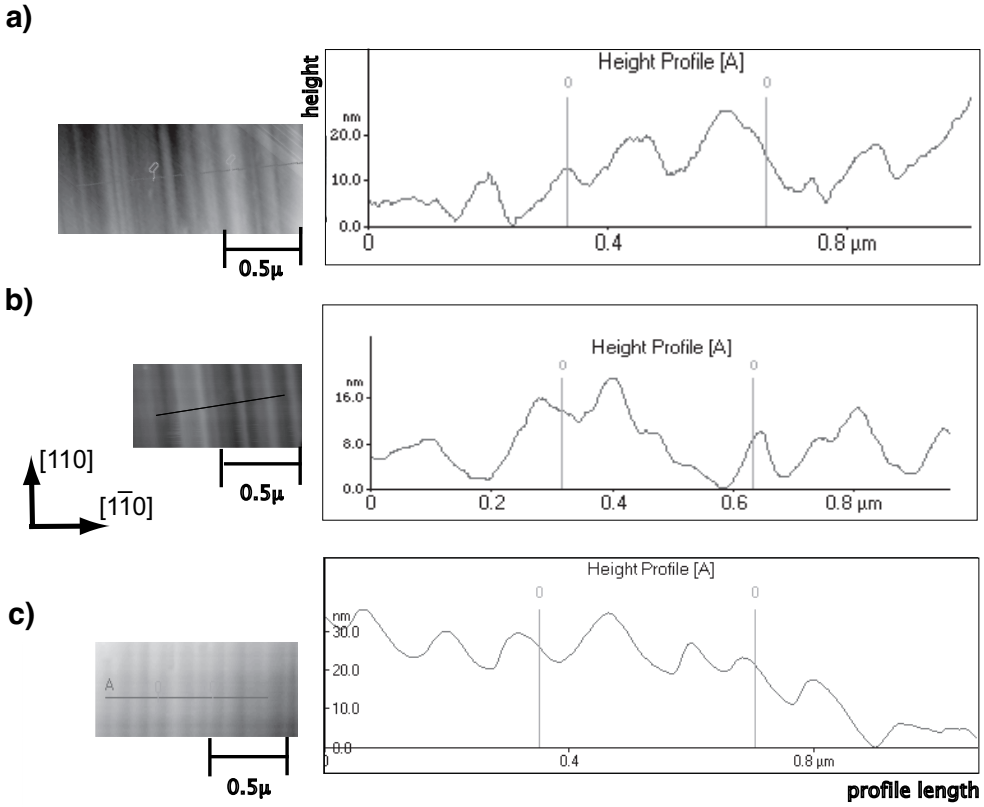

Figure 7.3: AFM pictures and corresponding height profile of sample (I) a) before preparation, b) after the first sputtering cycle, c) after the second sputtering cycle.

surface remain. Therefore it is ascertained that the steps observed with LEED are related to the height differences of 1-4 nm rather than the grooves with a height modulation of 10-20 nm. Besides the larger grooves can't influence the shape of the LEED spots as they are larger than the coherence length of the electron gun focus.

7.4 Chemical characterization

So as to acquire information about the surface phases and the chemical state of the (4×1) reconstruction on the $CuGaSe_2$ surface, the SXPS spectra obtained from measurements performed on sample B will be analyzed. For this sample a (4×1) reconstruction was observed with LEED with remaining steps on the surface as shown in section 7.2. The

preparation steps are given in table 7.1.

Table 7.1: Preparation steps for the $CuGaSe_2$ (001) surface of sample B measured with SXPS

preparation	prep. step
as received	A
0.5h sputt./anneal	B
0.5h sputt./anneal	C
2h sputt./anneal,	D
3h anneal (300)°C	
2.5h sputt./anneal,	E
2.5h anneal (300)°C	

7.4.1 Survey spectra

The XPS spectra of the core levels Se3d and Ga3d, as well as the valence band (dominating Cu3d) after each preparation step are shown in Fig. 7.4a), b) for an excitation energy of 95eV. In Fig. 7.4c), d) also the C1s and O1s spectra for an excitation energy of 650eV are shown. The preparation steps are listed in detail in table 7.1. Line shape changes in the Ga3d and Se3d emissions are observed as the surface is cleaned by sputtering. The intensity changes of the Se3d and Ga3d core levels and the prominent Cu3d emission in the valence band at ~ 3.5eV of sample B (Fig. 7.4) are generally in line with the compositional changes monitored by AES for sample A in section 7.1. The increase in Se3d emission intensity upon the first preparation step is much more pronounced, which is due to the high surface sensitivity of the XPS experiment, where the kinetic energy of 41 eV of the Se3d photoelectrons excited with $h\nu = 95$eV relates to an escape depth λ of only ~ 0.6nm.

The Se3d and Ga3d emissions of the non-treated surface clearly exhibit contributions of several components which should derive from surface phases and oxides. The disappearance of these surface components during the first sputter/annealing cycles B and C and the strong decrease of the O1s emission indicate the removal of these surface phases. After preparation step C, a weak shoulder develops at the low binding energy side of the

Se3d emission, which becomes more pronounced with the following preparation steps D and E. After preparation E, the additional component at the low binding energy of the Se3d emission side is readily discernible. Some residual traces of C, CO and O_x are still detected, which could result from the change of the pressure from 10^{-10} mbar to 10^{-9} mbar during the last preparation cycles. In order to exactly identify the observed surface components, the Se3d and Ga3d core levels were deconvoluted by curve fitting.

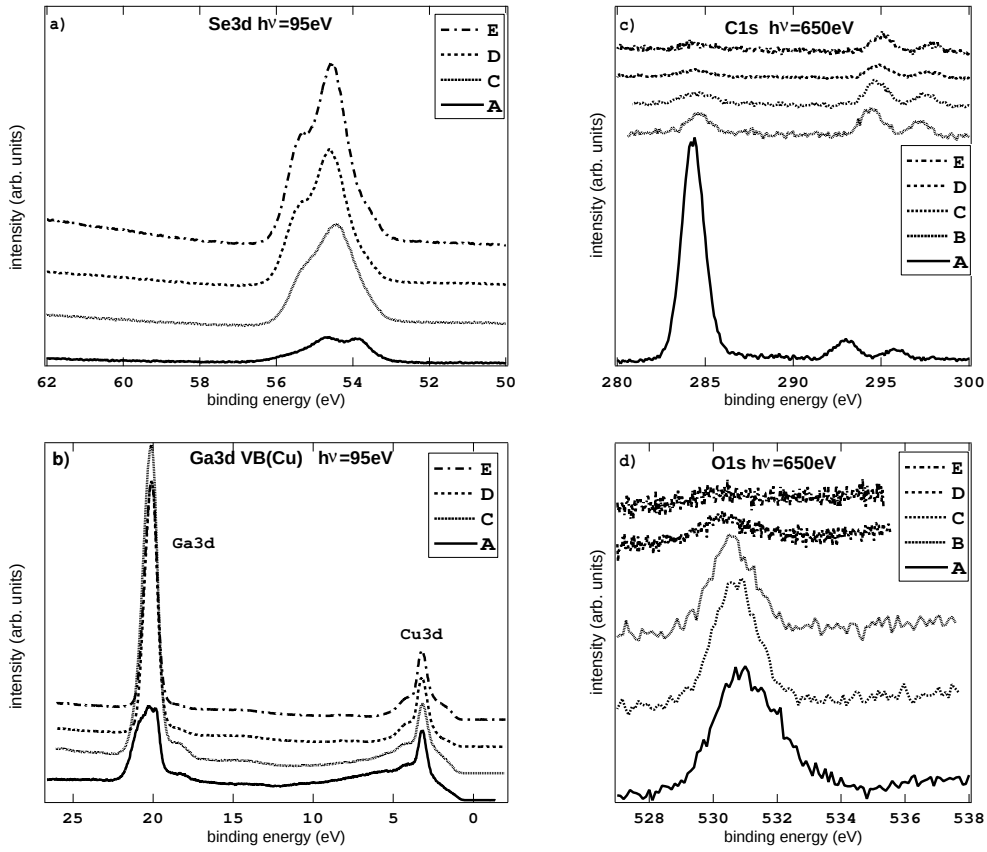

Figure 7.4: Core level spectra excited by 95eV of a) Se3d, b) Ga3d and the valence band, which is dominated by Cu3d, and core level spectra excited by 650eV of c) C1s, d) O1s. Spectra in b) were normalized on the intensity of the Cu3d peak. The spectra were taken after preparation step A-E, as listed in table 7.1

7.4.2 The oxidized $CuGaSe_2$ surface

A deconvolution of the Se3d level (Fig. 7.5) reveals two surface components with a binding energy shift of +0.7 and +1.15 eV with respect to the bulk component. The surface components fitted in the Ga3d level are shifted by +0.8 and +0.35 eV, as well as by -0.5 and -1.6 eV. These additional components in the Se3d level, as well as the Ga3d surface components are removed by the sputter/annealing cycles B and C.

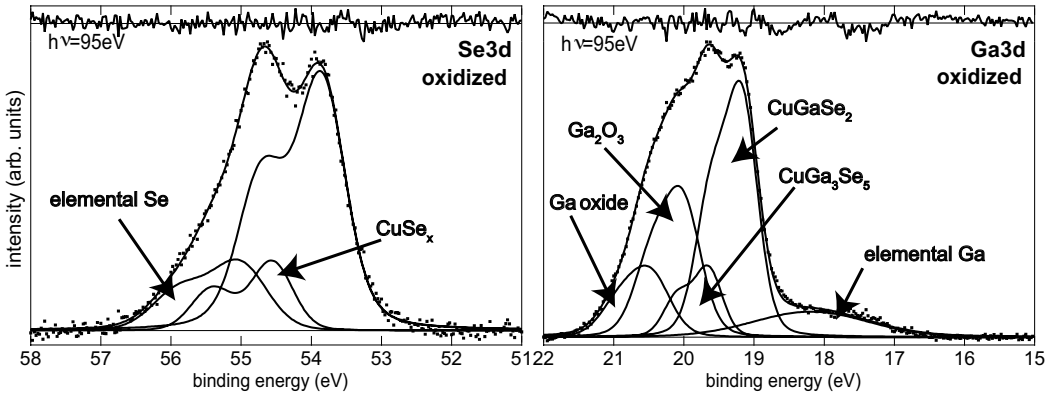

Figure 7.5: Fitted Se3d and Ga3d core-level spectra excited by 95 eV of the oxidized $CuGaSe_2$ (001) surface (sample B) before preparation. The surface components are marked with arrows.

In their study on the oxidation of $CuInSe_2$ surfaces, Kazmerski et al. [109] had observed the formation of In_2O_3 and Cu_2Se. The Cu_2Se component was shifted by +0.7 eV with respect to the bulk emission. Würz et al. [110] also report of a Cu_2Se component shifted by +0.4 eV in the Se3d core level of thermally oxidized $CuGaSe_2$. Consequently, the +0.7 eV surface component in Se3d can be identified with Cu_2Se. The remaining surface components should be also correlated with the surface phases of the $CuGaSe_2$ epilayer which was etched with KCN and exposed to air. As it will be later shown in chapter 8, Fig. 8.6, elemental Se is shifted by about 1 eV towards the bulk Se peak of the $CuInSe_2$ surface. Therefore the surface component of the Se3d emission shifted by +1.15 eV is supposed to correspond to elemental Se as well.

The surface component of the Ga3d peak shifted by -1.15 eV can be attributed to

metallic Ga. Namely the Ga3d spectra of the oxidized surface were compared with other spectra of $CuGaSe_2$ sputtered with high ion energies where metallic Ga was generated (Fig 7.6a). The component shifted by -1.15 eV coincides with the pronounced metallic Ga peak of the second sample (E_B =18.3 eV). A similar component at the same BE has been also observed on polycrystalline $CuGaSe_2$ samples [111]. Hence, small amounts of metallic Ga are present on the surface.

The component at a BE of 19.17 eV has the highest intensity. By comparing the energy differences between the Se3d and Ga3d spectra from the oxidized and from the sputtered surface, this component is explicitly attributed to the $CuGaSe_2$ bulk component. The comparison of the spectra in Fig. 7.6a) corroborates this argument, as this component coincides with the distinct $CuGaSe_2$ peak of the sample sputtered with higher energies.

Würz et al. [110] also observe a Ga_2O_3 surface component with a BE shift of + 0.7 eV towards the Ga3d bulk component of the oxidized $CuGaSe_2$. Bertness et al. [112] identify in the Ga3d spectra of oxidized GaAs a peak shift at +0.9 eV with Ga bound directly to oxygen. During the room temperature and thermal oxidation of GaSe [113] a surface component at a BE of 20.1 eV and 20.5 eV respectively in the Ga3d core level was attributed to Ga_2O_3. Therefore the component shifted by +0.85 eV (E_B =20 eV) in the Ga3d spectra of the oxidized $CuGaSe_2$ in Fig. 7.5 is attributed to Ga_2O_3, as well. The component shifted by +1.3 eV (E_B =20.4 eV) is accordingly attributed to a further Ga_2O_3. Moreover Iwakuro et al. [113] report the formation of Ga hydroxides on the GaAs surface, like $Ga(OH)_3$. However, in the O 1s spectra of the oxidized $CuGaSe_2$ surface no OH^- components can be discerned near the dominating O^{2-} component (Fig. 7.6b). Consequently the presence of Ga hydroxides on the oxidized $CuGaSe_2$ surface is exluded.

The surface component at a BE of 19.65 eV has the lowest intensity. Iwakuro et al. [113] measured the BE of sputtered GaSe at 19.5 eV and of oxidized GaSe at 19.3 eV. Thus, this surface component could be related with a surface phase such as GaSe or Ga_2Se_3. The formation of Ga_2Se_3, $CuGa_3Se_5$ or $CuGa_5Se_8$ on $CuGaSe_2$ surfaces is possible according to phase diagrams for Ga-rich conditions (see section 4.5). Schmid et

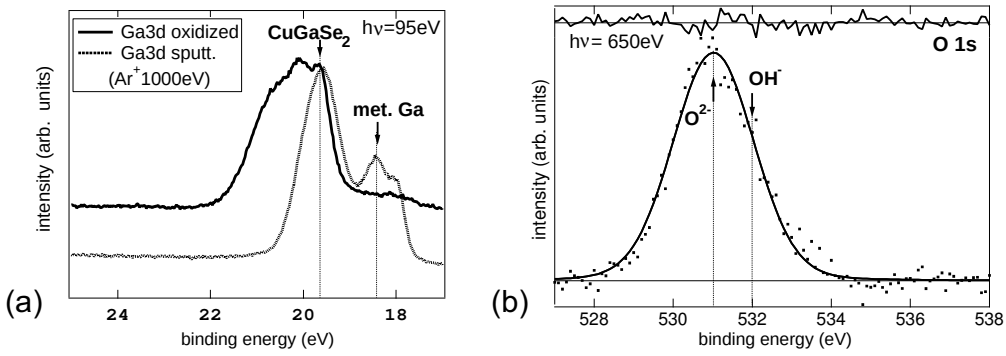

Figure 7.6: a) Ga3d spectra excited with 95eV of the oxidized sample (B) before preparation and of a sample (A) sputtered with an Ar^+ ion energy of 1000eV resulting in the generation of metallic Ga. b) fitted O1s spectra excited with 650 eV of the oxidized surface (B). Only one peak at 531 eV is present, corresponding to O^{2-}. The O oxidation state of OH^- at 532 eV does not appear.

al. [57] detected a $CuGa_5Se_8$ phase on Cu-poor polycrystalline $CuGaSe_2$ with valence band spectroscopy. Würz et al. [110] report the presence of $CuGa_3Se_5$ on polycrystalline $CuGaSe_2$ films, however, no corresponding surface components are explicitly shown in the measured Se3d and Ga3d core levels. In order to clarify the origin of this surface component, XPS spectra taken from decapped $CuGa_3Se_5$ films [114] were compared with the spectra of the oxidized $CuGaSe_2$ sample in Fig. 7.7. The spectra were calibrated relative to the Se3d peaks. Namely on the Se3d core level of the oxidized $CuGaSe_2$ no further surface components apart from the Se oxide components appear, which could be associated with a $CuGa_3Se_5$ phase. Thus, in case of the presence of a $CuGa_3Se_5$ phase on the $CuGaSe_2$ surface, the Se3d levels of both should appear at the same binding energy. Hence, by comparison of the Ga3d levels after calibration, the Ga3d peak of the $CuGa_3Se_5$ sample coincides with the unidentified surface component of the oxidized $CuGaSe_2$. Thus, the surface component at a BE of 19.17 eV is attributed to the surface phase $CuGa_3Se_5$.

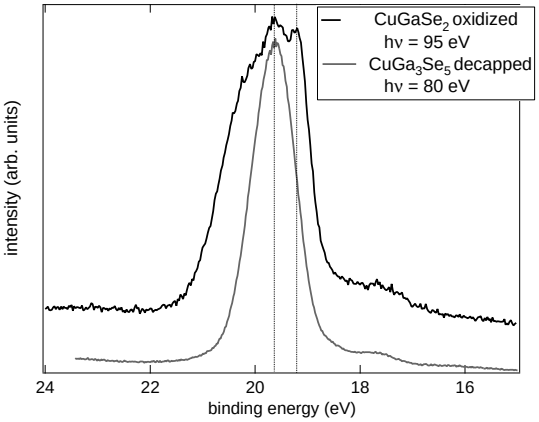

Figure 7.7: Ga3d spectra of the oxidized $CuGaSe_2$ sample before preparation excited with 95eV and of a decapped $CuGa_3Se_5$ sample excited with 80 eV.

7.4.3 The sputtered $CuGaSe_2$ surface

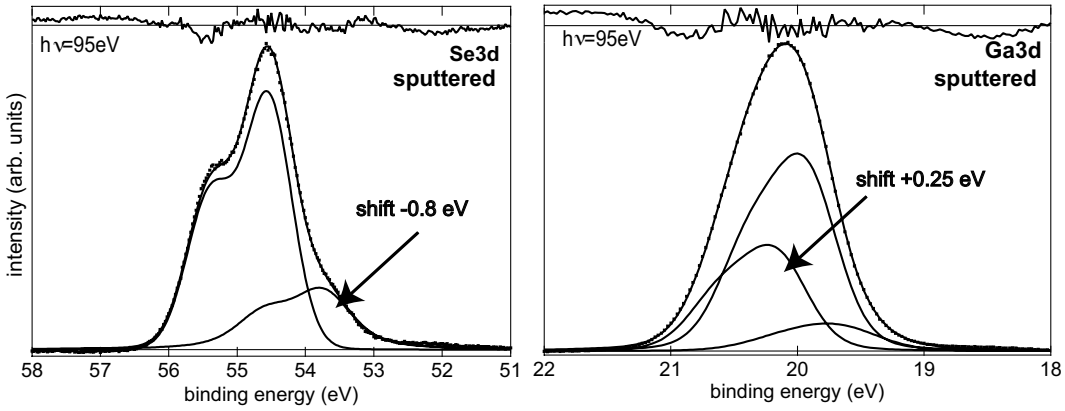

Figure 7.8: Fitted Se3d and Ga3d core-level spectra of the $CuGaSe_2$ (001) surface (sample B) after preparation showing a stepped (4×1) reconstruction

The Se3d level of the clean $CuGaSe_2$ surface is deconvoluted into a bulk and an additional component with a shift of -0.8 eV with respect to the bulk emission (Fig. 7.8). The intensity of this component decreases with higher excitation energy ($h\nu = 230$eV) which proves it to be a surface component. A similar surface component with a surface core level shift of –0.60 eV had been reported earlier for epitaxial $CuInSe_2$/GaAs (100), but was not correlated with LEED data [115]. For ZnSe (001), a surface core level shift of –0.32 eV had been observed for both the Se-rich (2x1) and the Zn-rich c(2x2)

reconstructions. By comparison to these literature data, the surface component can be attributed to the selenium atoms of the well-defined (4×1) reconstructed $CuGaSe_2$ (001) surface. In the Ga3d peak it also possible to fit two components. The component shifted by +0.3 eV can be related to a surface contribution of Ga adatoms, whereas the component shifted by -0.3 eV could be related with bulk defects generated during the preparation process, as it will be further discussed for the case of the $CuInSe_2$ (001) surface in chapter 8.

Table 7.2: BE shifts of the surface components with respect to the bulk component that were detected in the Se3d and Ga3d core level spectra of $CuGaSe_2$

	Se3d	Ga3d
BE shift	-0.8	+0.3
BE shift surface phases		
Cu_2Se	+0.7 eV	
elemental Se	+1.15 eV	
Ga_2O_3		+0.85
Ga oxide		+1.3
$CuGa_3Se_5$		+0.5
elemental Ga		-1.15

7.4.4 Summary

On the oxidized $CuGaSe_2$ surface, phases and oxides such as Cu_2Se and Ga_2O_3, as well as a second Ga oxide were detected. Also elemental Se and Ga were found. Especially the presence of $CuGa_3Se_5$ could be identified. The clean surface exhibits a Se3d surface component correlated with the surface reconstruction observed with LEED, and probably also a Ga3d surface component. The measured BE shifts for the surface components are given in table 7.2.

7.5 Conclusions

The phases present on the oxidized $CuGaSe_2$ (001) surface of a sample (C) grown under low Cu-excess were identified. Besides elemental Se and elemental Ga, Ga oxides such as Ga_2O_3 were detected, as well as the expected Cu_xSe phase (section 4.5). A surface component with a shift of +0.5 eV towards the bulk component in the Ga3d core level was attributed to $CuGa_3Se_5$. Until now $CuGa_3Se_5$ had been reported only on polycrystalline $CuGaSe_2$ and $CuIn_3Se_5$ on polycrystalline $CuInSe_2$ (section 4.5), although no surface component in the core levels was attributed to this phase. Thus, according to these results the $CuGa_3Se_5$ phase can be found also on epitaxial $CuGaSe_2$ grown under low Cu-excess and a corresponding surface component is found in the Ga3d core level. Further SXPS investigations on samples with different stoichiometries are required in order to confirm this statement.

After applying the optimized preparation from chapter 6 by Ar^+ ion sputtering and annealing on samples (A) grown under moderate Cu-excess, surface phases and oxides are completely removed. Surfaces free of C, O and As contaminants are obtained exhibiting a clear (4×1) reconstruction. The observed reconstruction refers to $4 \times \frac{a_o}{\sqrt{2}}$ along the $[1\bar{1}0]$ direction and $\frac{a_o}{\sqrt{2}}$ along the [110] direction, with $\frac{a_o}{\sqrt{2}} = 3.95$ Å. A surface component with a BE shift of -0.8 eV is found in the Se3d core level of the clean surface. In Ga3d core level it is also possible to fit surface components. These surface components are related with the surface atoms participating in the (4×1) reconstruction.

A noteworthy dependence of the surface structure on the amount of Cu-excess under which samples are grown is observed. The (4×1) reconstruction of samples (C) grown under high Cu-excess is not complete, as the corresponding LEED spots are weaker. Samples (B) grown under low Cu-excess show a clear (4×1) reconstruction with intensive spots, however, steps remain also on the surface which cannot removed completely by sputtering as in the case of samples (A) and (C). Also the surface composition of sample (B) is Cu-poorer in comparison to the surface composition of sample (A). Additionally, all samples show some Cu-depletion during the transition from the oxidized to the clean surface. The surface of all samples feature grooves along the [110] direction of 10-20 nm

height. The steps observed on the LEED patterns are identified as smaller irregularities in the order of 1-4 nm which proceede along the grooves.

8 The $CuInSe_2$ (001) surface

Like in the case of the $CuGaSe_2$ (001) surface, the preparation and properties of the $CuInSe_2$ (001) surface will be presented. For the preparation of the $CuInSe_2$ (001) surface both decapping and sputtering methods are implemented. The surface stoichiometry and structure are investigated in respect to bulk composition. Surface components by slightly different surface structures of the $CuInSe_2$ (001) surface are identified with SXPS and correlated with the obtained LEED patterns. Subsequently a structure model for both the $CuGaSe_2$ and $CuInSe_2$ surface is proposed. Moreover, a similar correlation between surface composition, structure and bulk composition is found for both $CuGaSe_2$ and $CuInSe_2$.

8.1 Preparation

The $CuInSe_2$/GaAs (001) epilayers were grown by Molecular Beam Epitaxy (MBE) according to [116] and subsequently capped with a protective Se layer [53]. Constant fluxes from elemental sources were applied throughout the whole deposition process at a substrate temperature of T_{sub} of 450 °C. The growth duration was 60 min which resulted in an epilayer thickness of 0.7 μm. The CIS film was exposed to the selenium molecular beam at a T_{sub} below 130 °C in order to deposit an amorphous Se film. The Se cap layer protects the $CuInSe_2$ surface from contamination and oxidation during transport and storage in air [85]. For the surface analytical experiments samples with different stoichiometries were used, namely a Cu-poor and a stoichiometric sample. The [Cu]:[In] ratio of the Cu-poor sample was measured to 0.84 and of the stoichiometric sample to 0.98 by electron-probe microanalysis.

LEED	preparation	prep. step
faceted	decapping 150°C 15 min	
faceted	annealing 200°C 15 min	
faceted	annealing 250°C 15 min	
faceted	annealing 300°C 15 min	A
faceted	annealing 350°C 15 min	
faceted	annealing 400°C 15 min	
faceted	annealing 450°C 15 min	
faceted/(1x1)	3h sputter/anneal, 1h anneal (350)°C	B
(4x2)/(2x4)	3h sputter/anneal, 1h anneal (350)°C	C
(4x2)	3h sputter/anneal, 1h anneal (350)°C	D

Table 8.1: Preparation steps for the $CuInSe_2$ (001) surface with corresponding LEED pattern during the first set of experiments at the TU Berlin

Like in the case of $CuGaSe_2$, the preparation of the $CuInSe_2$ films was studied during the first set of experiments in the system of the TU Berlin, while the chemical characterization of the obtained surfaces was implemented at the BESSY synchrotron storage ring. During the first set only Cu-poor $CuInSe_2$ layers were used, while in the second set both Cu-poor and stoichiometric $CuInSe_2$ layers were studied. Whereas the oxidized $CuGaSe_2$ films were directly sputtered, the $CuInSe_2$ layers were first decapped after being introduced in the preparation chamber and subsequently sputtered. For the preparation study the surface structure and composition of the samples after each preparation cycle was monitored by LEED and AES. The protecting Se film was removed from the $CuInSe_2$ samples by annealing at 150°C leading to the desorption of the Se cap layer ("decapping") [85]. Further annealing cycles with increasing temperature were implemented. Subsequently, the preparation procedure by sputtering and annealing obtained for $CuGaSe_2$ was applied and optimized on the $CuInSe_2$ layers. The samples were sputtered by Ar^+ ion-bombardment with 600 eV Ar^+ ions at normal incidence with a background pressure of 2×10^{-6} mbar as well. The employed cycles for the whole prepa-

ration process are listed in Table 8.1. For the second set of experiments during which the characterization of the observed structures was in the foreground, the preparation process was abbreviated as listed in Table 8.2.

LEED	preparation	prep. step
faceted	decapping (300)°C	A
faceted	1h sputter/anneal,	B1
	30 min anneal (350)°C	
(4x2)/(2x4)	6h sputter/anneal,	C
	2h anneal (350)°C	
(4x2) not obtained		D
(4x2)/(2x4) with met. In	3h sputter/anneal (Ar^+ ion energy > 600eV),	E
	1h anneal (350)°C	

Table 8.2: Preparation steps for the $CuInSe_2$ (001) surface with corresponding LEED pattern during the second set of experiments at the BESSY synchrotron storage ring.

8.2 Surface symmetry and stoichiometry

The obtained LEED patterns for the Cu-poor $CuInSe_2$ sample during the first set of experiments are shown in Fig. 8.1. After decapping of the $CuInSe_2$ sample, the LEED pattern indicates a completely faceted surface (Fig. 8.1a). The LEED spots split and move outwards along the $[1\bar{1}0]$ and [110] direction with increasing electron energy, thus they correspond to {112} and $\{11\bar{2}\}$ facets [53]. The LEED pattern resembles that of MBE grown $CuInS_2$/Si(001) epilayers [53]. Annealing to higher temperatures increases the intensity of the LEED spots without modifying the LEED pattern itself. Thus, Se and C rests are removed from the surface, as it will be also shown by the AES spectra. After preparation step B by sputtering, also a (1×1) LEED pattern is obtained (Fig. 8.1b). By increasing electron energy besides the facet spots, the (1×1) is still visible, indicating the partial removal of the facets and the presence of (001) oriented areas on the surface. By further sputtering of the $CuInSe_2$ surface, the facets are completely

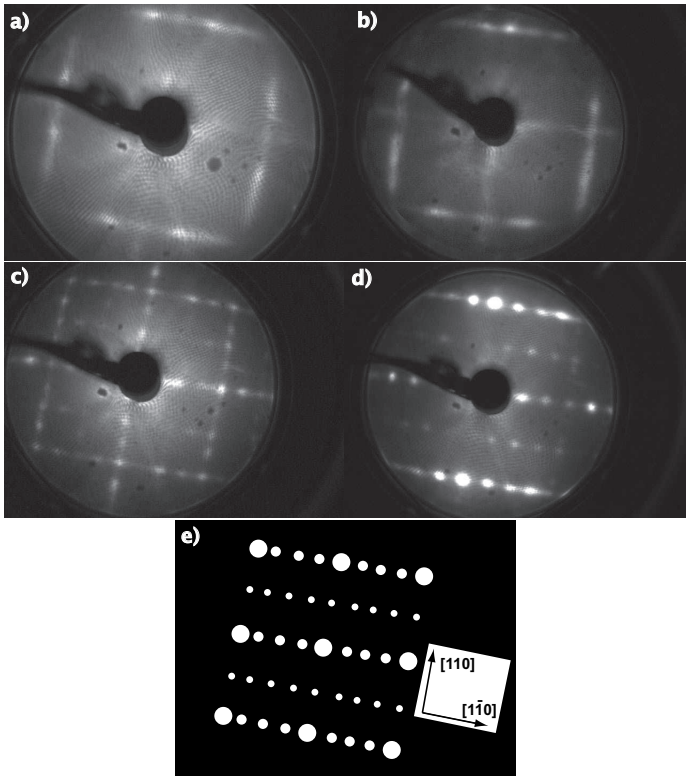

Figure 8.1: LEED patterns of the $CuInSe_2$ (001) surface of the Cu-poor sample a) after decapping taken at a primary electron energy of 41eV, b) after preparation step B at 41eV, c) after preparation step C at 45 eV, d) after preparation step D at 35 eV. The pattern symmetry in c) corresponds to a mixed $(4 \times 2)/(2 \times 4)$, whereas in d) to (4×2), which is illustrated schematically in e).

removed and a mixed $(4 \times 2)/(2 \times 4)$ structure appears (Fig. 8.1c). The possibility of a (4×4) superstructure is excluded, as the fractional order spots $\{\frac{1}{4}\frac{1}{4}\}$, $\{\frac{1}{4}\frac{3}{4}\}$, $\{\frac{3}{4}\frac{3}{4}\}$ are not observed. An other preparation cycle leads to the formation of a (4×2) reconstruction (Fig. 8.1d).

A series of selected AES spectra before preparation, after decappping at 150°C, annealing at 450°C and after sputtering is shown in Fig. 8.2. Before preparation the Se peak from the Se film and the C peak are clearly visible. The effectiveness of the decapping process is proved with the first spectra of the decapped surface, as no oxygen is detected. Thus, a clean surface is obtained. Besides the Se peak, also the Cu and

In peaks appear, indicating the removal of the Se film. Carbon traces are reduced by annealing at higher temperatures and removed by the sputtering process.

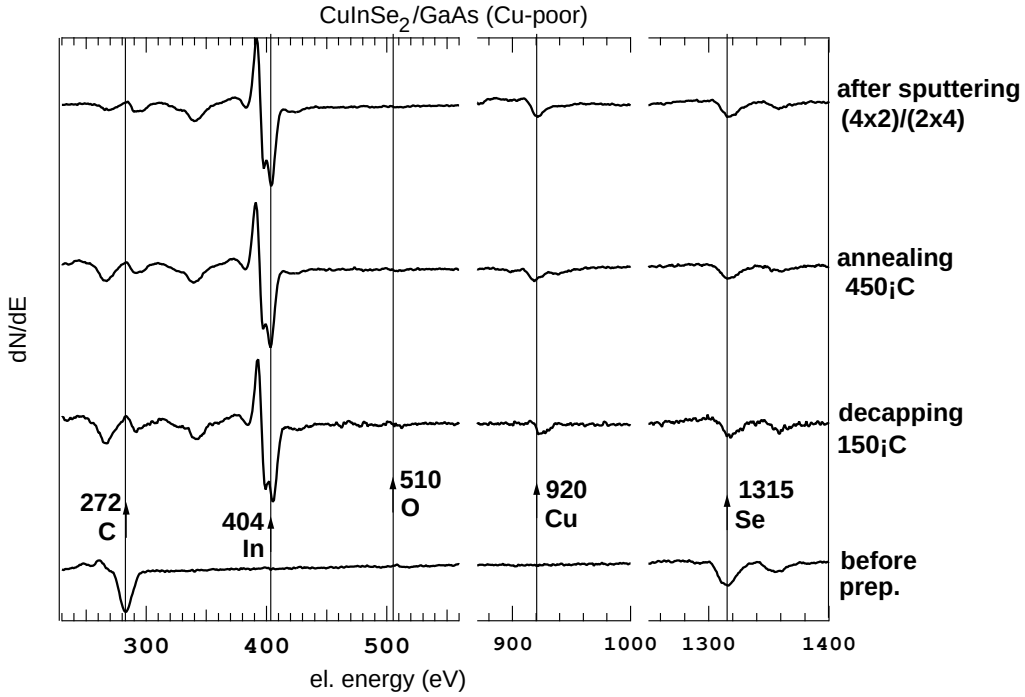

Figure 8.2: AES spectra of the Cu-poor $CuInSe_2$ sample before preparation, after decapping at 150°C, annealing at 450°C and after sputtering. The C, In, O, Cu, Se peaks at 272, 404, 510, 920 and 1315 eV respectively are marked with arrows.

The change of surface composition during the whole preparation process can be seen in Fig. 8.3: The percentage relative concentration of a particular element is plotted versus each preparation step. Before preparation a Cu/In/Se ratio of about 1:3:6 was calculated, indicating the presence of amorphous Se and of the $CuIn_3Se_5$ phase on the surface beneath. The decapped and faceted surface holds a ratio of 1:3:5, implying the removal of the Se film and the presence of the $CuIn_3Se_5$ phase. The detection of $CuIn_3Se_5$ on the $CuInSe_2$ surface is not surprising, as explained in section 4.5. Annealing to higher temperatures leads to some further Se-depletion implying the compete removal of Se rests from the surface. After preparation with sputtering and annealing a clear change of composition is observed: The Cu/In/Se ratio changes to approximately 0.8/1.2/2,

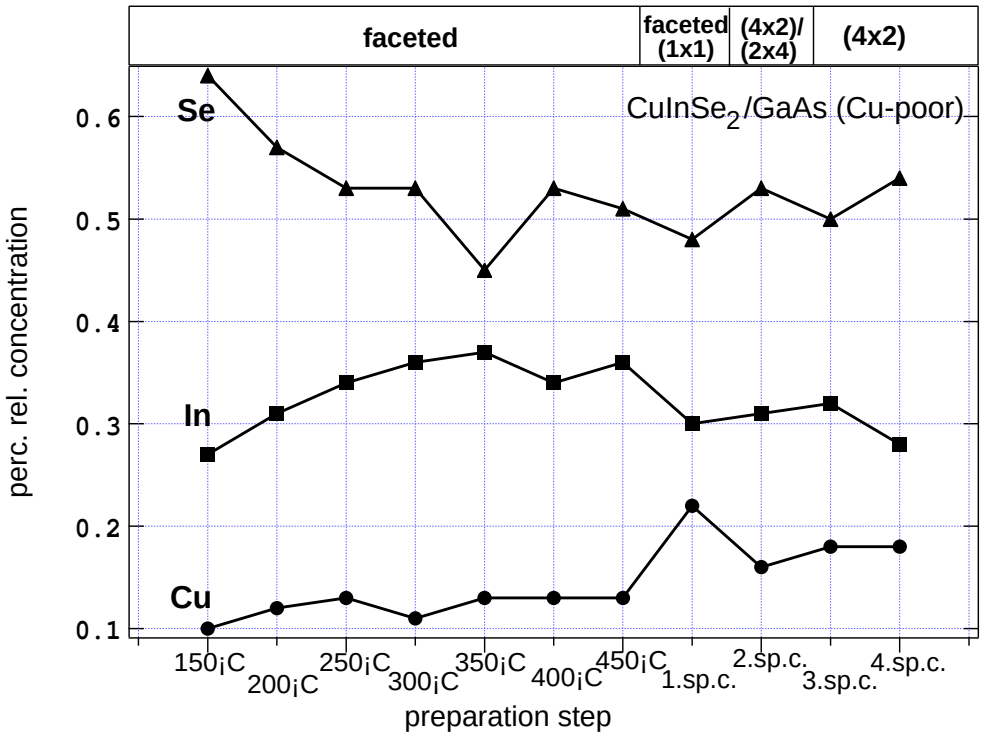

Figure 8.3: The percentage relative concentration of Cu, In, Se is plotted for each preparation step as calculated from the AES spectra of the Cu-poor $CuInSe_2$.

implying a slightly Cu-poor to stoichiometric surface. Thus, the $CuIn_3Se_5$ phase could be removed by sputtering and a $CuInSe_2$ surface could be obtained. As the $CuIn_3Se_5$ phase was found on the faceted $CuInSe_2$ surface and removed by sputtering, it should be related with the facets of the decapped surface. Further and more accurate information about the stoichiometry of the prepared $CuInSe_2$ surfaces will be given in section 8.3 from the SXPS measurements. As already explained in chapter 5, SXPS provides a higher surface sensitivity in comparison to AES.

8.3 Chemical characterization - SXPS

In order to obtain further information about the chemical state of the surface atoms involved in the observed $CuInSe_2$ (001) reconstructions, the Se3d, In4d, Cu2p core level emission lines were investigated with SXPS. After providing an overview of the SXPS

measurements with the survey spectra of the Cu-poor $CuInSe_2$, the spectra of the unreconstructed $CuInSe_2$ surface from the Cu-poor sample obtained by decapping will be analyzed. Then, the spectra measured on the reconstructed surfaces of the Cu-poor and stoichiometric $CuInSe_2$ samples will be studied. The spectra of the Cu-poor $CuInSe_2$ after preparation with a higher ion energy will be given. Then, the valence band spectra are discussed.

8.3.1 Survey spectra

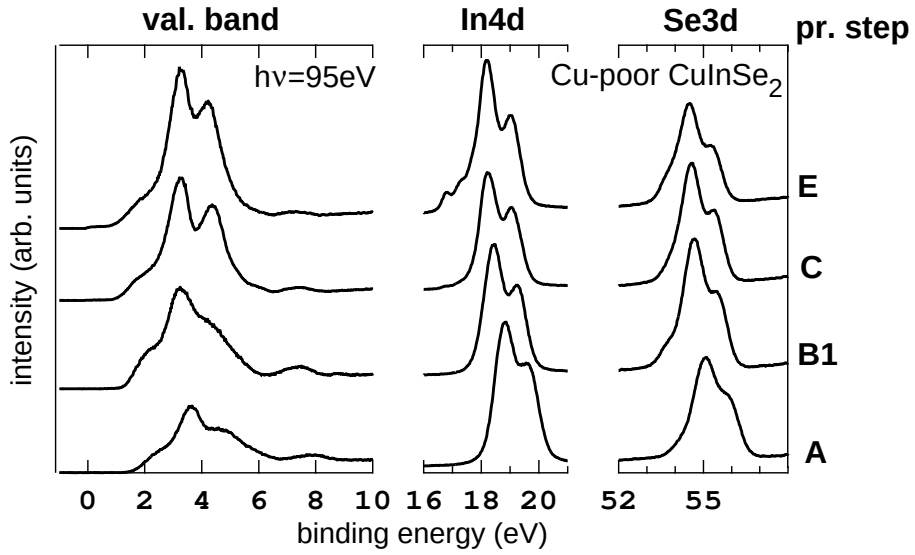

Figure 8.4: Valence band spectra and In4d, Se3d core level spectra excited by 95 eV from the Cu-poor $CuInSe_2$ sample for preparation steps A, B1, C, E.

Spectra of the Se3d, In4d, Cu2p, C1s, O1s core levels and valence band spectra of the Cu-poor $CuInSe_2$ are shown in Fig. 8.4 and Fig. 8.5. The preparation steps are listed in detail in table 8.2. After decapping (prep. step A) traces of carbon and oxygen can be detected on the surface. As the sample had already been stored for a very long time before being measured with SXPS, some contamination can not be excluded. After some short time of sputtering (prep. step B1) the carbon and oxygen traces are significantly reduced. On the prepared surface exhibiting a $(4\times2)/(2\times4)$ pattern, these traces completely dissapear. Thus, the AES results of section 8.2 are further confirmed

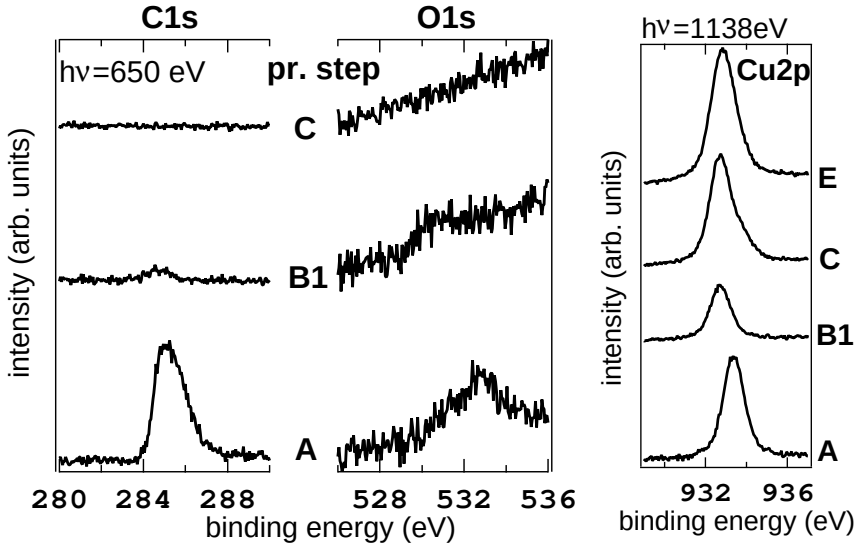

Figure 8.5: C1s and O1s spectra excited by 650 eV (left), Cu2p spectra excited by 1138 eV (right) from the Cu-poor $CuInSe_2$ sample for preparation steps A, B1, C, E.

and the reconstructed surface is in fact free of contaminants. As far as the Se3d, In4d and Cu2p core level spectra are concerned, line shape changes can be discerned upon preparation. Particularly the characteristic doublet structure of the core levels becomes more pronounced from prep. step A to preparation step C, implying the improvement of the surface structure. Surface components are more difficult to distinguish by pure observation. On the In4d level the generation of metalic In on the low binding energy side after preparation step E is quite obvious. On the Se3d spectra a shoulder develops on the low binding energy side after preparation step B1, implying the appearance of surface components. A shoulder develops also on the high binding energy side of the Cu2p peak after prep. step C. These line shape changes will be analyzed in detail with curve fitting in the next sections. With regard to the valence band spectra, their structure is distinctly improved upon preparation, as well.

8.3.2 Decapping of $CuInSe_2$

The decapping process of the Cu-poor $CuInSe_2$ sample is monitored by the Se3d core-level emission spectra excited by 95eV in Fig. 8.6. The Se3d parameters are obtained by fitting the data from the amorphous Se capping layer with one core-level component (Fig. 8.6a). For the next sample condition the Se film was removed. The decapping process

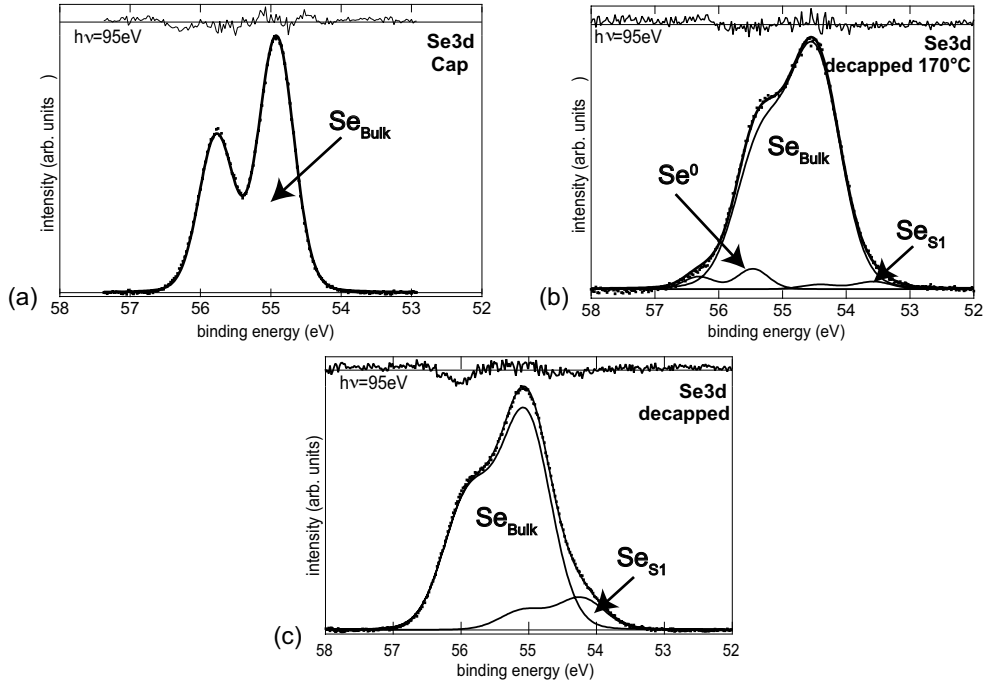

Figure 8.6: Se3d core-level spectra of the capped surface (a), after 10 min decapping at 170 °C (b) and after further 20 min annealing at 300 °C (c). The spectra were obtained from the Cu-poor $CuInSe_2$ sample

was terminated by switching of the heating power immediately after the desorption of the amorphous Se layer, indicated by the change of the gray matt surface appearance into the typical mirror-shiny of an epitaxial CIS (001) surface. This was observed at a sample temperature reading of 170 °C. Still elemental Se remains are present on the surface, as indicated by the component Se^0 on the high-binding energy side of the Se3d emission. At the same time a weak component Se_{S1} on the low-binding energy side arises (Fig. 8.6b).

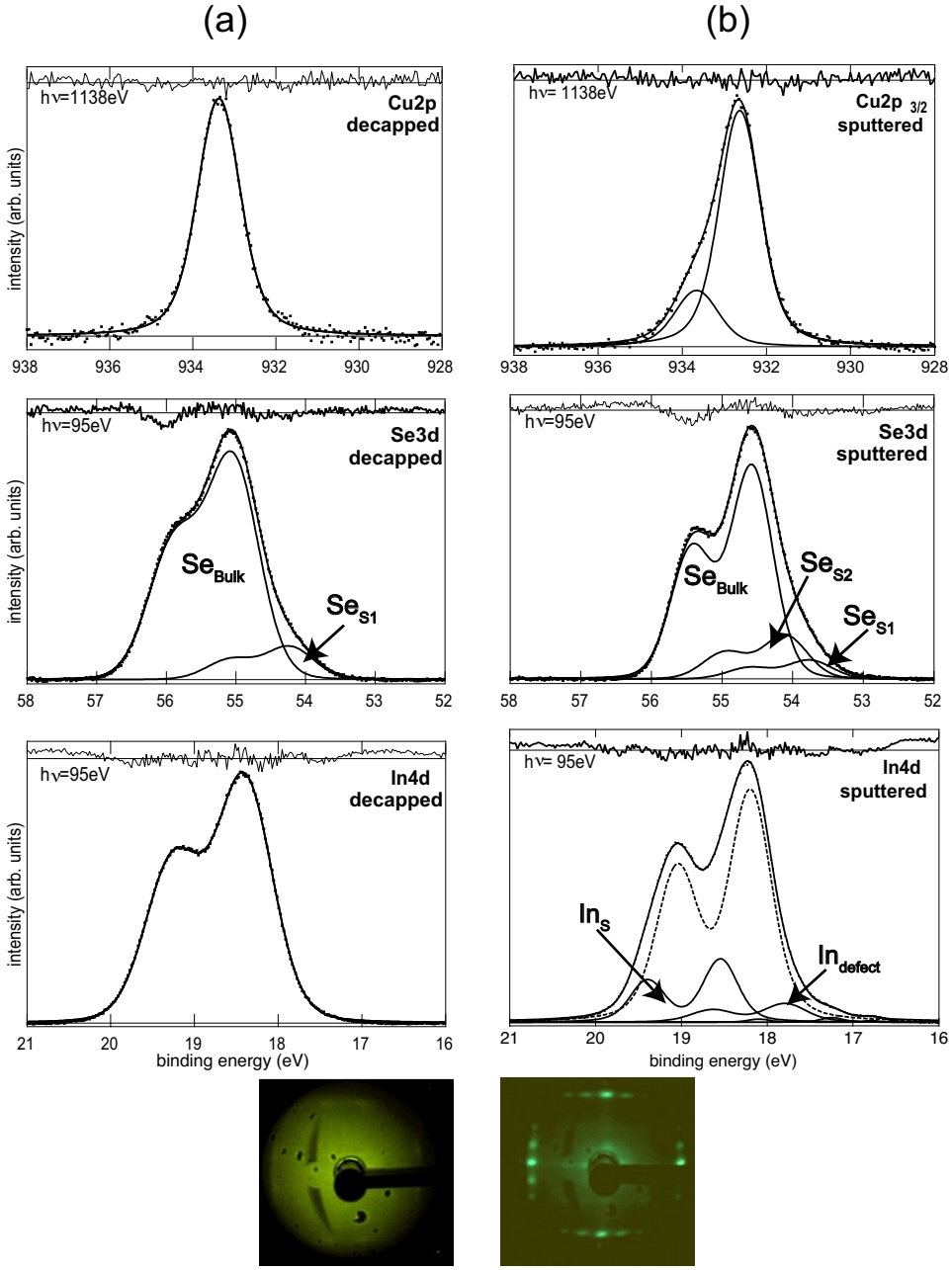

Figure 8.7: Fitted Cu2p, Se3d, In4d core-level spectra (a) of the faceted $CuInSe_2$ (001) surface after decapping (prep. step A) and (b) of a mixed surface structure $(4\times4)/(4\times2)$ after preparation step C (Cu-poor $CuInSe_2$ sample). The intensity ratio of the residuum to the measured peaks lies in the range of 0.02 to 0.06. Below the corresponding LEED patterns of the measured spectra are shown.

After a second decapping step for another 10 min at 300 °C the component Se^0 assigned to elemental Se remains disappears, whereas the additional component Se_{S1} on the low binding-energy side with an energy shift of -0.8eV increases in intensity (Fig. 8.6c) and Fig.8.7a). Thus, elemental Se is completely removed from the surface. Well resolved, single-component In4d and Cu2p spectra are obtained from the same surface (Fig. 8.7a).

8.3.3 The sputtered (001) $CuInSe_2$ surface

Following the preparation of the decapped Cu-poor $CuInSe_2$ sample with Ar^+ ion sputtering and annealing and the appearance of the mixed $(4 \times 2)/(2 \times 4)$ superstructure (preparation step C), the Se3d core level can be deconvoluted into a bulk component Se_{bulk} and two additional components Se_{S1}, Se_{S2} (Fig. 8.7b). In addition to the already observed surface component Se_{S1} on the decapped surface with a shift of -0.8 eV, a second surface component Se_{S2} with a shift of -0.5eV with respect to the bulk component is necessary. Also the Cu2p and In4d core levels are altered after the transition of the faceted surface to a $(4 \times 2)/(2 \times 4)$ superstructure. The previously symmetrical Cu2p core level now exhibits a second component shifted by +1.0 eV towards higher binding energies. The In4d peak exhibits also two additional components shifted by +0.3 eV (In_{defect}) and -0.4 eV (In_S) in comparison to the In4d peak from the decapped faceted surface.

Table 8.3: BE shifts of the surface components in the Cu2p, Se3d, In4d core level spectra of $CuInSe_2$

	Cu2p	Se3d	In4d
BE shift	+1.0	-0.8	+0.4
		-0.5	

The comparison of the results obtained from the Cu-poor sample with those of the stoichiometric one helps to clarify the origin of the surface components. Spectra of the stoichiometric $CuInSe_2$ sample after decapping and Ar^+ ion sputtering show similar surface components (Fig. 8.8). Already after decapping, the LEED pattern of this sample shows a weak, but visible (4×2) reconstruction without facet spots. In this case the corresponding Se3d core level can be deconvoluted into a bulk and only one surface com-

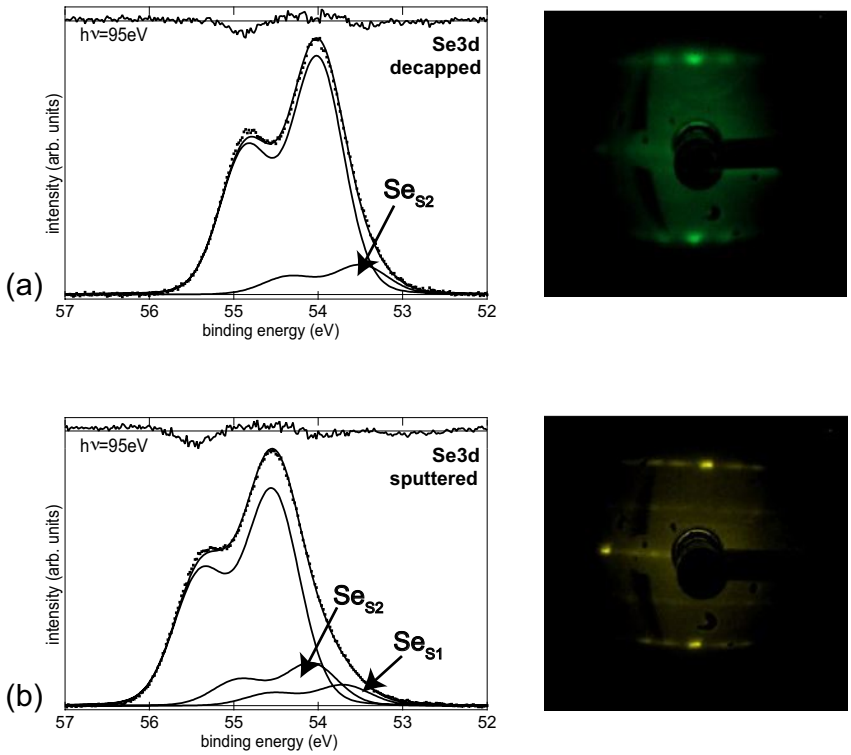

Figure 8.8: Se3d core-level spectra of the stoichiometric $CuInSe_2$. After decapping the LEED pattern shows a weak (4×2) reconstruction (a) and after sputtering and annealing the surface shows a stepped (4×2) reconstruction (b).

ponent Se_{S2} shifted only by -0.5 eV towards the bulk component (Fig. 8.8a). Following preparation by Ar^+ ion sputtering and annealing the LEED pattern of this sample exhibits a sharper (4×2) reconstruction, however, also steps are present on the surface, as the LEED spots are elongated along the $[1\bar{1}0]$ direction. Both surface components, Se_{S1} and Se_{S2} with a shift of -0.8 and -0.5eV are present on the corresponding Se3d spectra (Fig. 8.8b). As far as the Cu2p and In4d spectra are concerned, the same surface components appear for both surface conditions as already mentioned for the sputtered Cu-poor $CuInSe_2$ sample. The BE shifts of the surface components are given in table 8.3.

8.3.4 Excitation with higher energies

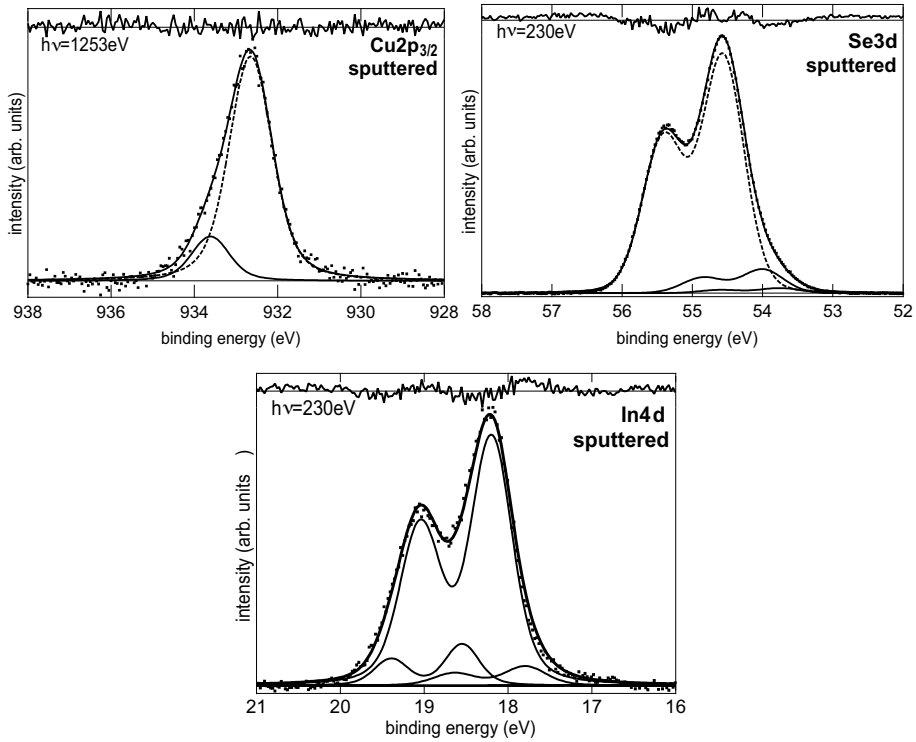

Figure 8.9: Cu2p, In4d, Se3d core level spectra (Cu-poor $CuInSe_2$ sample) of a mixed surface structure $(4 \times 4)/(4 \times 2)$ after preparation step C (Cu-poor $CuInSe_2$ sample). The Cu2p are obtained with an excitation energy of 1253 eV and the Se3d spectra with 230 eV which provide a lower surface sensitivity, due to the varying electron mean free path.

Further SXPS spectra were taken with a higher excitation energy on the Cu-poor $CuInSe_2$ sample (Fig. 8.9) in order to examine if the observed additional components are actually deriving from surface atoms. As described in chapter 5, the highest surface sensitivity for the measured core levels is obtained by about 95eV. With increasing excitation energy the surface sensitivity decreases. As a result the components in Cu2p and Se3d prove to be surface components, as they decrease in intensity with increasing excitation energy. The component on the high-binding energy side of the In4d core-level is also a surface component. However, the component on the low binding energy

side should originate from bulk defects, probably generated by the preparation, as its intensity does not change with increasing excitation energy.

8.3.5 Sputtering with higher Ar^+ ion energies

Finally, after obtaining the (4×2)/(2×4) superstructure on the Cu-poor $CuInSe_2$ sample, the sample was subjected to another sputtering/annealing cycle, which resulted in the generation of metallic In (preparation step E). The intensity of the LEED spots decreased significantly in contrast to first preparation series where the same preparation lead to a clear and bright (4 × 2) reconstruction (Fig. 8.1d). In experiments where higher ion primary energies of 1 keV were intentionally applied for sputtering, very similar sample conditions were obtained. It has already been reported in the literature that metallic In was generated during sputtering of $Cu(In_{1-x}Ga_x)Se_2$ with 1keV [101]. Therefore it is supposed that the ion energy regulation had failed and produced higher ion energies during the last preparation step. The spectra of this sample condition are shown in Fig. 8.10. Even two additional components In_1^0 and In_2^0 arise on the low binding energy side of the In4d spectra, at a binding energy position of 16.8 eV and 17.25 eV. The component at 16.8 eV can be easily attributed to metallic In, while the origin of the component at 17.25 eV is not clear, should nevertheless be correlated with high Ar^+ ion energy, as well. The intensity of the component In_{defect} on the high binding energy side attributed to bulk defects increases significantly in comparison to the respective component corresponding to the (4×2)/(2×4) superstructure. This observation supports the assignment of In_{defect} to bulk defects, induced by the sputtering process. Thereupon it is assumed that In atoms from the bulk diffuse towards the surface, leaving defects in the bulk and forming metallic In on the surface. The intensity of the Cu2p surface component decreases, while the intensity of the Se3d surface component shifted by -0.8 eV increases when comparing to the respective spectra corresponding to the (4 × 2)/(2 × 4) superstructure.

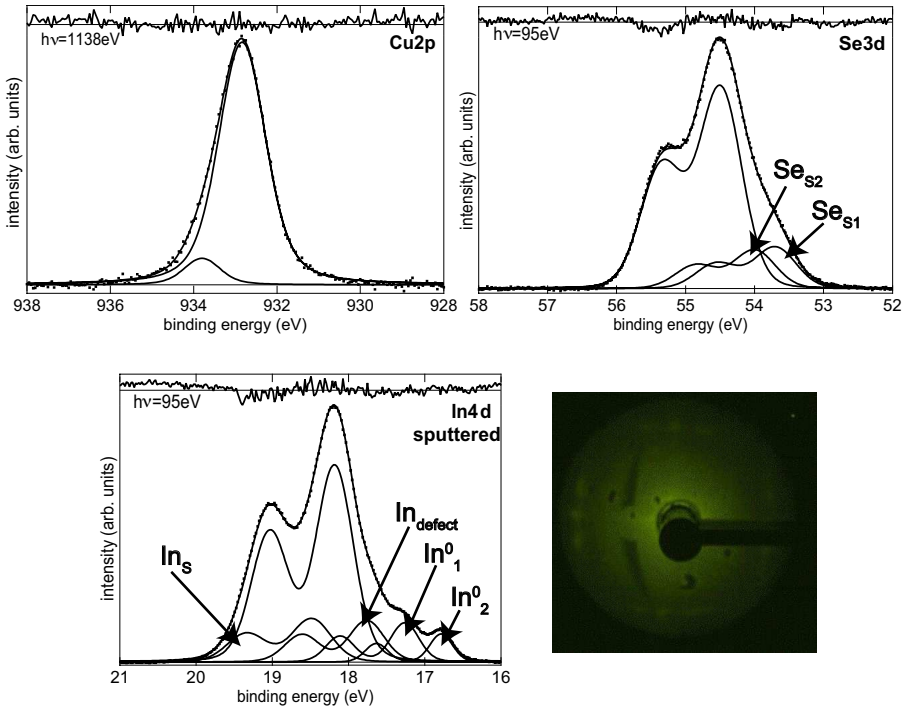

Figure 8.10: Cu2p, Se3d, In4d core-level spectra of the Cu-poor $CuInSe_2$ sample after preparation with an Ar^+ ion energy higher than 600eV (preparation step E) resulting in the generation of metallic In. Consequently also the spots intensity of the $(4\times2)/(2\times4)$ LEED pattern observed on the previous surface state was significantly reduced.

8.3.6 Valence band

Considering the valence band spectra in Fig. 8.11a) of the Cu-poor $CuInSe_2$ sample after decapping, the bonding states In-Se (D) by 8 eV, the Cu3d-Se3p hybride bonds by 4.5eV (C), the Cu3d non-bonding peak around 3.5eV (B) and the Se 4p peak (A) by 2.6 eV are well discerned [64]. After preparation with Ar^+ ion sputtering and annealing the (B) and (C) peaks (Fig. 8.11b) increase by about a factor of 2 in intensity and a distinct valley develops between B and C. With these assignments, the increase of structures B and C by sputtering/annealing can be understood by the increase of the Cu concentration in the surface, which was as well indicated by the increase of the relative Cu3p/In3d intensity in the core levels. Hence, the valence band spectra support the transformation of a Cu-poor surface with presumable $CuIn_3Se_5$ or $Cu_2In_4Se_7$ composition to a near-

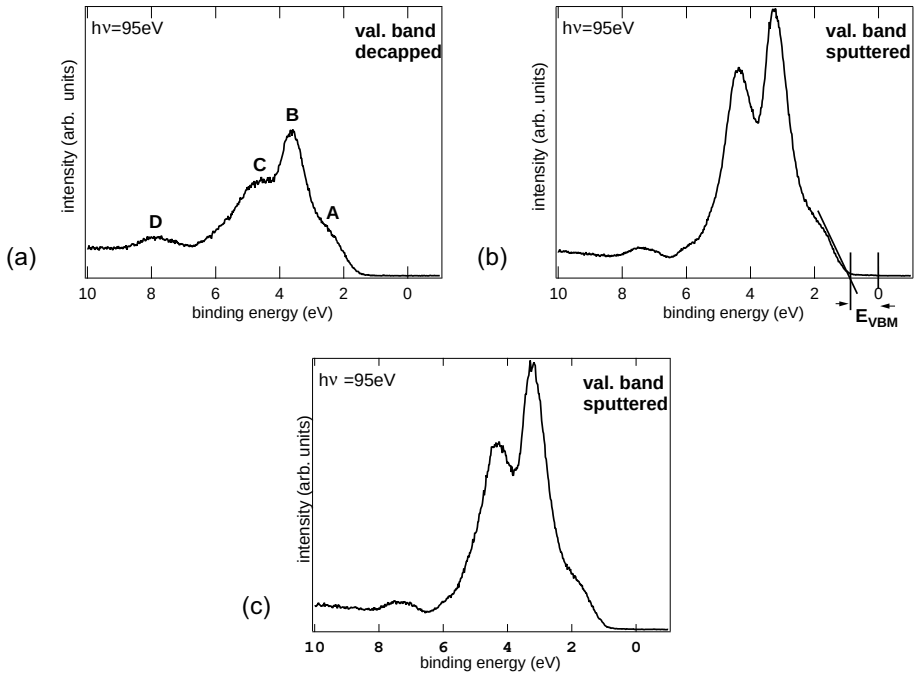

Figure 8.11: Valence band spectra a) after decapping and b) after preparation step C of the Cu-poor sample, c) after preparation of the stoichiometric $CuInSe_2$ sample. The marked features D by 8 eV, C by 4.5eV, B around 3.5eV and A by 2.6 eV correspond to the bonding states In-Se, the Cu3d-Se3p hybrid bonds, the Cu3d non-bonding peak and the Se 4p peak respectively [64].

stoichiometric $CuInSe_2$ surface already implied by the AES results in section8.2.

8.4 Model proposal

In this section the surface components observed on the SXPS spectra of the $CuInSe_2$ surface will be discussed in more detail. Also the similar surface components observed on the prepared $CuGaSe_2$ surface from section 7.4.3 will be taken into consideration. Finally, a general reconstruction model for the (001) chalcopyrite surface will be proposed. Comprising, the decapped faceted $CuInSe_2$ surface shows only one Se3d surface component Se_{S1} shifted by -0.8eV, while the $(4 \times 2)/(2 \times 4)$ and faceted (4×2) reconstructed surfaces of the Cu-poor and stoichiometric sample, respectively, exhibit two

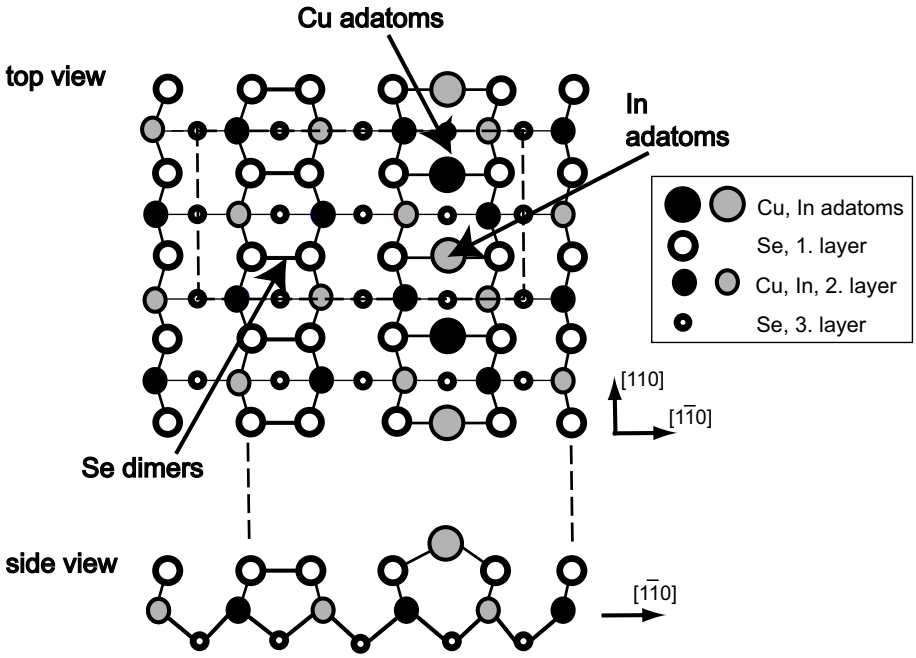

Figure 8.12: Structural model of the $CuInSe_2$ (001) surface with the (4x2) unit cell as implied by the respective LEED pattern. According to the interpretation model, the surface is terminated with Se dimers, Cu and In adatoms ($\theta_{\mathrm{adatom}} = \frac{1}{4}$ML)

Se3d surface components, Se_{S1} and Se_{S2}, of -0.8 and -0.5 eV. However, the Se3d level of the facet-free surface with a weak (4×2) reconstruction contains only one surface component Se_{S2} with a shift of -0.5eV. Hence, the -0.5eV surface component Se_{S2} should be correlated directly with the reconstruction. The origin of the -0.8eV component Se_{S1} is not completely clear, however, it can be related to a Se species participating both in the facet formation and the (2×4) reconstruction. The Cu2p and In4d core levels of all reconstructed surfaces exhibit positive surface core level shifts, which are not present on the spectra of the faceted decapped surface, thus they are also associated with the reconstruction. The In4d component of lower intensity on the low binding energy side is attributed to bulk defects generated by the sputtering treatment, as already mentioned. Furthermore the increase of the [Cu2p$_{3/2}$]:[In3d] intensity ratio by a factor of 2 after the change from the unreconstructed to the reconstructed surface should be taken into consideration. This stoichiometry change is interpreted as a transition from

a Cu-deficient surface phase like $CuIn_3Se_5$ or $CuIn_2Se_{3.5}$ to a surface composition close to $CuInSe_2$. Hence the $(4 \times 2)/(2 \times 4)$ and (4×2) reconstructed surfaces are associated with near-stoichiometric $CuInSe_2$ surfaces.

The reconstructed $CuGaSe_2$ surface shows similar surface core level shifts: A surface component shifted by -0.8eV is observed on the Se3d spectra, as well as a positive surface component on the Ga3d spectra which analogously to $CuInSe_2$ should be correlated with the reconstruction. The observed shifts of the surface Cu, In, Ga and Se components are similar to those observed on ZnSe (100) surfaces [117]. For the Se-rich (2×1) reconstruction of the ZnSe (100) surface a Se3d surface component shifted towards lower binding energies is observed which is attributed to Se dimers. For the Zn-rich $c(2 \times 2)$ reconstruction a Zn3d surface component shifted towards higher binding energies appears which is attributed to Zn adatoms. Theoretical calculations for the ZnSe (100) surface predict also a (4×2) reconstruction, as a combination of Se dimers and Zn adatoms. We propose a similar model for the interpretation of the (4×2) reconstruction of the chalcopyrite (001) surface (Fig.8.12). The observed Se3d surface component shifted by -0.5eV is attributed to Se dimers. The Cu2p surface component shifted by +1.0 eV and the In4d component shifted by +0.4 eV are attributed to Cu and In adatoms respectively. The observed surface components on the Se3d and Ga3d core levels of the $CuGaSe_2$ surface can be analogously attributed to Se dimers and Ga adatoms respectively. For the $CuGaSe_2$ (001) surface a (4×1) reconstruction was obtained in contrast to the (4×2) reconstruction of $CuInSe_2$ (001). As can be seen from Fig. 8.12, the $\times2$ periodicity along the [110] of the surface unit cell is due to the alternation of Cu and In/Ga atoms along the [110]. With this structural model the $\times1$ periodicity of the $CuGaSe_2$ (001) along the [110] could be explained by a Ga/Cu disorder in the adatom chains.

8.5 Stoichiometry and morphology

Another remarkable point is the dependence of the surface morphology on the Cu/In or Cu/Ga bulk and surface ratio, as well as on the preparation method. The predicted tendency of the chalcopyrite surfaces to form {112} facets [53, 86] is confirmed, however, it is

possible to remove these facets or steps by sputtering and obtain a flat (001) chalcopyrite surface. According to the obtained LEED-patterns in relation to the bulk stoichiometry of the corresponding samples, Cu-poorer surfaces tend to form facets and steps more easily, while Cu-richer surfaces are flater but also show a weaker reconstruction. A flat reconstruction is obtained only for an optimal Cu/In or Cu/Ga ratio. The surface ratio Cu/In is also correlated with the surface morphology. In this work the surface ratio was estimated by using the ratio of the relative peak intensities of the Cu2p and In4d peaks as a qualitative indicator. An intensity ratio of 0.8 corresponds to a nearly stoichiometric surface. The surface Cu/In ratio corresponding to the faceted LEED pattern (Fig. 8.1a)) of the Cu-poor $CuInSe_2$ sample amounts to 0.5, while the Cu/In ratio of the reconstructed surface (Fig. 8.1b)) averages to 0.8, thus it is Cu-richer. Especially as far as the stoichiometric $CuInSe_2$ sample is concerned, during the transition from the weak (4×2) reconstruction (Fig. 8.8a)) to the sharp but stepped (4×2) reconstruction (Fig. 8.8b)), the surface Cu/In ratio slightly decreases from 0.87 to 0.76. Consequently the formation of steps or facets is associated with a lower Cu/In ratio and thus, with In (or Ga) surface atoms. The (001) surface tends to form facets or steps, however, a flat (001) surface is energetically also possible and is correlated with a slightly higher Cu/In surface ratio in comparison to the faceted/stepped (001) surface. With an even higher Cu/In surface ratio, the surface is still flat, but the spots of the reconstruction weaken as well.

8.6 Surface band bending

The Valence Band Maximum E_{VBM} was plotted in Fig. 8.13 versus the Cu/In ratio of the Cu3d, In4d peak intensities of the corresponding $CuInSe_2$ surfaces measured by different experiments. The Valence Band Maximum E_{VBM} was estimated by a graphical extrapolation of the steep emission onset to zero signal. The two circles including different data points correspond to Cu-poor and stoichiometric samples, thus they are reference data for Cu-poor and stoichiometric $CuInSe_2$ surfaces.

In addition, the VBM in the bulk was calculated according to the formula

$$ln\frac{n}{N_{eff}} = (E_F - E_V)\frac{e}{kT} \tag{8.1}$$

by 0.16 eV. The value for the defect concentration n were taken from [116] and lies by $2 \cdot 10^{16} cm^{-3}$ whereas the value for the effective density state was taken from [119] and lies by $1.8 \cdot 10^{19} cm^{-3}$. This calculated value of the VBM by 0.16 eV is much lower than the one of 0.8 eV measured on the stoichiometric $CuInSe_2$ surface, implying a surface band bending. This surface band bending of the stoichiometric surfaces can be correlated with charged surface states of the reconstruction.

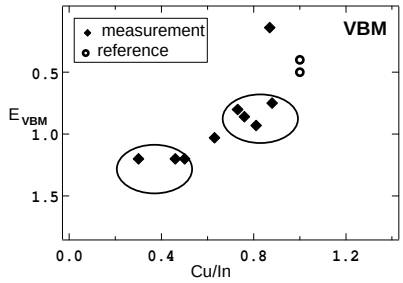

Figure 8.13: The VBM is plotted versus the Cu/In ratio of the Cu3d, In4d peak intensity of the corresponding $CuInSe_2$ surfaces as measured and as derived from crystals by Klein et al. [118] and Löher et al. [84]. The two circles including different data points correspond to Cu-poor and stoichiometric samples

8.7 Conclusions

The preparation by Ar^+ ion sputtering and annealing optimized on the $CuGaSe_2$ (001) surface was applied successfully also on the $CuInSe_2$ (001) surface and led to clean and well ordered surfaces. It was further combined with the Se decapping method so that different surface structures could be obtained. The surfaces were free of O contaminants already after decapping, while C traces were completely removed after additional sputtering. The surfaces of layers with a Cu-poor Cu/In bulk ratio were completely covered with {112} facets after decapping. Further preparation by Ar^+ ion sputtering

and annealing removed the facets so that a mixed $(4 \times 2)/(2 \times 4)$ reconstruction was obtained. By prolonging the preparation time by Ar^+ ion sputtering and annealing, the mixed $(4 \times 2)/(2 \times 4)$ reconstruction was transformed into a clear (4×2) reconstruction. According to the measured changes of the surface composition, on the faceted surface the $CuIn_3Se_5$ phase is present, whereas after sputtering a stoichiometric surface is obtained. Thus, the facets can be associated with the $CuIn_3Se_5$ phase, whereas the reconstructions are obtained on a $CuInSe_2$ surface.

Slightly different patterns were observed for a sample with a stoichiometric Cu/In bulk ratio. After decapping, already a weak (4×2) reconstruction was observed. After short preparation by Ar^+ ion sputtering and annealing the intensity of the LEED spots increased, however, also steps appeared on the surface. Remarkably, during this transition, the Cu/In surface ratio slightly decreased.

Hence, the surface structure is strongly correlated with the Cu/In bulk ratio, as well as with the implemented preparation method. The (001) surface tends in fact to form facets or steps, as it was expected, however, a flat (001) surface is energetically also possible. A Cu-poorer Cu/In bulk ratio is associated with a faceted surface, while a Cu-richer Cu/In bulk ratio with a flat surface with a weaker reconstruction. Facets can be removed by sputtering. Accordingly, also the surface Cu/In ratio is reduced from the flat surface with a weak reconstruction over the facet-free surface with a clear reconstruction to the faceted surface.

Surface band bending was observed on the SXPS spectra which should be caused by charged surface states of the reconstruction. Surface components were found in all the Cu3d, In4d, and Se3d core levels. Two surface components were fitted in the Se3d spectra with a shift of -0.5 eV and -0.8 eV towards the bulk. In the In4d spectra one surface component with a +0.4 eV shift was found, as well as a component related to In defects in the bulk. In the Cu3d level one surface component shifted by +1.0 eV was detected. By considering results of the similar ZnSe (100) surface, a model for the interpretation of the (4×2) reconstruction is proposed. Thus, the observed Se3d surface component shifted by -0.5 eV is attributed to Se dimers, while the Cu2p surface

component shifted by +1.0 eV and the In4d component shifted by +0.4 eV are attributed to Cu and In adatoms respectively. As similar surface components were observed on the $CuGaSe_2$ surface, the same model is proposed for the interpretation of the $CuGaSe_2$ (4×1) reconstruction, as well. The $\times 1$ periodicity along the [110] in the $CuGaSe_2$ case could be explained by a Ga/Cu disorder in the adatom chains, which is not present on the $CuInSe_2$ surface with a $\times 2$ periodicity.

9 Growth of ZnSe on the $CuGaSe_2$ (001) surface

Besides the understanding of the surface properties of the chalcopyrite (001) surface, the investigation of the interface properties between chalcopyrite surfaces and their corresponding buffer layers is also of importance towards optimization of solar cells, as already discussed in chapter 2. The knowledge of the crystalline structure of the growing buffer layer as well as the interface reactions during deposition can contribute in a better growth control of these layers. ZnSe represents an alternative material for buffer layers, as it is supposed to be more friendly to the environment and it absorbs a larger range of sun radiation in comparison to CdSe. However, few investigations have been carried out on the ZnSe/$CuGaSe_2$ interface [120]. With Raman and luminescence spectroscopy information can be acquired on the structural properties of the bulk and consequently also on modifications of the crystal quality during growth.

In this work the deposition process of ZnSe on $CuGaSe_2$ (001) films was studied with Raman and luminescence spectroscopy excited by the 488 nm of an Ar^+ laser under UHV conditions. The Raman measurements were performed in a quasi backscattering geometry. The $CuGaSe_2$ sample (C), grown under high Cu-excess, was prepared with Ar^+ ion sputtering and annealing like described in chapter 6. Subsequently ZnSe was deposited on the clean surface at 700 °C at a rate of 0.65 nm/min in steps of 1,2,3,5 and 10 ML. After each preparation step the surface was monitored additionally with LEED and AES.

9.1 Surface structure and morphology during growth

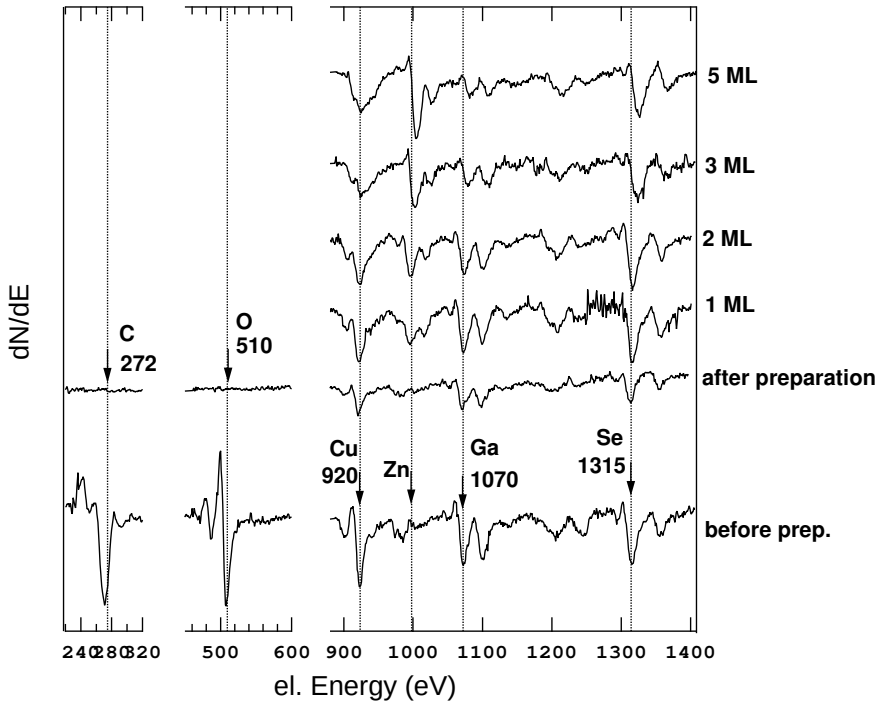

Figure 9.1: AES spectra of the $CuGaSe_2$ (001) surface before preparation and after each ZnSe deposition step.

According to the AES spectra in Fig. 9.1 the sample surface is free of contaminants after preparation, as the C and O peaks completely disappear. The Zn peak is already discernible after the deposition of 1 ML of ZnSe and increases with further deposition. For the evaluation of the AES spectra the percentage relative surface concentration of the different elements was calculated as described in section 6.4 and is shown in Fig. 9.2a). After preparation some Cu-depletion is observed as already reported in section 7 so that the Cu/Ga ratio changes from 0.76 to 0.64. Also during deposition further Cu-depletion takes place in the vicinity of the surface, as the Cu/Ga ratio reaches 0.36 by a ZnSe coverage of 5 ML. As already mentioned in section 3.2, Cu has the highest mobility among the $CuGaSe_2$ species, thus some Cu diffusion in the bulk could take place during the ZnSe deposition due to the elevated temperature. The Zn concentration raises with

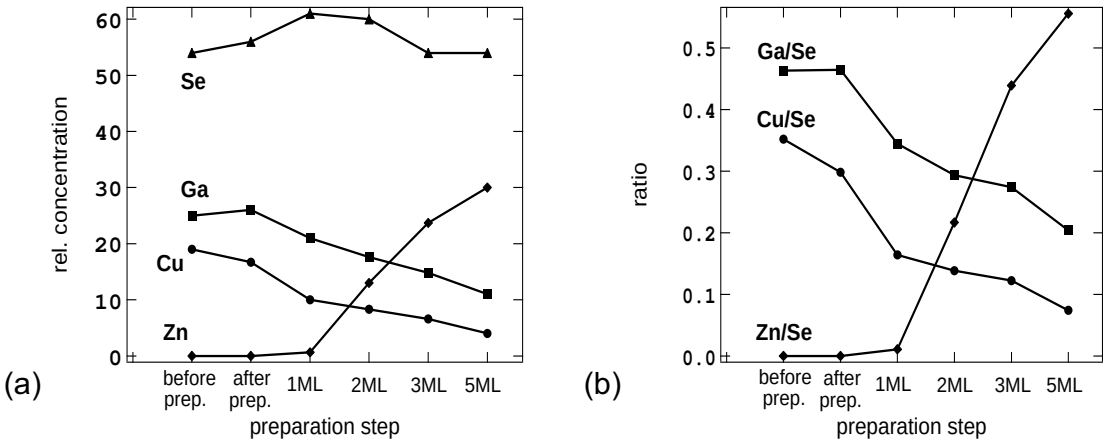

Figure 9.2: a) Percentage relative concentration of Cu, Zn, Ga, Se as calculated from the AES spectra before, after preparation and after each ZnSe deposition step.b) Ga/Se, Cu/Se and Zn/Se ratios for the same process.

deposition as expected, whereas the Se concentration varies between 50% and 60%, as both $CuGaSe_2$ and ZnSe contain Se. The slight Se depletion between the 1 and 3 ML deposition steps can be related with slight Cu, as well as Zn diffusion into the bulk. This assumption will be further supported by the luminescence spectra of section 9.2. In Fig. 9.2b) the relative concentrations are plotted with respect to Se, so that the continuous Ga and the even stronger Cu depletion are clearly distinguished.

The LEED pattern of the clean $CuGaSe_2$ surface obtained after sputtering and annealing shows the (4×1) reconstruction with steps along the $[1\bar{1}0]$ direction. The steps do not recede with further sputtering due to the high Cu-excess offered during growth as already mentioned in section 7. After the deposition of 1 and 2 ML of ZnSe the (4×1) LEED pattern can still be discerned (Fig. 9.3). After the deposition of 3 ML of ZnSe the LEED pattern turns into a weak (2×1) structure with broad spots. By 10 ML the LEED spots of this (2×1) structure are higher in intensity. Hence the $CuGaSe_2$ (4×1) turns into the already observed (2×1) reconstruction (chapter 4), typical for the Se-rich (001) ZnSe surface.

In order to investigate the growth modus of ZnSe on $CuGaSe_2$, the peak height/

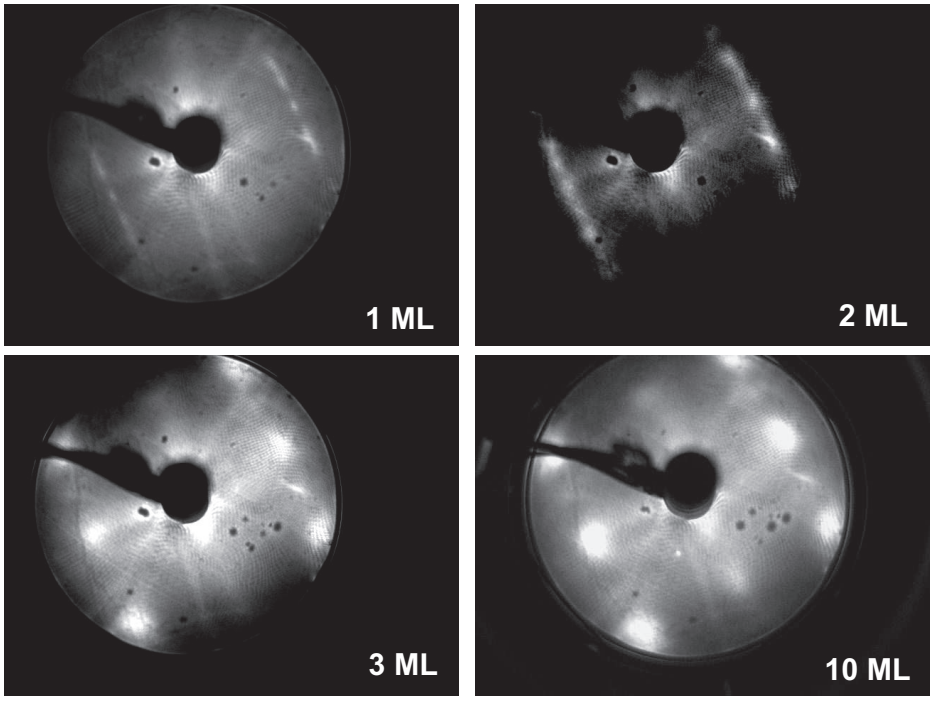

Figure 9.3: LEED patterns of the ZnSe/$CuGaSe_2$ (001) surface, taken at a primary electron energy of 43 eV for 1ML, 2ML, 3ML and 10ML of ZnSe respectively. The pattern symmetry for 1 and 2 ML corresponds to a still visible but weak (4×1) with steps along the $[1\bar{1}0]$ direction, while for 3 and 10 ML to a weak (2×1) structure with broad spots indicating a rough surface.

coverage relation of the AES signals relative to the corresponding Se intensity

$$\frac{I_x}{I_{x0} I_{Se}}$$

was plotted in Fig. 9.4, as described in section 6.4. I_x is the peak to peak intensity of the Auger signal of a particular element, I_{x0} the intensity of the Auger signal of the uncovered surface for Cu, Ga, Se and of the covered surface for Zn. The gradient of the plotted ratio is not linear for all elements and shows a weak attenuation. The inelastic mean free path was calculated from the plotted ratio by 170 Å for Cu and 180 Å for Ga. The theoretical values for the inelastic mean free path were calculated by 12 Å for Cu and 13 Å for Ga, thus they are much lower than the experimental ones. These observations suggest that rather island formation takes place instead of layer-by-layer

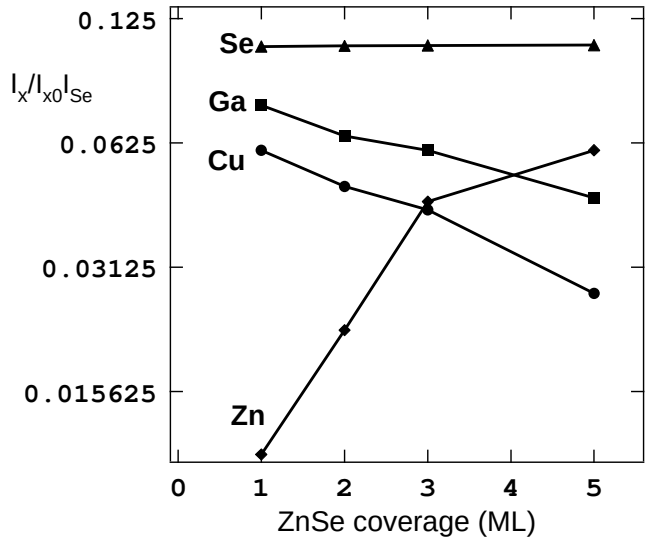

Figure 9.4: Peak height/ coverage relation of the AES signals of the different elements relative to the corresponding Se intensity during the ZnSe deposition. The weak attenuation of the curves implies island formation instead of layer by layer growth.

growth. Considering the LEED patterns of Fig. 9.3, after deposition of 1 and 2 ML of ZnSe the reconstruction pattern of $CuGaSe_2$ can still be discerned, further indicating an incomplete coverage of the surface with ZnSe, in accordance to the observations from the above. After 3 ML the LEED pattern characteristical of the ZnSe (001) surface is obtained, hence the surface is completely covered by ZnSe. The broad LEED spots of the (2×1) are indicative for a rough surface, which can be correlated with the mentioned island formation.

9.2 Deposition of ZnSe and bulk properties of $\mathrm{CuGaSe_2}$

On the photoluminescence spectra recorded before preparation (Fig. 9.5), two peaks of different intensity are visible. The smaller peak at lower energies corresponds to the emission of the GaAs substrate. The higher peak has a low resolution as it was taken in room temperature. However, it is almost identical with PL spectra obtained from $CuGaSe_2$ samples of similar stoichiometry with a temperature ramp ranging from 20 to 300 K [121]. The contributions at 1.66 and 1.71 eV corresponding to donor-acceptor pair transitions of DA2 and DA1 respectively [103, 22] were clearly visible at temperatures below 60 K. The intensity ratio of DA2/DA1 is correlated with the Cu/Ga ratio in

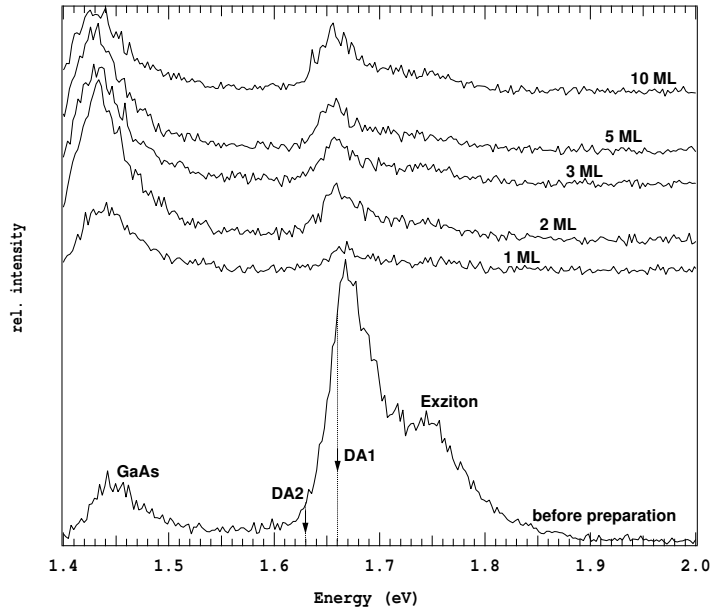

Figure 9.5: Photoluminescence spectra of the $CuGaSe_2$ (001) surface before preparation and after each ZnSe deposition step.

the bulk and is thus indicative for the amount of the offered Cu-excess during growth [103, 22]. By comparison to the corresponding spectra of Xue et al. [121], the measured sample was grown under moderate to high Cu-excess. The high-energy shoulder of this peak originates from a free-to-bound-exciton. After deposition, the shape of the peaks corresponding to the donor-acceptor transitions does not change significantly. In contrast, the intensity of the GaAs emission increases during deposition. Some Zn could diffuse in the Zn-doped GaAs substrate during deposition and enhance the GaAs emission. The assumption of Zn diffusion into the bulk was also made by the evaluation of the AES results in section 9.1.

On the Raman spectra (Fig.9.6) taken before preparation two peaks are observed. The peak at 182 cm^{-1} corresponds to the A_1 mode. On the right shoulder of this peak a light asymmetry can be seen originating from the B_2 at 192 cm^{-1}. The lower peak at 270 cm^{-1} corresponds to the E_1 mode [122, 123]. According to Xue et al. [121] these spectra originate from a sample grown under high Cu-excess conditions. During

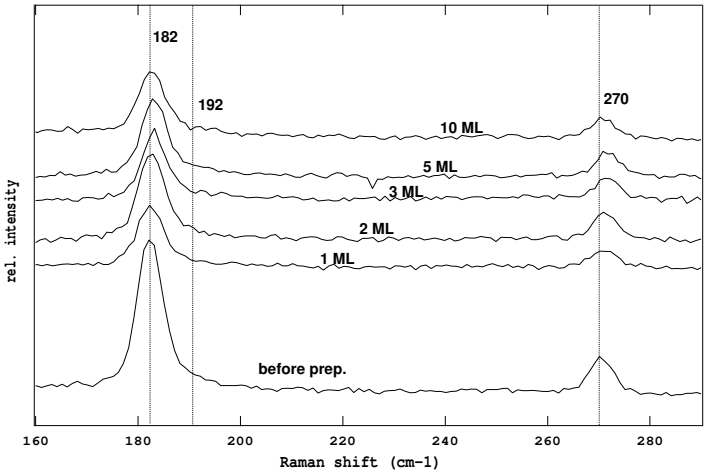

Figure 9.6: Raman spectra of the $CuGaSe_2$ (001) surface before preparation and after each ZnSe deposition step.

deposition no significant changes are observed on the spectra. Considering the fact that also the recorded PL spectra remain almost the same during deposition, the bulk structure should not be influenced by the preparation process and the ZnSe deposition. No significant interface reaction takes place, as well.

9.3 Summary

Summarizing, it was shown that preparation of the $CuGaSe_2$ (001) surface by sputtering and annealing does not affect the bulk properties of the $CuGaSe_2$ film. Furthermore it was possible to grow ZnSe on the clean $CuGaSe_2$ surface without influencing the structural properties of the $CuGaSe_2$ bulk, as well. During deposition no significant interface reaction is observed. However, apparently some Zn diffuses into the Zn-doped GaAs during the ZnSe deposition of 1 to 3 ML. The obtained LEED-patterns and the evaluation of the AES spectra indicate island formation during the whole deposition process. The $CuGaSe_2$ surface is completely covered by ZnSe after 3 ML of deposition. The LEED pattern of the grown ZnSe film shows a (2×1) reconstruction, characteristical for the Se-rich ZnSe (001) surface. The broadening of the LEED spots is characteristical for an irregular and rough surface.

10 Deposition of Mn on the $ZnGeP_2$ (001) surface

Besides $CuGaSe_2$ and $CuInSe_2$ also other chalcopyrite materials have attired interest for different applications. $ZnGeP_2$ seems to be suitable for the use in semiconductor spintronics and magnetooptics [124]. It was already observed that $ZnGeP_2$ obtains the properties of a ferromagnetic substance after the introduction of magnetic impurities in its crystal. In order to develop a room temperature spin injector, high-temperature ferromagnetic layers of $(Zn, Mn)GeP_2$ on III-V substrates were introduced. For their optimization it is nescessary to understand the magnetic properties of pure $ZnGeP_2$ and $ZnGeP_2$ doped with Mn and subsequently obtain knowledge of their spin system and magnetic ordering. Magnetic resonance effects have already been observed on $ZnGeP_2$ doped with Mn by Baranov et al. [125], [126]. They are supposed to result from the substitution of Zn sites by incorporated Mn atoms. This project aimed at the study of the properties of $ZnGeP_2$ epitaxial films grown on GaP (001) single crystal substrates with MOCVD [127] and subsequently doped with Mn. Here the experimental part including the deposition of Mn on the $ZnGeP_2$ surface will be discussed.

10.1 Preparation

The $ZnGeP_2$ samples were introduced into the vacuum chamber and prepared with Ar^+ ion sputtering and annealing. However, due to the known hardness of $ZnGeP_2$ a higher ion energy as for $CuGaSe_2$ was chosen, namely 1keV. The samples were sputtered and simultaneously annealed at 400 ° for 3h and subsequently annealed at the same

temperature for 1h. Mn was deposited on the clean surface with a rate of 8-9 nm/min so as to obtain a Mn layer with a thickness of 50-70 nm. Subsequently the samples were annealed at 500 °C for 30 min so as to further induce the diffusion of Mn into the bulk of $ZnGeP_2$ and improve the modified bulk structure (see also Table 10.1). The whole process was monitored with AES and LEED.

Table 10.1: Preparation and deposition procedure for the $ZnGeP_2$ (001) surface

preparation	prep. step
3h sputter/anneal 400 °C	A
1h anneal 400 °C	
Mn deposition	B
anneal 500 °C	C

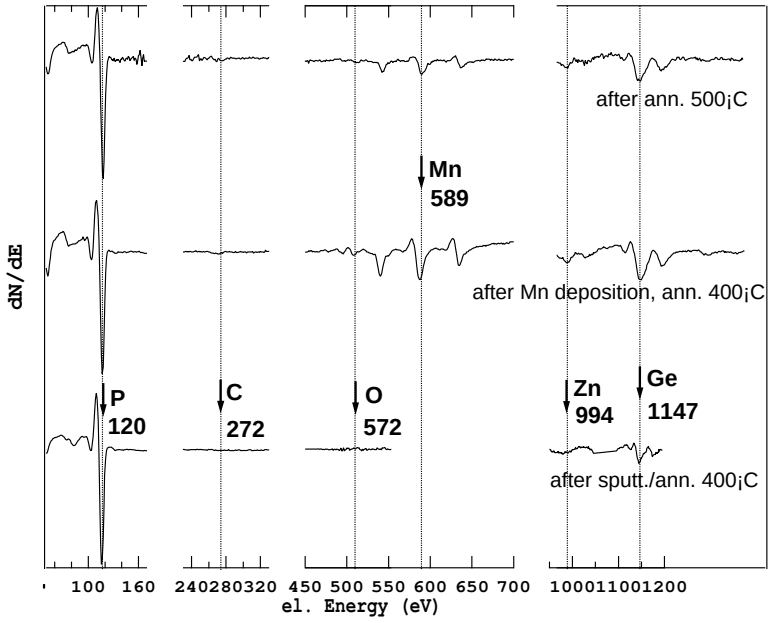

Figure 10.1: AES spectra of $ZnGeP_2$. All AES spectra are normalized to the P-peak at 120 eV and displayed on the same intensity scale. Spectra are shown after preparation, after Mn deposition and annealing at 400 °C, and after annealing at 500 °C.

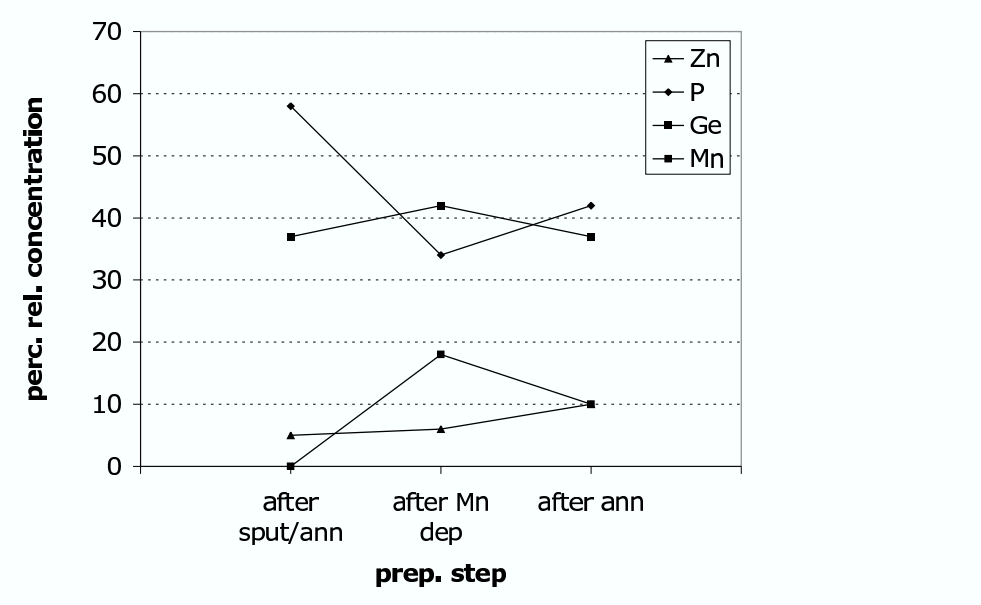

Figure 10.2: percentage relative concentration of Mn, Zn, Ge, P as calculated from the AES spectra of $ZnGeP_2$.

10.2 Stoichiometry

After preparation with Ar^+ ion sputtering and annealing at 400 ° the $ZnGeP_2$ surface is free of carbon and oxygen contaminants, as shown by the AES spectra in Fig.10.1. The peaks of P at 120 eV, Zn at 994 eV and Ge at 1147 eV are also discernible. After Mn deposition the Zn percentage relative concentration (Fig.10.2) remains almost the same, while the Ge concentration slightly rises and the P concentration clearly diminishes. It appears that already some Mn atoms substitute Zn and P atoms in the area close to the surface. After annealing at 500 °C the Mn concentration decreases so that the expected diffusion of Mn atoms into the bulk is confirmed. The increase of the Zn and P concentration after this annealing step can be explained by the generation of Zn and P vacancies in the bulk and the diffusion of Zn and P atoms to the surface [125], [126]. Therefore the intended incorporation of Mn into the $ZnGeP_2$ crystal seems to be succesful.

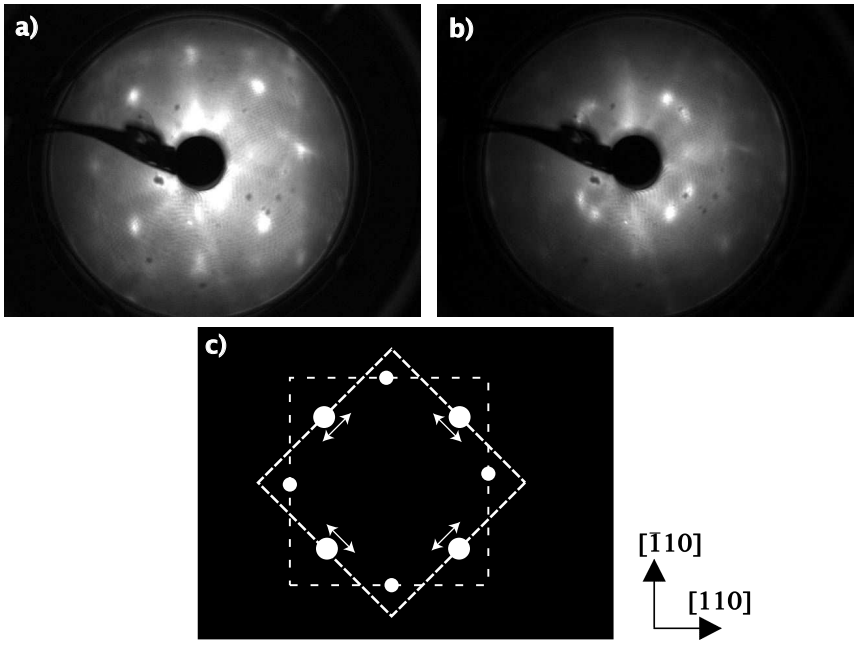

Figure 10.3: LEED patterns of the $ZnGeP_2$ (001) surface after preparation with Ar^+ ion sputtering and annealing, a) for 46eV and b) for 59eV. In a) a (1×1) structure is visible, as well as the spots of a second (1×1) structure turned by 45° relatively to the first one. In b) the spots of the (1×1) structure split and move outwards across the [010] and [100] direction. The corresponding symmetry is shown in c)

10.3 Suface structure

As far as the surface structure is concerned, after preparation the LEED pattern of the clean $ZnGeP_2$ surface in Fig. 10.3a) shows two different (1×1) structures, turned by 45° towards each other. Therefore the surface is supposed to form two different lattices rotated by 45° towards each. In Fig. 10.3b) the spots of the smaller (1×1) structure split and move along the [010] and [100] direction with increasing electron energy, implying the presence of facets. From the geometrical construction in Fig. 10.4 it is possible to estimate the orientation of the facets corresponding to the facet spots. The arrows show the direction in which the facet spots move by increasing electron energy. Also the reciprocal rods corresponding to the facet spot in the front and to the (00) spot are drawn. By increasing the electron energy, the facet spot and the corresponding rod

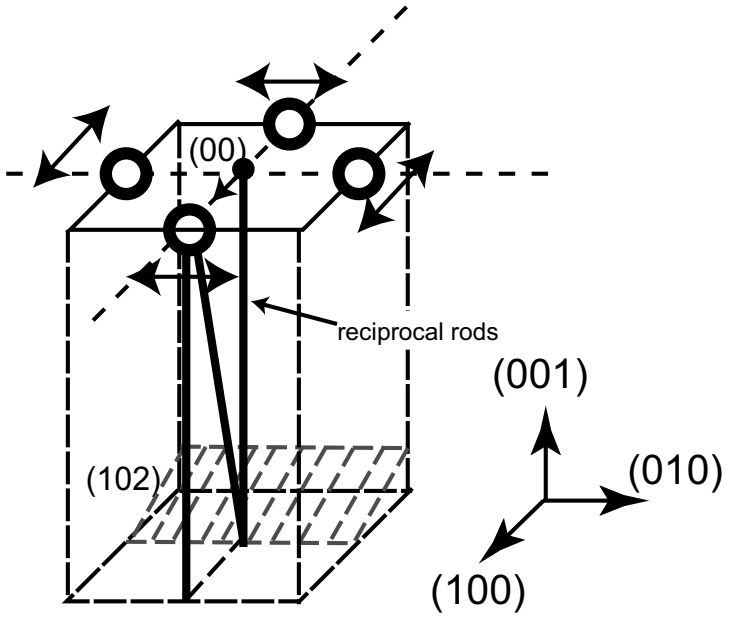

Figure 10.4: Geometrical construction for the estimation of facets orientation. The facet spots move across the marked directions with increasing electron energy. The reciprocal rods corresponding to the facets spots, as well as to the (00) spot are also drawn. In case of a flat surface, all LEED spots and consequently the reciprocal rods should move towards the (00) spot. If the surface is tilted, like in the case of a facet, the spots move towards the (00) spot of the tilted surface with increasing electron energy, which corresponds also to a "tilted" reciprocal rod. Therefore the orientation of a facet can be estimated from the direction in which the facet spot moves with increasing electron energy.

should move towards the (00)-spot. Instead the facets spot moves along the [100] and [010] direction. This means that the rod of the corresponding surface is tilted towards the same direction, as drawn. The plane perpendicular to the rod tilted in the [100] direction corresponds to a surface like the (102). By taking into consideration the remaining facet spots, also $(\overline{1}02)$, (012) and $(01\overline{2})$ facets should be present on the crystals surface. In order to determine exactly the angle of the facets in relation to the sample surface, it is nescessary to know the angle of the tilted rod towards the rod corresponding to the (001) surface. Therefore a detailed analysis of the facets movement with increasing energy has

to be implemented, which was not applied in the frame of this work.

After Mn deposition these facets disappear and a LEED pattern resembling to a (5×1) structure develops (Fig. 10.5). Annealing at 500 °C slightly deteriorates the quality of the LEED pattern, as the LEED spots decrease in intensity and are simultaneously enlarged. Consequently the deposition of Mn on the $ZnGeP_2$ surface changes the surface structure, implying also a change of the bulk structure at least in the region close to the surface.

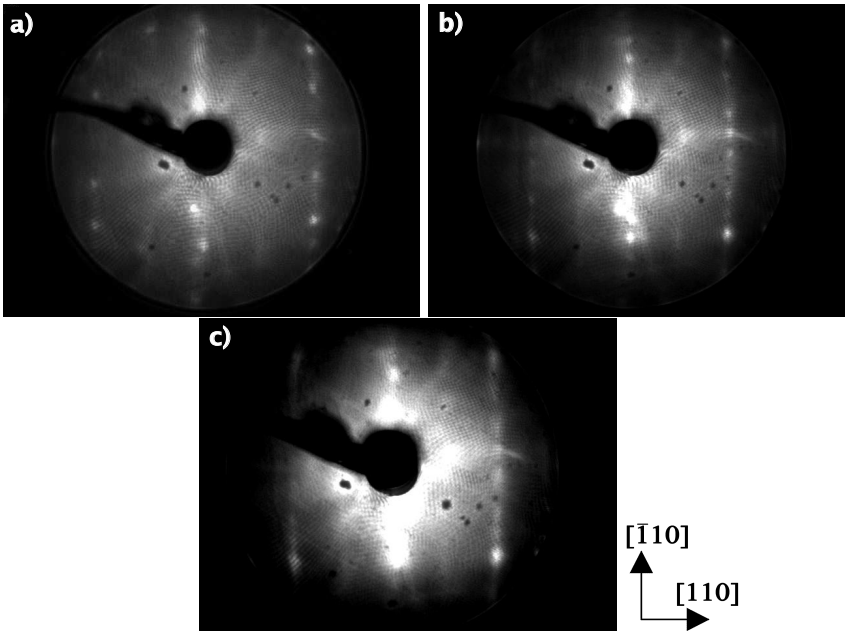

Figure 10.5: LEED patterns of the $ZnGeP_2$ (001) surface after Mn deposition at 400 °C for a) 39eV and b) 52eV and c) after annealing at 500 °C for 60eV. The surface structure resembles to a (5×1). After annealing the LEED spots of the (5×1) are slightly larger and more diffuse, implying some degradation of the surface structure.

Besides it is remarkable that the surface structure and facet formation of $ZnGeP_2$ differs by comparison to $CuInSe_2$ and $CuGaSe_2$. Namely the $CuInSe_2$ and $CuGaSe_2$ surfaces were found to form (4×2) structures and by particular stoichiometries (112) and $(\overline{112})$ facets. In contrast, the $ZnGeP_2$ (001) surface showed two different lattices turned by 45° towards each other which seem to be unreconstructed. The surface corresponding to the rotated lattice forms (102), $(\overline{1}02)$, (012) and $(01\overline{2})$ facets, thus the $ZnGeP_2$

facets are also turned by 45° in comparison to the $CuInSe_2$ facets. However, $ZnGeP_2$ belongs to the II-IV-V_2, while $CuInSe_2$ and $CuGaSe_2$ to the I-III-V_2 chalcopyrites. The properties of II-IV-V_2 pnictides are very similar to those of the I-III-V_2 chalcopyrites described in chapter 3. However, while in chalcopyrites the transition-atom 3d band occurs in the upper valence band, in pnictides the transition-atom 3d band occurs at lower energies near the IV-V band. As a result the Zn-P bonding in the valence band region does not have such a distinct covalent character as the Cu-Se bonding in the corresponding region [128]. Hence, with differences in the bonding of the atomic species of the different materials, also modifications on their atomic surface structure should be expected. Otherwise the growth conditions and the substrate of the particular $ZnGeP_2$ sample can be also related with the observed surface structure.

10.4 Summary

Summarizing, it was possible to deposit successfully Mn on $ZnGeP_2$ films and incorporate Mn atoms in Zn and P vacancies of the $ZnGeP_2$ bulk lattice. The clean $ZnGeP_2$ surface forms two different lattices turned by 45° towards each other with (1×1) structures. The surface corresponding to the rotated lattice forms (102), $(\overline{1}02)$, (012) and $(01\overline{2})$ facets. The $Mn/ZnGeP_2$ surface is modified in comparison to the clean $ZnGeP_2$ surface and shows a (5×1) structure. Furthermore electro-Paramagnetic Resonance (EPR) measurements performed by G.A. Medvedkin on the grown samples in fact showed the expected magnetic resonance effect [125], [126].

11 summary and outlook

In this work a preparation procedure for the $CuGaSe_2$, as well as the $CuInSe_2$ (001) surface was developed, enabling the observation of reconstructions for the first time. The structural properties of these surfaces were studied particularly with respect to composition.

The preparation by Ar^+ ion sputtering and annealing was optimized on the $CuGaSe_2$ (001) surface as a factor of Ar^+ ion energy, time and temperature. The $CuInSe_2$ surface was first prepared by decapping and then by the optimized Ar^+ ion sputtering and annealing procedure which enabled the observation of different structures. Similar results were obtained for both the $CuGaSe_2$ and $CuInSe_2$ (001) surfaces, depending on the preparation method as well as the bulk and surface composition. $CuGaSe_2$ layers grown with a moderate Cu-excess were completely covered with steps after a first sputtering cycle which had just removed the oxides layer. After a second sputtering cycle, the steps were also completely removed, giving rise to a clear (4×1) reconstruction. Likewise, $CuInSe_2$ layers with a Cu-poor bulk composition were completely faceted after decapping. After sputtering the facets were completely removed and a clear $(4 \times 2)/(2 \times 4)$ reconstruction was observed, which was transformed into a (4×2) by prolonged sputtering. During the transition of the surface from stepped/faceted to reconstructed, a slight Cu-enrichment in the surface composition was observed for both materials.

$CuGaSe_2$ layers grown with a high Cu-excess were flat after preparation, however, the (4×1) reconstruction was incomplete and the spots rather weak in intensity. $CuInSe_2$ layers with a stoichiometric bulk composition showed also an incomplete (4×2) reconstruction with weak spots. Sputtering of this surface improved its structure, so that a

sharp (4×2) reconstruction appeared, though steps were also present on this surface state. Remarkably, also the Cu/In surface ratio was reduced during this transition. Similiarly, $CuGaSe_2$ layers grown with a low Cu-excess exhibited a sharp (4×1) reconstruction with steps which did not recede by further sputtering.

Hence, a strong correlation between bulk, surface composition and surface structure is determined. A general, simplified scheme can be extracted showing a tendency of Cu-poor → stoichiometric → Cu-rich bulk or surface compositions corresponding to reconstructed with facet/steps → reconstructed and flat → weakly reconstructed but flat surfaces. The reconstructed and flat surfaces could be only obtained after sputtering of surfaces which were completely faceted/stepped after decapping/removal of oxide. During this transition also a Cu-enrichment of the surface composition was observed.

Moreover, according to the surface composition of the $CuInSe_2$ layers, the decapped faceted surface corresponds to the $CuIn_3Se_5$ phase, while the flat reconstructed surface to nearly stoichiometric $CuInSe_2$. On the oxidized $CuGaSe_2$ surface of the layer grown with a low Cu-excess, a surface component in the Ga3d level was also attributed to the $CuGa_3Se_5$ phase. Thus, the facets/steps are associated with the $CuIn_3Se_5$ or $CuGa_3Se_5$ phase.

With SXPS measurements BE shifts were found for the first time in all the Se3d, In4d, Ga3d, Cu3d core levels of both materials. By considering the structures found theoretically and experimentally on the similar ZnSe (100) surface, a model was proposed for the interpretation of the (4×2) reconstruction. The surface component with a BE shift of -0.5 eV in the Se3d emission of $CuInSe_2$ was attributed to Se dimers, while the surface components with a BE shift of +0.4 eV and +1.0 eV of the In4d and Cu3d emissions respectively were assigned to In and Cu adatoms. As similar surface components were observed in the $CuGaSe_2$ emissions, the same model is proposed for the interpretation of the $CuGaSe_2$ (4×1) reconstruction, as well. The $\times 1$ periodicity along the [110] could be explained by a Ga/Cu disorder in the adatom chains of $CuGaSe_2$.

Hence, in contrast to the prevailing expectation of the (112) to be the only stable chalcopyrite surface, the (001) surface is also stable under particular conditions. For

Cu-poorer compositions the tendency to form (112) facets is in fact observed. For particular optimal stoichiometries the facets can be completely removed leading to a clear reconstruction of the surface. For rather Cu-rich compositions no facets are formed. This information is important also for the understanding of grain boundaries properties of polycrystalline layers. Not only (112) oriented surfaces are present on the grain boundaries as it is believed, but also (001) surfaces should be possible in dependence of stoichiometry.

Further measurements of samples grown with different compositions are required in order to further clarify the interrelations of composition and surface structure. STM investigations, as well as total energy calculations would enable a more accurate interpretation of the observed reconstruction. The obtained information can contribute in the determination of defects and the understanding of recombination effects, important factors in the improvement of growth control as well as solar cell efficiency. The same preparation and investigation methods can be applied to the competitive $Cu(In, Ga)Se_2$ as well, so that analogous benefits are obtained.

A further experiment focusing on the deposition of ZnSe on the prepared $CuGaSe_2$ (001) surface was implemented, bearing significance for the ZnSe/$CuGaSe_2$ interface. Raman and luminescence measurements showed that the bulk properties of $CuGaSe_2$ are not affected either by sputtering nor by ZnSe deposition. However, some Zn seems to diffuse into the Zn-doped GaAs substrate. Instead of epitaxial growth, island formation is observed during ZnSe deposition. A (2×1) reconstruction with broad spots is obtained, characteristic for the Se-rich ZnSe surface.

For applications dealing with a magnetic resonance effect, the deposition of Mn on the prepared $ZnGeP_2$ (001) surface was studied. From the stoichiometry changes it appears that Mn atoms are incorporated in Zn and P vacancies of the $ZnGeP_2$ lattice as it was expected. On the clean $ZnGeP_2$ surface two different lattices are observed rotated by 45° towards each other with (1×1) structures. Also facets are observed which are estimated as (102), $(\overline{1}02)$, (012) and $(01\overline{2})$ oriented faces. The Mn/$ZnGeP_2$ surface shows a (5×1) structure.

Bibliography

[1] M. Green, J. Zhao, A. Wang and S. Wenham, Sol. Energy Mat. & Sol. Cells **65** (2001) 9

[2] K. Ramanathan, M.A. Contreras, C.L. Perkins, S. Asher, F.S. Hasoon, J. Keane, D. Young, M. Romero, W. Metzger, R. Noufi, J. Ward, and A. Duda, Prog. Photovolt. Res. Appl. **11** (2003) 225

[3] L. Stolt, J. Hedström, J. Kessler, M. Ruckh, K.O. Velthaus, and H.W. Schock, Appl. Phys. Lett. **62** (1993) 597

[4] M. Saad, H. Riazi, E. Bucher and M.C. Lux-Steiner, Appl. Phys. A **62** (1996) 181

[5] S. Siebentritt and U. Rau, Wide Gap Chalcopyrites (Springer, Berlin, New York, 2005)

[6] St. S. Hegedus and A. Luque, Handbook of Photovoltaic Science and Engineering, J. Wiley and Sons (2003)

[7] W.N. Shafarman and L. Stolt, Handbook of Photovoltaic Science and Engineering, edited by A. Kuque and S. Hegedus, J. Wiley and Sons (2003)

[8] U. Rau, H.W. Schock, Applied Physics A **69** (1999) 131

[9] S. Wagner, J. Shay, P. Migliorato, H. Kasper, Appl. Phys. Lett. **25** (1974) 434

[10] J. Shay, S. Wagner, H. Kasper, Appl. Phys. Lett. **27** (1975) 89

[11] V. Probst, W. Stetter, J. Palm, R. Toelle, S. Visbeck, H. Calwer, T. Niesen, H. Vogt, O. Hernández, M. Wendl, F.H. Karg, 3rd World Conference on Photovoltaic Solar Energy Conversion, Osaka **1** (2003) 329

[12] M. Powalla, B. Dimmler, 3rd World Conference on Photovoltaic Solar Energy Conversion, Osaka **1** (2003) 313

[13] Würth Solar (2005) http://www.wuerth-solar.de/we_web/frames.php?par LANG=EN&parKAT=335

[14] A. Ennaoui, M.C. Lux-Steiner, W. Eisele, Neue Materialien, HMI Ergebnisse 2000

[15] W. Fuhs, FVS-DGS Themen 2000, Photovoltaik - Stand und Perspektiven

[16] W.E. Devaney, W.S. Chen, J.M. Stewart, R.A. Mickelsen, IEEE Trans. Electron Devices **ED-37** (1990) 428

[17] K. Zweibel, B. von Roedern, H.S. Ullal, Photon International **10** (2004) 48

[18] J.H. Werner, J. Mattheis, U. Rau, Thin Solid Films (2004)

[19] I. Hengel, A. Neisser, R. Klenk, M.C. Lux-Steiner, Thin Solid FIlms **361/62** (2000) 458-462

[20] W. Calvet, Präparation und in-situ Charakterisierung MBE gewachsener Kupferindiumsulifd-Schichten, dissertation 2002

[21] R. Klenk, Thin Solid Films **387** (2001) 135

[22] S. Siebentritt, Thin Solid Films **403** (2002) 1

[23] J.E. Jaffe and Alex Zunger, Phys. Rev. B **29** (1984) 1882

[24] J.E. Jaffe and Alex Zunger, Phys. Rev. B **27** (1983) 5176

[25] J.E. Jaffe and Alex Zunger, Phys. Rev. B **28** (1983) 5822

[26] S.B. Zhang, Su-Huai Wei, Alex Zunger, and H. Katayama-Yoshida, Phys. Rev. B **57** (1998) 9642

[27] K.D. Becker, and S. Wagner, Phys. Rev. B **27** (1983) 5240

[28] J. Krustok, J.H. Schön, H. Collan, M. Yakushev, J. Mädasson, and E. Bucher, J. Appl. Phys. **86** (1999) 364

[29] J. Krustok, J. Raudoja, J.-H. Schön, M. Yakushev, H. Collan, Thin Solid Films **361** (2000) 406

[30] A. Bauknecht, S. Siebentritt, J. Albert, and M.C. Lux-Steiner, J. Appl. Phys. **89** (2001) 4391

[31] S. Schuler, S. Siebentritt, S. Nishiwaki, N. Rega, J. Beckmann, S. Brehme, and M.C.Lux-Steiner, Phys. Rev. B **69** (2004) 45210

[32] S. Siebentritt, I. Beckers, T. Riemann, J. Christen, A. Hoffmann, and M. Dworzak, Appl. Phys. Lett. **86** (2005) 91909

[33] W. Kleber, Einführung in die Kristallographie, VEB Verlag Technik Berlin (1977)

[34] Su-Huai Wei, L.G. Ferreira, and Alex Zunger, Phys. Rev. B **45** (1992) 2533

[35] Su-Huai Wei, S.B. Zhang, and Alex Zunger, Phys. Rev. B **59** (1999) R2478

[36] . D.S. Su, Su-Huai Wei, Appl. Phys. Lett., **74** (1999) 2483

[37] D.S. Su, W. Neumann, R. Hunger, P. Schubert-Bischoff, M. Giersig, H.J. Lewerenz, R. Scheer, and E. Zeitler, Appl. Phys. Lett. **73** (1998) 785

[38] B.J. Stanbery, S. Kincal, S. Kim, C.H. Chang, S.P. Ahrenkiel, G. Lippold, H. Neumann, T.J. Anderson and O.D. Crisalle, J. Appl. Phys. **91** (2002) 3598

[39] Su-Huai Wei, S.B. Zhang, and Alex Zunger, Phys. Rev. B **59** (1999) R2478

[40] D.S. Su, W. Neumann, M. Giersig, Thin Solid Films **361-362** (2000) 218

[41] H. Lüth, Surfaces and Interfaces of Solid Materials, Springer (1995)

[42] H. Ibach, and H. Lüth, Festkörperphysik, Springer, Berlin (1995)

[43] M. Henzler, W. Göpel, Oberflächenphysik des Festkörpers, Teubner (1994)

[44] M.D. Pashley, Phys. Rev. B **40** (1989) 10481

[45] M. D. Pashley, K.W. Haberern, W. Friday, J.M. Woodall, and P.D. Kirchner, Phys. Lett. **60** (1988) 2176

[46] M.D. Pashley, K.W. Haberern, and J.M. Woodall, J. Vac. Sci. Technol. B **6** (1988) 1468

[47] C.H. Park, and D.J. Chadi, Phys. Rev. B **49** (1994) 16467

[48] A. García and J. E. Northrup, J. Vac. Sci. Technol. B **12** (1994) 2678

[49] W. Weigand, A. Müller, L. Kilian, T. Schallenberg, P. Bach, G. Schmidt, L.W. Molenkamp, O. Bunk, R.L. Johnson, C. Kumpf, and E. Umbach, Phys. Rev. B **68** (2003) 241314

[50] W. Chen, A. Kahn, P. Soukiassian, P.S. Mangat, J. Gaines, C. Ponzoni, and D. Olego, Phys. Rev. B **49** (1994) 10790

[51] John E. Jaffe, Alex Zunger, Phys. Rev. B **64** (2001) 241304

[52] S.B. Zhang, and S.-H. Wei, Phys. Rev. B **65** (2002) 81402

[53] R. Hunger, C. Pettenkoffer, R. Scheer, Surface Science **477** (2001) 76

[54] J.J.M. Binsma, L.J. Giling, J. Bloem, J. Cryst. Growth **50** (1980) 429

[55] R. Scheer, Trends in Vac.Sci.Techn. **2** (1997) 77

[56] R. Scheer, and H.-J. Lewerenz, J. Vac. Sci. Technol. A **13** (1995) 1924

[57] D. Schmid, M. Ruckh, H.W. Schock, Appl. Surf. Sci. **103** (1996) 409

[58] J. Álvarez-García, A. Pérez-Rodríguez, A. Romano-Rodríguez, L.- Calvo-Barrio, R. Scheer and R. Klenk, J. Vac. Sci. Technol. A **19** (2001) 232

[59] M. Aggour, U. Störkel, C. Murrell, S.A. Campbell, H. Jungblut, P. Hoffmann, R. Mikalo, D. Schmeißer, H.J. Lewerenz, Thin Solid Films **403** (2002) 57

[60] V. Nadenau, D. Hariskos, H.-W. Schock, M. Krejci, F.-J. Haug, A.N. Tiwari, H. Zogg and G. Kostorz, J. Appl. Phys. **85** (1999) 534

[61] D. Liao and A. Rockett, Appl. Phys. Lett. **82** (2003) 2829

[62] R. Scheer, and H.-J. Lewerenz, J. Vac. Sci. Technol. A **12** (1994) 56

[63] M.V. Kuznetsov, E.V. Shalaeva, M.V. Yakushev, R.D. Tomlinson, Surf. Sci. **530** (2003) 237

[64] A.N. Tiwari, S. Blunier, M. Filzmoser, H. Zogg, D. Schmid, H.W. Schock, Appl. Phys. Lett. **65** (1994) 3347

[65] T.P. Massopust, P.J. Ireland, L.L. Kazmerski, and K.J. Bachmann, J. Vac. Sci.Techn.A **2** (1984) 1123

[66] M.P. Seah, W.A. Dench, Surface and Interface Analysis, **1** (1979) 2

[67] D. Briggs, and M.P. Seah, Practical Surface Analysis, J. Wiley & Sons (1983)

[68] P.W. Palmberg, G.E. Riach, R.E. Weber, N.C. MacDonald, Handbook of Auger Electron Spectroscopy (Physical Electronics Industries, Inc, U.S.A., 1972)

[69] G. Ertl, J. Küppers, Low Energy Electrons and Surface Chemistry, VCH (1985)

[70] M. Cardona and L. Ley, Photoemission in Solids I, Springer (1978)

[71] St. Hüfner, Photoelectron Spectroscopy, Springer (1995)

[72] J.J. Yeh and I. Lindau, Atomic Data and Nuclear Data Tables **32** (1985) 1-155

[73] S. B. C. G. Magaritondo, J.E. Rowe, Phys. Rev B **19** (1979) 2850

[74] J. A. Carlisle, M.T. Sieger, T. Miller, and T.C. Chiang, Phys. Rev. Lett **71** (1993) 2955

[75] M.T. Sieger, T. Miller, and T.C. Chiang, Phys. Rev. Lett **75** (1995) 2043

[76] N. Esser, A. Frisch, W. Richter, P. Vogt, W. Braun, R. Follath, and C. Jung, Solid State Commun. **113** (2000) 443

[77] M. Alonso, R. Cimino, and K. Horn, Phys. Rev. Lett. **64** (1990) 1947

[78] M. Alonso, R. Cimino, and K. Horn, J. Vac. Sci. Techn. A **9** (1991) 891

[79] M. H. Hecht, Phys. Rev. B, **41** (1990) 7918

[80] J. Humlicek, J. Quant. Spectrosc. Radiat. Tranfer **27** (1982) 437

[81] F. Schreier, J. Quant. Spectrosc. Radiat. Tranfer **48** (1992) 743

[82] B.H. Armstrong, J. Quant. Spectrosc. Radiat. Tranfer **7** (1967) 61

[83] E.E. Whiting, J. Quant. Spectrosc. Radiat. Tranfer **8** (1968) 1379

[84] T. Loeher, W. Jaegermann, C. Pettenkofer, J. Appl. Phys. **77** (1995) 731-738

[85] R. Hunger, Th. Schulmeyer, A. Klein, W. Jaegermann, K. Sakurai, A. Yamada, P. Fons, K. Matsubara, Sh. Niki, Surface Science **557** (2004) 263

[86] D. Liao and A. Rockett, J. Appl. Phys. **91** (2002) 1978

[87] U. Resch-Esser, N. Esser, D.T. Wang, M. Kuball, J. Zegenhagen, B.O. Fimland, W. Richter, Surf. Sci. **352-354** (1996) 71

[88] D. Drews, A. Schneider, D.R.T. Zahn, D. Wolffframm, D.A. Evans, Appl. Surf. Sci. **104** (1996) 485

[89] J.. Cerdá, F.J. Palomares, and F. Soria, Phys. Rev. Lett. **75** (1995) 665

[90] E.J. Heller, D.E. Savage, and M.G. Lagally, J. Vac. Sci. Technol. A **6** (1988) 1484

[91] J.R. Arthur, Surf. Sci. **43** (1974) 449

[92] K. Yamasaki, K. Asai, K. Shimada, and T. Makimura **129** (1982) 2760

[93] R. Behrisch, Topics in Applied Physics: Sputtering by Particle Bombardment I, Springer Verlag (1981)

[94] R. Behrisch, Topics in Applied Physics: Sputtering by Particle Bombardment II, Springer Verlag (1983)

[95] O. Auciello, R. Kelly, Ion Bombardment Modification of Surfaces, Elsevier (1984)

[96] M. Henzler, W. Göpel, Oberflächenphysik des Festkörpers, Teubner Stuttgart (1994)

[97] P. Corvini, A. Kahn, and S. Wagner, J. Appl. Phys. **57** (1985) 2967

[98] K. Otte, G. Lippold, D. Hirsch, A. Schindler, F. Bigl, Thin Solid Films **361-362** (2000) 498

[99] D. Haneman, R.D.L. Kristensen, and A. Hafiz, J. Appl. Phys. **2** (1986) 4030

[100] J. Álvarez-García, A. Pérez-Rodríguez, A. Romano-Rodríguez, J.R. Morante, L. Calvo-Barrio, R. Scheer and R. Klenk, J. Vac. Sci. Technol. A **19(1)** (2000) 232

[101] D.W. Niles, K. Ramanathan, F. Hasoon, and R. Noufi, J. Vac. Sci. Technol. A **15(6)** (1997) 3044

[102] Th. Glatzel, D. Fuertes Marrón, Th. Schedel-Niedrig, S. Sadewasser and M. Ch. Lux-Steiner, Appl. Phys. Lett. **81** (2002) 2017

[103] A. Bauknecht, S. Siebentritt, J. Albert, and M.Ch. Lux-Steiner, J. Appl. Phys. **89** (2001) 4391

[104] S. Horng and A. Kahn, J. Vac. Sci. Technol. B **7** (1989) 931

[105] F.J. Palomares, M.A. Méndes, M.T. Cuberes and F. Soria, J. Vac. Sci. Technol. A **9** (1991) 939

[106] M.J. Romero, K.M. Jones, J. AbuShama, Y. Yan, M.M. Al-Jassim, and R. Noufi, Appl. Phys. Lett. **83** (2003) 4731

[107] K. Gartsman, L. Chernyak, V. Lyahovitskaya, D. Cahen, Vl. Didik, V. Kozlovsky, R. Malkovich, El. Skoryatina, and V. Usacheva, J. Appl. Phys. **97** (1997) 4282

[108] U. Rau, D. Braunger, R. Herberholz, H.W. Schock, J-F. Guillemoles, L. Kronik and D. Cahen, J. Appl. Phys. **86** (1999) 497

[109] L.L. Kazmerski, O. Jamjoum, P.J. Ireland, S.K. Deb, R.A Mickelsen, and W. Chen, J. Vac. Sci. Technol. **19** (1981) 467

[110] R. Würz, M. Rusu, Th. Schedel-Niedrig, M.Ch. Lux-Steiner, H. Bluhm, M. Hävecker, E. Kleimenov, A. Knop-Gericke, R. Schlögl, Surface Science **580** (2005) 80

[111] R. Hunger, private communication

[112] K.A. Bertness, J.-J- Yeh, D.J. Friedman, P.H. Mahowald, A.K. Wahi, T. Kendelewicz, I. Lindau, and W.E. Spicer, Phys. Rev. B **38** (1988) 5406

[113] H. Iwakuro, C. Tatsuyama and S. Ichimura, Jap. J.Appl. Phys. **21** (1982) 94

[114] Th. Schulmeyer, private communication

[115] A.J. Nelson, G. Berry, A. Rockett, D.K. Shuh, J.A. Carlisle, D.G.J. Sutherland and L.J. Terminello, Appl. Phys. Lett. **70** (1997) 1873

[116] S. Niki, Y. Makita, A. Yamada, O. Hellman, P.J. Fons, A. Obara, Y. Okada, R. Shioda, H. Oyanagi, T. Kurafuji, S. Chichibu, H. Nakanishi, J. Cr. Growth **150** (1995) 1201

[117] W. Chen, A. Kahn, P. Soukiassian, P.S. Mangat, J. Gaines, C. Ponzoni and D. Olego, Phys. Rev. B **49** (1994) 10790

[118] A. Klein, Jaegermann, Pettenkofer, J. Appl. Phys. (1996)

[119] M. Gloeckler, J.R. Sites, and W.K. Metzger, J. Appl. Phys. (2005) in print

[120] A. Bauknecht, U.Blieske, T. Kampschulte, J. Albert, H. Sehnert, M. Ch. Lux-Steiner, A. Klein, and W. Jaegermann, Appl. Phys. Lett. **74** (1999) 1099

[121] C. Xue, D. Papadimitriou, Y.S. Raptis, N. Esser, W. Richter, S. Siebentritt, M.Ch. Lux-Steiner, J.Appl.Phys. **94** (2003) 4341

[122] F.W. Ohrendorf, H. Haeuseler, Cryst. Res. Technol. **34** (1999) 339

[123] F.W. Ohrendorf, H. Haeuseler, Cryst. Res. Technol. **35** (2000) 569

[124] S. Cho, S. Choi, G.-B.Cha, S.C. Hong, Y. Kim, and B.-C. Choi, Phys. Rev. Lett. **88** (2002) 257203

[125] P.G. Baranov, S.I. Goloshchapov, G.A. Medvekin, T. Ishibashi, K. Sato, J. Superconductivity: Incorporating Novel Magnetism **16** (2003) 131

[126] P.G. Baranov, S.I. Goloshchapov, G.A. Medvekin, V.G. Voevodin, JEPT Lett. **77** (2003) 582

[127] G.C. Xing, K.J. Bachmann, G.S. Solomon, J.B. Posthill, M.L. Timmons, J. Cryst. Growth **94** (1989) 381

[128] J.E. Jaffe and Alex Zunger, Phys. Rev. B **30** (1984) 741

Acknowledgments

I would like to thank the people who contributed to this thesis, especially

Dr. N. Esser for his support during the thesis and the fruitful discussions.

Prof. Dr. W. Richter and Prof. Dr. Lux-Steiner for giving me the opportunity to work at this thesis.

Prof. Dr. C. Thomsen for his careful reviewing of the thesis and his motivating attitude.

Prof. Dr. A. Knorr for being the chairman of my thesis committee.

The members of Prof. Richters group for the experimental support, especially Eugen Speiser for his commitment during UHV experiments and his forthcoming ideas for several technical problems, as well as Theo Herrmann. Also Bert Rähmer and Stefan Weeke for their willing and cooperative help at the AFM experiments. Engelbert Eder and Karim Friedemann for technical support and their encouraging smile. And furthermore Bert Rähmer, Regina Paßman, Sandya Chandola for the nice and amusing "Nachprüfung"!...

R. Hunger for the nice samples, providing beamtime, concentrated work during beamtime and a fruitful cooperation. Th. Schulmeyer for concentrated support during BESSY experiments and a lot of fun.

Dr. S. Siebentritt for the nice samples as well as contributing many ideas during evaluation. N. Rega for samples and willingness to provide important information about samples at any time.

Katy Rodenko for the nice chats during writing the thesis.

Maria Machon for the "expert" support during the preparation of the examination as well as amusing breaks with her and the other members of Prof. Thomsen's group during the whole thesis time.

very especially Uwe Kuhlmann for everything.